

**THE PHYSICS AND PERFORMANCE OF
IN GaAs QUANTUM DOT LASERS**

EMMA J PEARCE

PH.D. THESIS

Department of Physics and Astronomy

University of Cardiff

January 2005

UMI Number: U584784

All rights reserved

INFORMATION TO ALL USERS

The quality of this reproduction is dependent upon the quality of the copy submitted.

In the unlikely event that the author did not send a complete manuscript and there are missing pages, these will be noted. Also, if material had to be removed, a note will indicate the deletion.



UMI U584784

Published by ProQuest LLC 2013. Copyright in the Dissertation held by the Author.
Microform Edition © ProQuest LLC.

All rights reserved. This work is protected against
unauthorized copying under Title 17, United States Code.

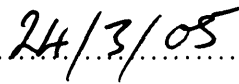


ProQuest LLC
789 East Eisenhower Parkway
P.O. Box 1346
Ann Arbor, MI 48106-1346

Declaration

This work has not previously been accepted in substance for any degree and is not being concurrently submitted in candidature for any degree.

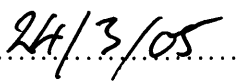
Signed..........(candidate)

Date..........

Statement 1

This thesis is the result of my own investigations, except where otherwise stated. Other sources are acknowledged by footnotes giving explicit references. A bibliography is appended.

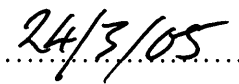
Signed..........(candidate)

Date..........

Statement 2

I hereby give consent for my thesis, if accepted, to be available for photocopying and for inter-library loan, and for the title and summary to be made available to outside organisations.

Signed..........(candidate)

Date..........

ABSTRACT

Quantum dot lasers are becoming increasingly technologically important. It is therefore essential to understand the factors affecting their current performance and be able to predict future performance.

The gain and unamplified spontaneous emission spectra have been measured for a selection of quantum dot devices and a quantum well device. The quotient of the gain and spontaneous emission spectra were used to calculate the P_F spectra and investigate the carrier distribution within the devices. Whilst the quantum well device and devices with one or three layers of dots exhibited characteristics consistent with Fermi-Dirac statistics, devices with more layers dots produced an unusual set of spectra, determined to be due to a non-thermal distribution of carriers in the ground state by looking at the unamplified spontaneous emission spectra.

A model was developed to investigate the effects of non-thermal carrier distributions on the calculated P_F spectra. From this it was deduced that it was possible to use a fit of a thermal P_F to the excited state P_F to calibrate the measured unamplified spontaneous emission spectra. The resultant P_F , gain and spontaneous emission spectra are sensitive to the exact balance between the homogeneous and inhomogeneous broadenings.

This calibration was used to calculate the radiative current densities and compare the radiative efficiencies of different structures, including both Dots-in-Well (DWELL) and standard dot structures. There was no large difference in efficiency found due to improved carrier injection in the DWELL structures. Calculated gain-radiative current density curves were used to predict the minimum transparency and threshold current densities that may be possible in the future. It is clear that the limits of quantum dot device performance have not yet been reached and that a factor of 1.7 improvement in threshold current density over state of the art devices could be achieved, even without reduced inhomogeneous broadening.

ACKNOWLEDGEMENTS

First of all I would like to thank my PhD supervisor Dr. Peter Smowton for his advice, time and belief in this project. I would like to thank the all members of the optoelectronics group, especially the technical help of Paul Hulyer who processed the structures. Thanks go to the Engineering and Physical Sciences Research Council (EPSRC) for their financial support over the last three years and to Bookham Technology who provided further financial support and a work placement through a CASE award.

I also want to thank my friends Iain and Madeline, Hannah, Dave and Iestyn who have been there with me throughout my PhD. As well as my Mum and Dad who haven't allowed me to give up, and my sisters Sarah, Jennifer and Nicola.

Finally, special thanks are due to my wonderful husband John who has been a great support over the last few years and given me the confidence to carry on and to my daughter Tiegan whose cheeky smiles and cuddles have kept me sane.

CONTENTS

ABSTRACT.....	2
ACKNOWLEDGEMENTS.....	3
CONTENTS	4
CHAPTER 1 INTRODUCTION.....	6
1.1 PROJECT AIMS	6
1.2 THE LASER	7
1.2.1 <i>What is a laser?</i>	7
1.2.2 <i>Achieving laser action</i>	7
1.3 SEMICONDUCTOR LASERS - BACKGROUND.....	10
1.3.1 <i>A Brief History of the Semiconductor laser</i>	10
1.3.2 <i>Structure of the Semiconductor Laser</i>	11
1.3.3 <i>Growth of Epitaxial Layers</i>	12
1.3.4 <i>Integration with other optical components</i>	12
1.4 LIGHT EMISSION IN SEMICONDUCTORS	13
1.4.1 <i>Optical Transitions</i>	13
1.4.2 <i>Non-radiative recombination</i>	19
1.5 CARRIER INJECTION AND CONFINEMENT OF LIGHT	22
1.5.1 <i>Homostructures</i>	22
1.5.2 <i>Heterostructures</i>	23
1.6 QUANTUM CONFINEMENT – WHY LOOK AT QUANTUM DOTS?	25
1.6.1 <i>The First Stage - Quantum Well Lasers</i>	25
1.6.2 <i>Quantum Dot Lasers</i>	28
1.7 REAL QUANTUM DOTS	28
1.7.1 <i>Practical Requirements</i>	28
1.7.2 <i>Stranski-Krastanow Growth Method</i>	30
1.8 LINE BROADENING PROCESSES IN QUANTUM DOT LASERS.....	30
1.8.1 <i>Homogeneous Broadening</i>	31
1.8.2 <i>Inhomogeneous Broadening</i>	31
1.9 GAIN AND SPONTANEOUS EMISSION IN QUANTUM WELLS AND QUANTUM DOTS.....	33
1.9.1 <i>Population Inversion Factor</i>	35
1.10 THESIS STRUCTURE	36
CHAPTER 2 DEVICE CHARACTERIZATION.....	38
2.1 DEVICE DETAILS	38
2.1.1 <i>Quantum Well Structure</i>	38
2.1.2 <i>Quantum Dot Structures</i>	39
2.1.3 <i>Electronic Coupling</i>	45
2.1.4 <i>Device Processing</i>	46
2.2 OPERATING WAVELENGTH AND SPECTRAL SHAPE.....	48
2.3 LIGHT-CURRENT CHARACTERISTICS	49
2.3.1 <i>Introduction</i>	49
2.3.2 <i>Experimental Method</i>	52
2.3.3 <i>Results</i>	53
2.4 THE MULTISECTION TECHNIQUE AND APPLICATIONS.....	55
2.4.1 <i>Theory</i>	55
2.4.2 <i>Experimental Details</i>	56
2.4.3 <i>Net Gain</i>	59
2.4.4 <i>Loss</i>	60
2.4.5 <i>Unamplified Spontaneous Emission and P_F factor</i>	61
2.5 CALCULATING THE OVERALL RADIATIVE EFFICIENCY.....	64

CHAPTER 3	NON-THERMAL CARRIER DISTRIBUTION	65
3.1	INTRODUCTION	65
3.2	P _F SPECTRA	65
3.3	SPONTANEOUS EMISSION AND GAIN SPECTRA	69
3.4	SEVEN-LAYER SAMPLE	72
3.5	SUMMARY OF OTHER STRUCTURES MEASURED.....	74
3.6	CONCLUSIONS	80
CHAPTER 4	MODELING PF	81
4.1	INTRODUCTION	81
4.2	THE MODEL.....	81
4.3	INPUTS.....	87
4.4	TRUE THERMAL DISTRIBUTION	90
4.5	QUASI THERMAL DISTRIBUTION.....	99
4.6	NON-THERMAL GROUND STATE DISTRIBUTION	109
4.7	CONCLUSIONS	113
CHAPTER 5	EFFICIENCY AND INTRINSIC PERFORMANCE	114
5.1	OVERALL RADIATIVE EFFICIENCY.....	114
5.1.1	<i>Introduction.....</i>	<i>114</i>
5.1.2	<i>Dots In Well versus Standard Quantum Dots.....</i>	<i>115</i>
5.1.3	<i>Ground State versus Excited State Efficiency</i>	<i>119</i>
5.1.4	<i>Variation with Current of the Efficiency.....</i>	<i>122</i>
5.1.5	<i>Spectral Explanation.....</i>	<i>123</i>
5.2	INTRINSIC PERFORMANCE.....	123
5.2.1	<i>Introduction.....</i>	<i>123</i>
5.2.2	<i>Gain - Current Curves</i>	<i>124</i>
5.2.3	<i>Gain versus Radiative Current.....</i>	<i>128</i>
5.3	EVALUATION OF ORIGIN OF NON-RADIATIVE RECOMBINATION.....	132
5.4	CONCLUSIONS	135
CHAPTER 6	SUMMARY AND FURTHER WORK.....	136
6.1	SUMMARY	136
6.2	FURTHER WORK	138
REFERENCES.....		139

1.1 PROJECT AIMS

Quantum dot lasers are becoming increasingly technologically important. It is therefore essential to understand the factors affecting their current performance and be able to predict future performance.

The main aim of this project has been to investigate the gain and unamplified spontaneous emission spectra for a selection of quantum dot devices and a quantum well device. The quotients of the gain and spontaneous emission spectra were used to calculate the P_F (population inversion factor) spectra and investigate the carrier energy distribution within the devices.

The aim was then to use the P_F spectra to calibrate the spontaneous emission and hence to calculate the radiative current densities and compare the radiative efficiencies of the different structures, including both Dots-in-Well (DWELL) and standard dot structures as it has been suggested that DWELL structures should show an improved injection efficiency due to improved carrier capture^[1].

Finally, I aim to predict the future performance of quantum dot lasers by using calculated gain-radiative current density curves to predict the minimum transparency and threshold current densities that may be possible in the future for devices with the same levels of inhomogeneous broadening.

1.2 THE LASER

1.2.1 WHAT IS A LASER?

The word LASER is an acronym standing for Light Amplification by Stimulated Emission of Radiation.

Five key laser characteristics are: spatial and temporal coherence, a clear threshold, strongly polarised light emission, and the existence of laser cavity modes.

1.2.2 ACHIEVING LASER ACTION

There are four things needed in order to achieve laser action.

- a gain medium for amplification that emits at the required wavelength,
- an energy source or pump to obtain population inversion,
- positive feedback in the form of mirrors to achieve coherent emission and
- a method of light extraction

The Gain Medium

The gain medium contains active centres that emit light. There is a variety of different types of laser, each with their own gain medium. Possible gain mediums include ruby or doped glass (solid state lasers), HeNe or CO₂ (gas lasers), GaAs or InP (semiconductor lasers). Organic lasers are also being developed.

In the lasers studied here, the active centres are InGaAs quantum dots, embedded within a GaAs quantum well. This gives an emission wavelength in the 1000nm range. An overview of light emission in semiconductors is given in Section 1.4. Further discussion of quantum dots is in Section 1.6 onwards.

Energy Sources

Energy sources can be optical, electrical or occasionally chemical. Optical sources are commonly used for solid state lasers. This is due to the difficulty in making electrical connections to the active medium. These sources can either be flashlights or other types of lasers.

Normally semiconductor lasers are electrically pumped using a p-n junction to inject the electrons and holes. This is contained within a more complex multilayer structure known as a heterostructure, which confines the light and carriers. One of the original drives for quantum dot devices was that it was thought that some of the advantages of atomic like systems could be accessed while still using an electrically pumped p-n junction for carrier injection.

Positive Feedback

Positive feedback is required to achieve coherent oscillations within the gain medium. In a laser, positive feedback is achieved by using two mirrors, one at each end of the cavity. These mirrors feedback a proportion of the light incident on them, increasing the photon density within the cavity and hence increasing stimulated emission - the key to laser action.

These mirrors can either be external to the gain medium or in the case of edge-emitting semiconductor lasers, formed from the refractive index difference at the interface between the gain medium and the air.

Spontaneous emission provides the initial stimulus to start the process. Spontaneously emitted photons of the appropriate energy, emitted in a direction along the cavity, are amplified by stimulated emission processes. These are then reflected by the mirrors and further amplified on the return path.

The laser threshold condition is reached when the roundtrip gain equals the roundtrip loss. The loss comes from several sources.

- Mirror transmission – this provides the useful output.
- Absorption and scattering at the mirrors.
- Absorption within the laser medium.
- Scattering losses at optical inhomogeneities in the medium

In semiconductor lasers, all apart from the first, transmission at the mirrors, are normally grouped under a distributed loss coefficient α_i . The required threshold gain can then be calculated using the Figure 1.1 for reference.

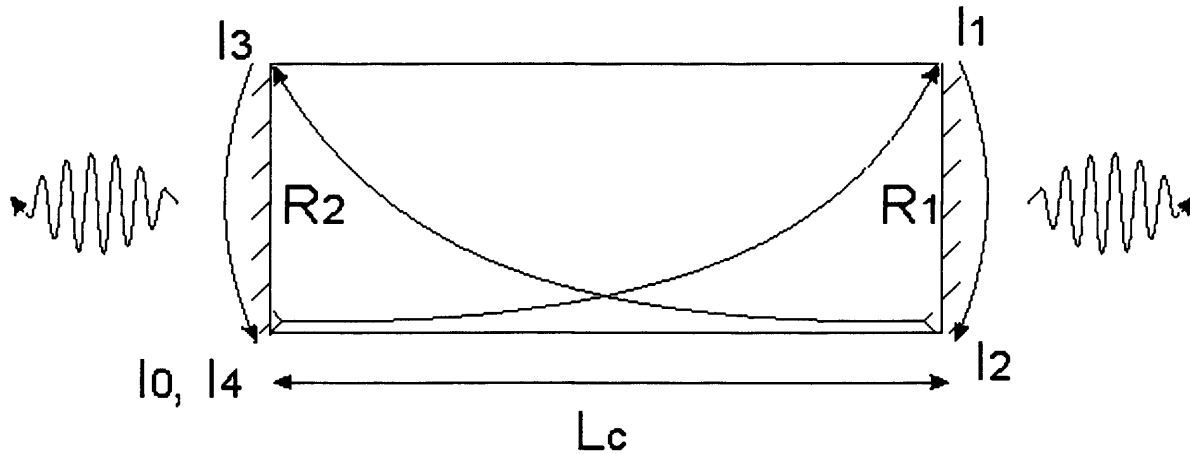


Figure 1.1 Schematic diagram of laser cavity indicating the exponential growth of light intensity along the cavity and the loss and reflection of light at each laser mirror

The initial light grows in intensity as it passes through the gain medium. If the length of the cavity is L_c , this gives a value for the intensity at the first mirror as shown in Equation 1.1.

$$I_1 = I_0 \exp[(G - \alpha_i)L_c]$$

Equation 1.1

Due to transmission losses at the first mirror, which has a reflectivity R_1 , the reflected intensity is reduced to a value

$$I_2 = R_1 I_1$$

Equation 1.2

This then grows exponentially again on the return trip...

$$I_3 = I_2 \exp[(G - \alpha_i)L_c]$$

Equation 1.3

... and has further losses due to transmission at the second mirror

$$I_4 = R_2 I_3$$

Equation 1.4

Substituting in the above equations gives a final value for I_4 in terms of the initial intensity I_0 , the reflectivities R_1 and R_2 , the gain G and the distributed losses α_i .

$$I_4 = R_1 R_2 I_0 \exp[2(G - \alpha_i)L_c]$$

Equation 1.5

For the round trip gain to equal the losses, the final intensity I_4 must equal the initial intensity I_0 . Setting $I_4=I_0$ and rearranging Equation 1.5 gives the threshold condition below.

$$\frac{I_4}{I_0} = R_1 R_2 \exp[2(G - \alpha_i)L_c] = 1$$

Equation 1.6

This can be rearranged in terms of the gain as shown in Equation 1.7.

$$G_{th} = \alpha_i + \frac{1}{2L_c} \ln\left(\frac{1}{R_1 R_2}\right)$$

Equation 1.7

This further simplifies to Equation 1.8 if the mirror reflectivities are equal.

$$G_{th} = \alpha_i + \frac{1}{L_c} \ln\left(\frac{1}{R}\right)$$

Equation 1.8

In a Fabry-Perot laser, this condition is normally first met at the peak of the gain spectrum.

1.3 SEMICONDUCTOR LASERS - BACKGROUND

1.3.1 A BRIEF HISTORY OF THE SEMICONDUCTOR LASER

The original concept of a semiconductor laser was first proposed in 1961 by Basov et al^[2] with the first working devices following in 1962^[3-6].

One of the first laser diodes was a simple gallium arsenide p-n junction created by Robert Hall, working for General Electric's Research and Development Laboratories in Schenectady, New York^[3]. The laser however required a current density of 10,000 Acm⁻² (compared for ≈ 100 Acm⁻² for the lasers studied here), and generated so much heat that it could only operate in a pulsed mode at 77K. The output wavelength of Hall's laser was 840nm.

The simple p-n junction was replaced by heterostructures in 1968^[7-9]. This meant that the lasers could now operate at room temperature.

In a heterostructure, the active layer is sandwiched between two or more layers of a slightly different material. In this configuration, both light and current can be confined to the active layer by using a material with a lower refractive index and band-gap energy larger than in the active layer. The operation of heterostructures is discussed further in Section 1.5.2.

A couple of years later in 1970, groups at both Bell Labs and the Soviet Union made the first semiconductor lasers that could operate continuously at room temperature^[10, 11]. However, they only lasted a few hours before failing.

Since then, one of the main applications leading development is that of optical fibre communications. Work has focused on lower threshold currents, higher efficiencies and powers, better reliability and new wavelength ranges. Semiconductor lasers are also now used commercially in a wide range of applications including data storage and medicine.

1.3.2 STRUCTURE OF THE SEMICONDUCTOR LASER

Semiconductor lasers can be either edge-emitting Fabry-Perot devices, or vertical cavity surface emitting lasers (VCSELs). As this work concentrates on edge-emitting lasers, the following discussion shall be limited to these.

A semiconductor laser consists of a substrate such as GaAs on top of which are grown epitaxial layers of other semiconductor materials such as $\text{Al}_x\text{Ga}_{1-x}\text{As}$. These layers are chosen with regard to their lattice constants, band-gaps and refractive indexes.

For the devices studied here, silicon oxide (SiO_2) is deposited onto the top of the structures and etched using photolithography to reveal a stripe. Gold contacts are then deposited on the top and on the bottom of the material. The wafer is then cleaved into individual lasers. The difference in refractive index between the semiconductor material and air at the facets provides the reflectivity needed for the feedback mirrors.

1.3.3 GROWTH OF EPITAXIAL LAYERS

An epitaxial growth process is one in which the arrangement of atoms in the deposited material is a continuation of the crystal structure of the substrate. There are three main epitaxial growth techniques, liquid phase epitaxy, metal organic chemical vapour deposition and molecular beam epitaxy.

In molecular beam epitaxy, or MBE, the new material is deposited on the substrate by means of beams of atoms directed at the surface. Each element to be deposited comes from its individual beam therefore control of the relative amounts of the elements is high. The high level of control that can be achieved is also used to grow layers from widths of only a few inter-atomic distances, with interfaces that are sharp on atomic length scales. All this occurs under vacuum to reduce contamination.

The temperature of the substrate must be held high enough for good epitaxial growth but low enough to prevent diffusion of atoms over significant distances. For complex multiple-layer structures with different melting points, MBE growth can become more of an art than a science.

In metal organic chemical vapour deposition, or MOCVD, material is deposited via the gaseous phase. This is the main technique that is used commercially to grow semiconductor lasers. Elements are carried to the surface as organic compounds, which then decompose on contact with the hot substrate.

Liquid phase epitaxy, or LPE, takes place in the liquid phase, as suggested by its name. As it is not as sophisticated as MBE, or MOCVD it is not normally used for semiconductor laser growth.

1.3.4 INTEGRATION WITH OTHER OPTICAL COMPONENTS

The need to cleave edge-emitting lasers is a disadvantage for integration with other semiconductor components. In this respect, VCSELs have a great advantage, the mirrors being formed epitaxially in the form of Bragg stacks. This enables the VCSEL to be operated in situ on the uncleaved substrate.

However, the relative simplicity of edge-emitting lasers is an advantage for research as there are fewer factors to take into account and they are simpler and therefore cheaper to fabricate. This is why many new material systems are first tested in edge-emitting lasers with the results subsequently being used to design VCSELs.

1.4 LIGHT EMISSION IN SEMICONDUCTORS

1.4.1 OPTICAL TRANSITIONS

The three main optical transitions that occur within a semiconductor laser are absorption, spontaneous emission and stimulated emission. Of these, only stimulated emission contributes to coherent optical gain.

For all the transitions, (crystal) momentum conservation is also required. Momentum is associated with the electron and hole \underline{k} values. This leads to the requirement of Equation 1.9

$$\underline{k}_h = \underline{k}_e + \underline{k}_{ph}$$

Equation 1.9

The photon k-vector can be calculated from the wavelength, λ using Equation 1.10, and for a typical laser wavelength of 1000nm this gives a value for the photon wave vector of $\sim 10^6 \text{m}^{-1}$.

$$k_{ph} = \frac{2\pi}{\lambda}$$

Equation 1.10

As typical k values for electrons and holes are of the order 10^8 to 10^9m^{-1} , this means that the photon momentum is negligible and therefore the electron momentum must equal the hole momentum. In the E-k diagram, this implies a vertical transition and therefore radiative recombination is higher in a direct gap semiconductor such as GaAs than in an indirect gap semiconductor such as Si where a phonon is additionally required to complete the transition, as shown in Figure 1.2.

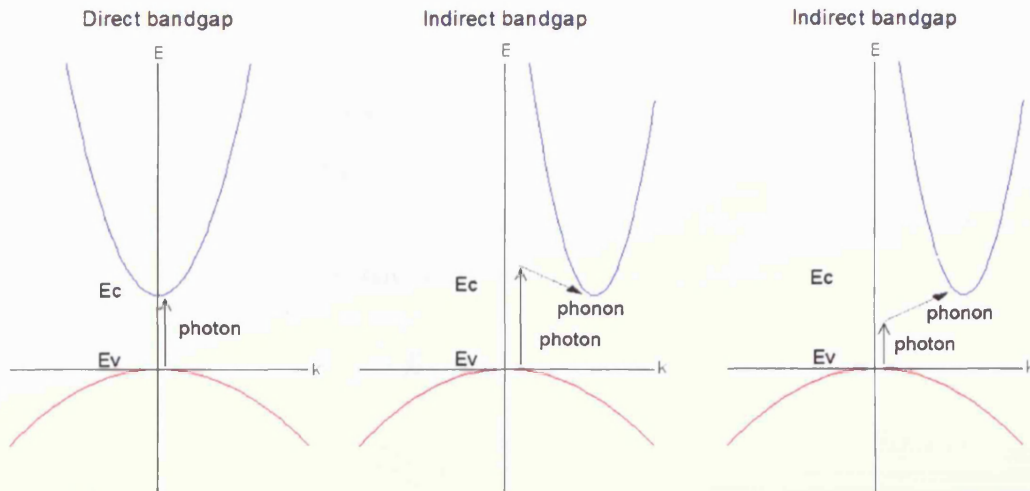


Figure 1.2 Diagram showing typical E-k curves for a direct band gap and an indirect band gap semiconductor. For an optical transition in an indirect band gap material, a phonon must be involved in addition to the photon reducing the probability of the transition

Absorption

In absorption, the electron starts in the valence band or lower energy state. On absorption of the energy from an incoming photon, the electron is promoted to a higher energy level within the conduction band.

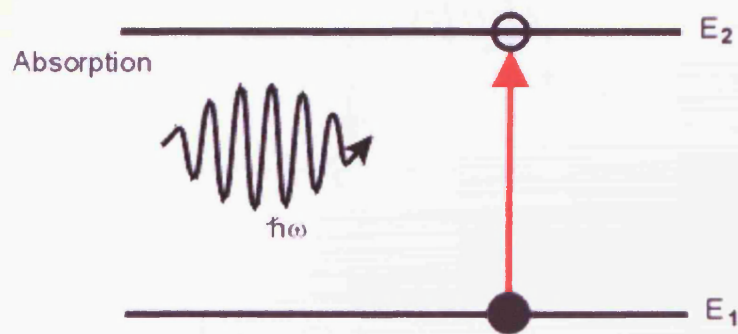


Figure 1.3 Absorption

The difference between the beginning and end energy levels of the electron is equal to the energy of the absorbed photon.

$$E_2 - E_1 = h\nu$$

Equation 1.11

The rate at which photons are absorbed is dependent on the number of occupied states in the valence band, the number of unoccupied states in the conduction band and the density of photons with the transition energy. In the equations below, p_1 and p_2 are the occupation probabilities of the lower and upper states respectively, B_{12} is the Einstein coefficient that represents the transition probability of an electron in the lower state being excited into a vacant upper state, and $\rho(\nu)$ is the photon density.

$$R_{abs} = B_{12}p_1(1 - p_2)\rho(\nu)$$

Equation 1.12

Spontaneous Emission

In spontaneous emission, an electron in the conduction band reverts to a lower energy state in the valence band releasing a photon in the process. Again, the energy of this photon is equal to the difference between the energy of the two electron states involved. The photon emitted has a random phase and direction and so doesn't contribute to the coherent optical gain.

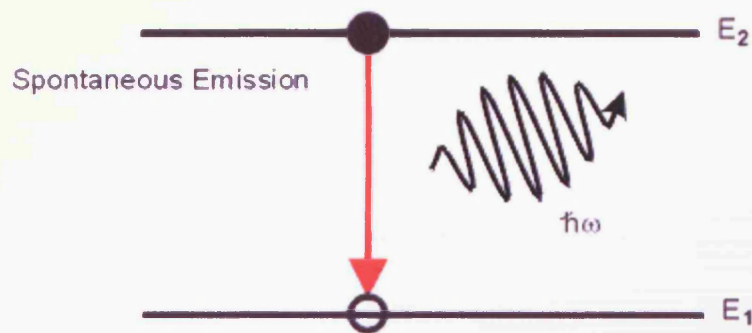


Figure 1.4 Spontaneous emission

The rate at which excited electrons will spontaneously emit photons is given by Equation 1.13 below, where A_{21} is the transition probability of an excited particle falling into a vacant lower state.

$$R_{spont} = A_{21}p_2(1 - p_1)$$

Equation 1.13

Stimulated Emission

During stimulated emission, a photon with the correct energy stimulates an already excited electron in the conduction band to revert to the valence band, releasing its energy as an additional photon. This additional photon has the same energy, phase and direction as the initial photon and contributes to the coherent optical gain of the laser.

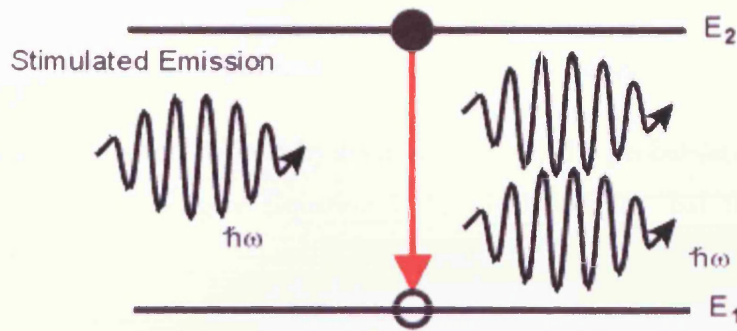


Figure 1.5 Stimulated emission

The stimulated emission rate depends on the occupation of both the levels and on the photon density at the transition energy as shown in Equation 1.14.

$$R_{stim} = B_{21}p_2(1 - p_1)\rho(\nu)$$

Equation 1.14

Einstein Relations

In equilibrium, the upward transitions must equal the downward transitions as shown in Equation 1.15.

$$R_{abs} = R_{spon} + R_{stim}$$

Equation 1.15

Substituting in for the equations above gives,

$$B_{12}p_1(1 - p_2)\rho(\nu) = A_{21}p_2(1 - p_1) + B_{21}p_2(1 - p_1)\rho(\nu)$$

Equation 1.16

This can then be solved for $\rho(\nu)$ to give,

$$\rho(\nu) = \frac{A_{21}p_2(1 - p_1)}{B_{12}p_1(1 - p_2) - B_{21}p_2(1 - p_1)}$$

Equation 1.17

Or,

$$\rho(\nu) = \frac{A_{21}}{B_{12} \frac{p_1(1-p_2)}{p_2(1-p_1)} - B_{21}}$$

Equation 1.18

As $\frac{p_1(1-p_2)}{p_2(1-p_1)}$ consists of the relative occupation probability of the states we can replace it with an expression derived by assuming that all the probabilities are governed by Fermi-Dirac statistics to give Equation 1.19, which implies that the system is in thermal equilibrium.

$$\rho(\nu) = \frac{A_{21}/B_{21}}{(B_{12}/B_{21})e^{(h\nu)/k_bT} - 1}$$

Equation 1.19

Comparing this with the Planck function for the distribution of radiation for a body in thermal equilibrium,

$$\rho(\nu) = \frac{\rho_0(\nu)h\nu}{e^{(h\nu)/k_bT} - 1}$$

Equation 1.20

Gives the results that for thermal equilibrium, the stimulated emission and stimulated absorption are complementary processes associated with the same recombination rate,

$$B_{12} = B_{21}$$

Equation 1.21

And

$$A_{21} = \rho_0(\nu)h\nu \cdot B_{21}$$

Equation 1.22

These results were derived by Einstein in 1917^[12], this is why the constants A and B are known as the Einstein coefficients.

Population Inversion

To increase the rate of stimulated emission for a pair of energy levels (in relation to spontaneous emission and absorption), we can see from Equation 1.16 above that it is necessary to increase both the photon density and the density of electrons in the upper level. For laser action to occur, one condition is that the population of the upper level must be higher than that of the lower level. This condition is called population inversion.

In order to achieve population inversion, energy must be provided to the electrons in the lower energy state to promote them to the higher energy state. This produces a non-thermal equilibrium situation – the energy distribution no longer obeys Fermi-Dirac statistics.

One method of pumping a laser is by stimulated absorption of light from another source. As $B_{12}=B_{21}$ as shown in Equation 1.21, once some electrons are excited into the upper level, the probabilities of further absorption or stimulated emission are equal. Therefore, the best situation that can be obtained in a two-level system is equality of the populations of the two levels.

For population inversion to be achieved, the minimum that is required is a three-level energy system as shown in Figure 1.6. Electrons are pumped from the ground state of the system to a higher, unstable state. From here, they rapidly decay to a more stable state between the two. Laser transitions occur between this metastable state and the ground state.

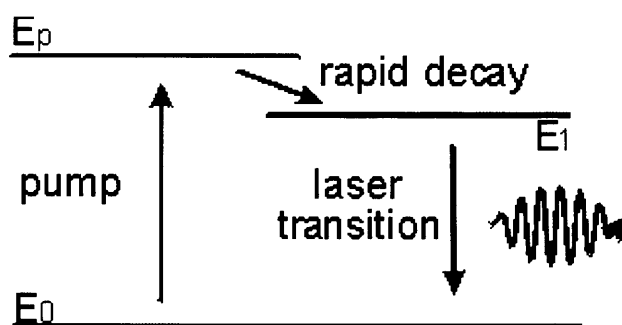


Figure 1.6 A three-level laser system

However, three-level energy systems require high pump powers. This is because the lower of the two laser transition states is the ground state and therefore over half the electrons in the system have to be pumped to the upper state to achieve inversion.

A much more efficient system is a four-level energy system as shown in Figure 1.7. In this case, the laser transition is between two intermediate states. Electrons are pumped to the highest energy level where they rapidly decay to a metastable state as before. The laser transition occurs between this state and a lower unstable state. The rapid decay from the lower laser-transition state to the ground state ensures a low population of the lower laser-transition state and therefore leads to a lower pumping requirement.

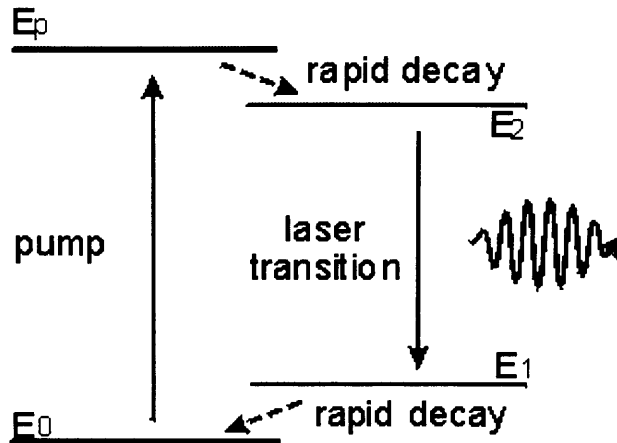


Figure 1.7 A four-level laser system

In a real semiconductor laser system, the uppermost energy level is normally many closely spaced energy levels, all with similar fast decay times. This increases the pumping efficiency. Carrier injection and population inversion within a semiconductor laser are discussed further in Section 1.5.

1.4.2 NON-RADIATIVE RECOMBINATION

Non-radiative recombination via defects - Shockley-Read-Hall

Electrons and holes can recombine via defect states within the energy gap^[13, 14]. Although in perfect semiconductors these should not be present, in any real system there are always impurities present. As these states are due to physical impurities, they are localised within space unlike the conduction and valence bands, which are extended in space throughout the semiconductor. As carriers move within the bands, they can be trapped by the defect. Once trapped they can then rapidly recombine with a carrier of the opposite type. As the defect states have an energy intermediate between that of the conduction and valence bands, they can facilitate the non-radiative recombination of an electron and hole.

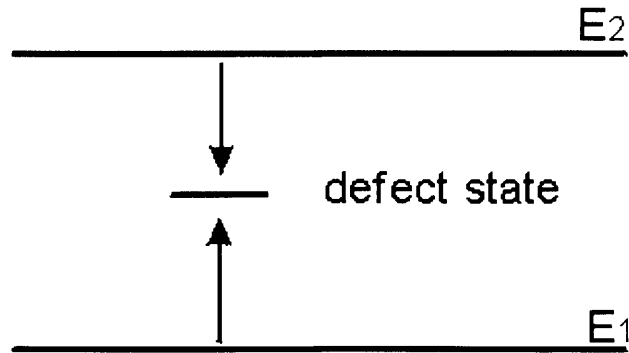


Figure 1.8 Non-radiative recombination via defects

Auger

Auger recombination is a non-radiative recombination process involving the interaction of at least three particles. The energy released by a recombining electron is immediately absorbed by another electron, which then dissipates the energy by emitting phonons. This is illustrated in Figure 1.9 below.

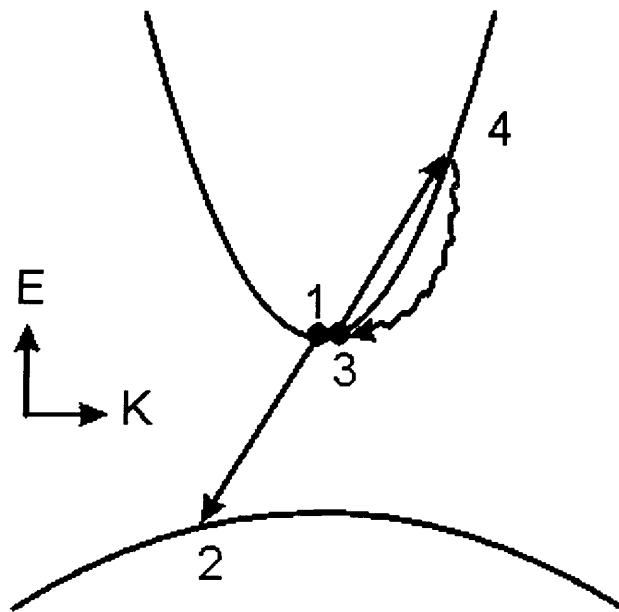


Figure 1.9 Auger recombination

An electron in the conduction band (1) recombines with a hole in the valence band (2). The energy released in this process promotes another electron in the conduction band (3) to a higher energy conduction band state (4). This ensures conservation of k momentum. The electron at (4) then relaxes back to its original energy by phonon emission.

The Auger recombination rate, for the process shown in Figure 1.9, is proportional to the electron density, n squared and the hole density, p as two electrons and one hole are involved in the process. This is shown in Equation 1.23. The coefficient C_A is larger for narrow band gap materials.

$$R_A = C_A n^2 p$$

Equation 1.23

1.5 CARRIER INJECTION AND CONFINEMENT OF LIGHT

The ease with which carriers can be injected and by which population inversion can be achieved is one of the most important characteristics of semiconductor lasers.

1.5.1 HOMOSTRUCTURES

In a simple p-n junction laser, population inversion is achieved by forward biasing a heavily doped p-n junction. In equilibrium, the Fermi level, E_f , lies within the conduction band for the n-type material and the valence band for the p-type material as shown in Figure 1.10.

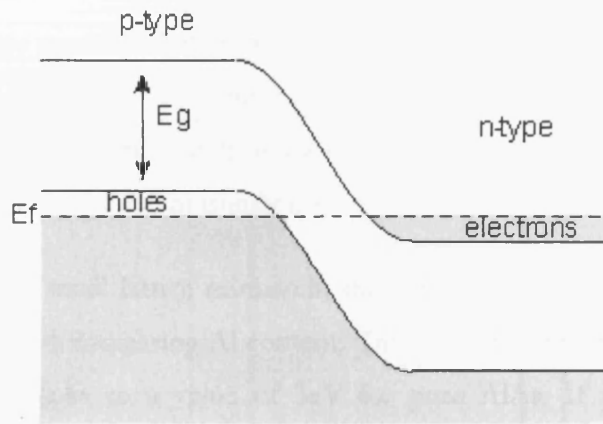


Figure 1.10 A p-n junction in equilibrium

When forward biased by a voltage approximately equal to the band gap, carriers are injected across the junction creating a population inversion as shown in Figure 1.11 and the Fermi level splits into two separate quasi-Fermi levels, E_{fc} and E_{fv} , reflecting the non-equilibrium electron and hole densities.

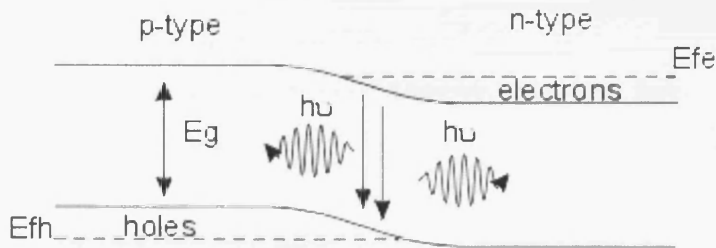


Figure 1.11 Population inversion in a simple p-n junction

Although there is some confinement of the light due to carrier induced refractive index change, this effect is very small as the index change is only about 0.02. This, combined with the low carrier confinement, is why threshold current densities are so high, allowing only pulsed operation at room temperature.

1.5.2 HETEROSTRUCTURES

A heterostructure exploits the differences in bandgaps and refractive indexes between mixed semiconductors of different compositions.

An example is the $\text{Al}_x\text{Ga}_{1-x}\text{As}$ ternary system, where the proportions of Al and Ga are varied. As Al and Ga have similar effective sizes in the crystal structure, this means that the variation in lattice constant between GaAs and AlAs is small at approximately 0.2% for room temperature. As the Al content generally only varies by a maximum of 30%, this ensures that the lattice mismatch at room temperature is only about 0.06%, small enough not to introduce significant numbers of crystalline defects^[15].

In addition to the small lattice mismatch, the AlGaAs system benefits from a large increase in bandgap with increasing Al content. This is approximately linear from a value of 1.43eV for pure GaAs to a value of 3eV for pure AlAs. If you take $3kT$ as the minimum bandgap step that gives useful carrier confinement, which at room temperature is 0.08eV, it can be seen that an AlGaAs system is highly suitable for this purpose^[15], even allowing for the fact that the band gap difference is split between the valence and conduction bands.

For optical confinement, and taking a three-layer dielectric slab as our model, the centre layer must have a refractive index higher than that of the cladding layers. As the refractive index decreases with increasing Al content in the above system, in addition to providing the carrier confinement as discussed above, the same layers also confine the light. This clearly reduces the losses due to absorption outside the high gain region.

Heterostructure lasers have developed in sophistication from the early single or double heterostructures discussed above. Many semiconductor lasers now use either single or multiple quantum wells surrounded by a separate confinement heterostructure (SCH), and cladding layers. This use of multiple layers allows greater flexibility in optimising the carrier and optical confinements for better device performance. Quantum wells themselves are simply heterostructures where the thickness of the layer is decreased such that quantum confinement effects become important.

An example of a separate confinement heterostructure is shown below in Figure 1.12.

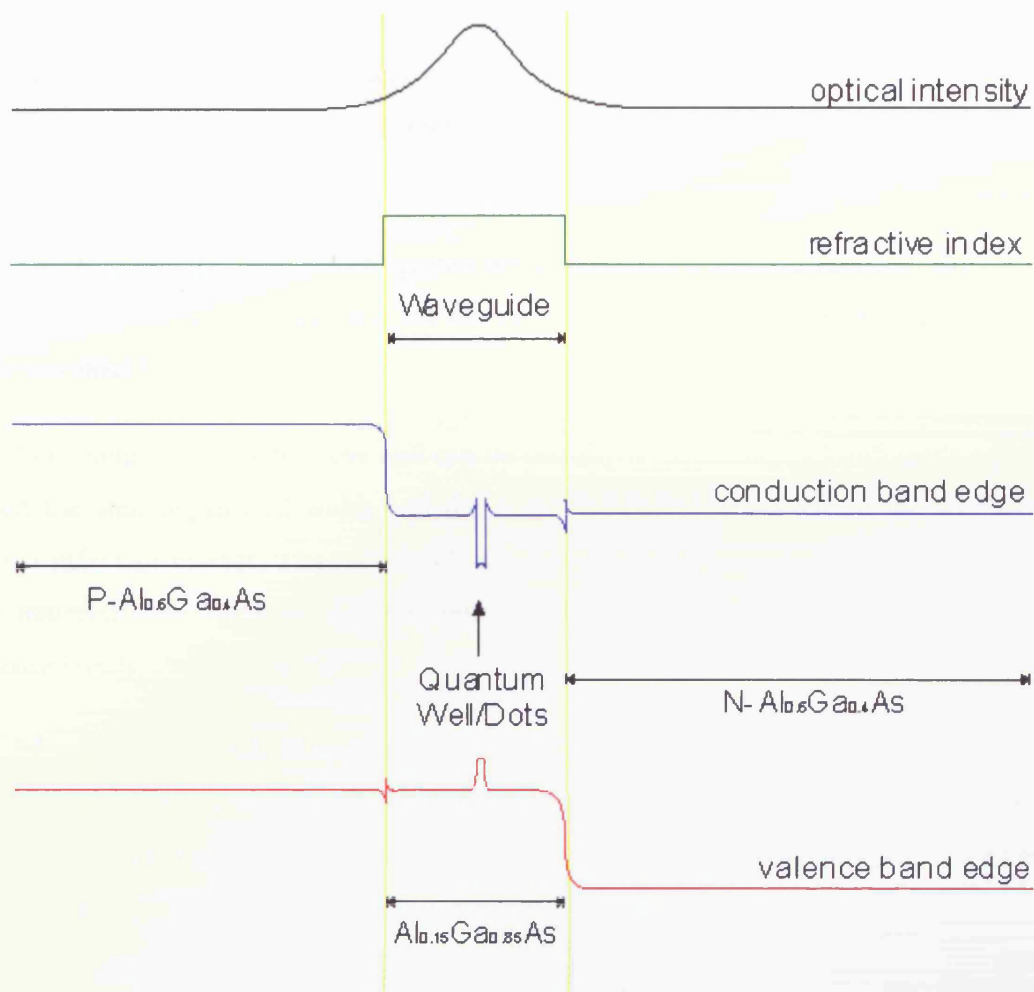


Figure 1.12 Schematic diagram of a separate confinement heterostructure showing both the variation in band edge energy through the device, which provides the electrical confinement, and the variation in refractive index, which produces the optical confinement

1.6 QUANTUM CONFINEMENT – WHY LOOK AT QUANTUM DOTS?

1.6.1 THE FIRST STAGE - QUANTUM WELL LASERS

When the active layer in a heterostructure decreases in thickness such that the width approaches that of the De-Broglie wavelength, quantum confinement effects start to become apparent. This distance is of the order of 10nm for semiconductors.

The resulting quantisation of the energy levels within the well increases the transition energy above that of the bulk material. As the energy levels depend on the thickness of the well, by adjusting this thickness the transition energy and hence the emitted wavelength of the laser can be altered. This allows tailoring of the wavelength of semiconductor lasers.

The gain and recombination spectra are narrowed by the quantisation leading to a lower current density requirement for the same maximum gain and hence the possibility of lower threshold currents.

The energy levels within the well can be calculated by solving Schrödinger's equation given the well depth and width and the components perpendicular to the well of the carrier effective masses. The well depth depends on the difference in band-gap between the materials and on how this difference is distributed between the conduction and valence bands, the band offset.

In a quantum well, the carrier momentum across the well is quantised with the associated electron and hole energies having discrete values. However, in the plane of the well the carriers are free to move. This leads to a step-like density of states function as illustrated in Figure 1.13.

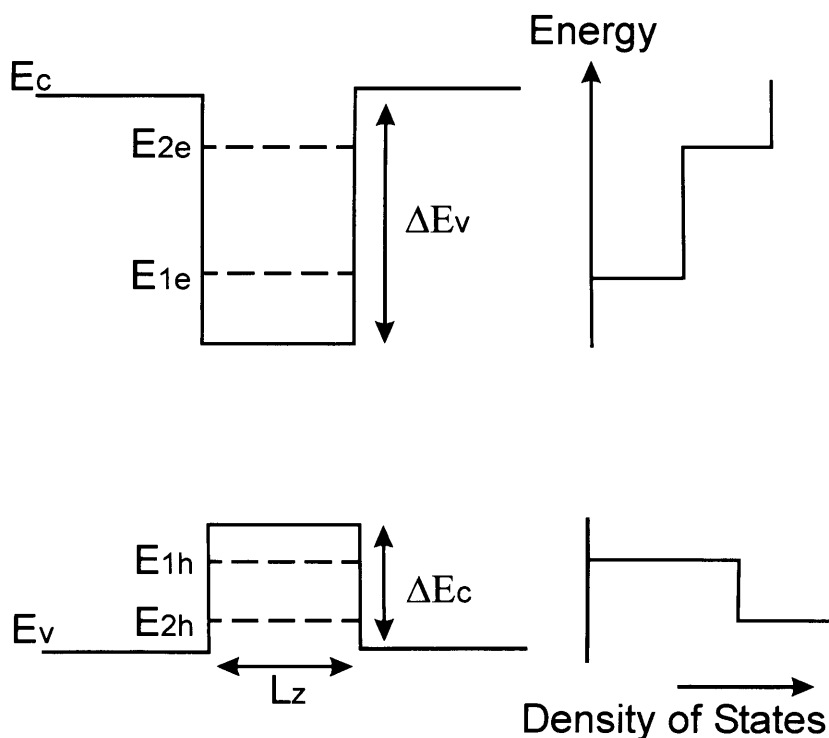


Figure 1.13 Two-dimensional density of states

Gain saturation occurs at high currents because as the quasi-Fermi levels enter the sub-bands, the rate of increase of gain with current decreases. The gain only increases significantly further when the next sub-band becomes sufficiently populated to begin laser action. This is accompanied by a shift in the gain peak to the transition energy of the next sub-band and a resulting decrease in the laser wavelength.

To summarise, the main qualitative differences between the 2D quantum well system and the 3D bulk system are as follows.

- The initial differential gain for quantum well lasers is greater than that of bulk lasers. This leads to lower threshold currents.
- The gain-current relationship of a quantum well is not linear as in the bulk case but tends to saturate at high currents within each sub-band. The accepted form of the gain-current relationship for quantum wells is given in Equation 1.24 where G is the gain and J the current density. G_0 and J_0 are fitting parameters^[16].

$$G = G_0 \ln\left(\frac{J}{J_0}\right) + 1$$

Equation 1.24

- The effective density of states increases proportionally with temperature leading to a weaker intrinsic temperature dependence of threshold current for a quantum well laser. However, this is not always met in real lasers due to thermally activated recombination currents associated with the barriers.
- The transparency current density, defined as where the gain equals zero, does not tend to zero for thin layers as in the bulk case, but is independent of Lz , even tending to increase for very thin wells.

1.6.2 QUANTUM DOT LASERS

After the successes of two-dimensional quantum wells in lasers, the next stage was to reduce the dimensionality further to one-dimensional quantum wires and to zero-dimensional quantum dots. As the carriers are now localised in all three dimensions in quantum dots, theoretically the energy levels are discrete as in atoms, with delta function density of states. Again, the measure of how small the dots must be for size quantisation effects to be apparent is that of the de Broglie wavelength. This gives a typical dot size of 10nm. Although it has atomic like energy levels and the resulting properties, it can still contain 10^4 or more atoms.

The three main advantages of quantum dots as the active region of semiconductor lasers that were originally proposed are:

- An improved temperature stability as the energy level separation is greater than the thermal energy^[17].
- Lower threshold currents, as with fewer possible states less charge carriers are needed for population inversion^[18].
- A narrow spectral linewidth as the discrete energy spectrum allows highly efficient laser action at a distinct energy.

Quantum dots also have an advantage over quantum wells in that material systems with greater lattice mismatches can be used, allowing access to a larger spectral range. For example, InGaAs quantum well lasers are limited to a wavelength of $\sim 1075\text{nm}$ as compositions needed to achieve longer wavelengths suffer from dislocations formed by inelastic relaxation of the lattice mismatch^[19].

1.7 REAL QUANTUM DOTS

1.7.1 PRACTICAL REQUIREMENTS

For quantum dots to be useful in practical devices such as semiconductor lasers, several requirements must be met.

- The three-dimensional potential well created by the quantum dots must be sufficiently large for at least one energy level to be present in the well. The separation between this energy level and the barrier must be large enough to limit the thermal escape of carriers at room temperature. This infers a minimum size for the dots that is dependent on the band offsets in the material system used.
- The quantum dots must be small enough that zero-dimensional confinement effects can be observed. For lasers, the thermal population of higher energy levels must be small, leading to a requirement that the separation of energy levels is as given in Equation 1.25^[20].

$$kT \leq \frac{1}{3} (E_2^{QD} - E_1^{QD})$$

Equation 1.25

- In an array, the dots must be of uniform size and shape. Fluctuations in these lead to a variation in the position of the energy levels and a resultant inhomogeneous broadening for quantum dot laser devices
- For a quantum dot laser to achieve sufficient gain to overcome the losses present there must be a high density of these uniform dots.
- Finally, the material should be free from defects such as dislocations, which would be detrimental to device performance. Dots grown by self-organised Stranski-Krastanow growth mechanisms should be most suitable for this purpose.

1.7.2 STRANSKI-KRASTANOW GROWTH METHOD

One method of growing quantum dots is the Stranski-Krastanow growth method^[21, 22] which depends on the dot material having a significantly larger lattice constant than the material it is grown on. This is the method used to grow the dots in this study. During epitaxial growth, the first few atomic layers form a planar wetting layer. As growth proceeds, the atoms tend to bunch up and form clusters as shown in Figure 1.14. This is energetically favoured as the compressive strain in the lattice can then relax thus reducing the energy of the islands. Energy considerations also cause the clusters to be of approximately uniform size.

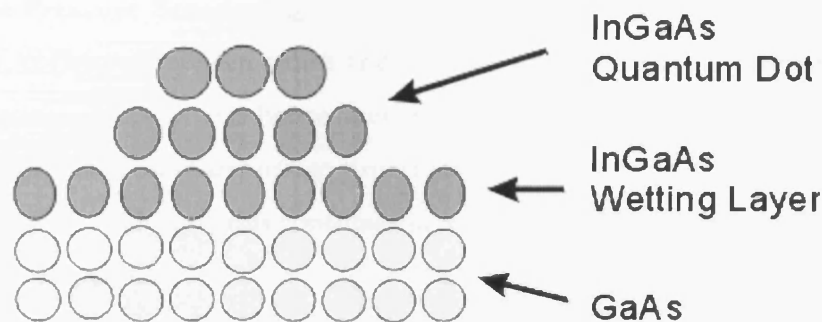


Figure 1.14 Stranski-Krastanow growth of quantum dots

A stabilising layer then covers the dots and further layers of dots can be grown on top. All these layers are then placed within a separate confinement heterostructure for improved optical and carrier confinement as described earlier in section 1.5.2 for a more conventional laser diode.

Other methods of producing semiconductor quantum dots can be used. Examples are lithography and etching of quantum well structures and the patterning of substrates and subsequent growth. These have the theoretical advantages of greater control over the shape, size and arrangement of dots but currently suffer from poor resolution and introduction of high numbers of defects and hence are not widely used.

1.8 LINE BROADENING PROCESSES IN QUANTUM DOT LASERS

There are two types of broadening present in every semiconductor laser. These are homogeneous broadening and inhomogeneous broadening and they have different physical causes and affect the spectral output of the laser in different ways. Without these broadening mechanisms, the spectral laser line would be a sharp delta function.

1.8.1 HOMOGENEOUS BROADENING

This mechanism broadens the line of each individual state and therefore the whole system in the same way. Each state has the same transition centre frequency. There are two potential causes

Natural or Intrinsic Broadening

The finite lifetime of excited states gives rise to a finite frequency spread due to the uncertainty principle. The lifetimes of both the upper and lower levels must be considered. This mechanism provides the theoretical lower limit to the linewidth.

Collision or Pressure Broadening

In a gas, collisions between atoms and between atoms and the walls of the container cause dephasing processes and hence alter the lifetime of the states. In a solid, such as a semiconductor laser, these dephasing processes are due to the interaction of the atoms with the lattice. In each case, this contribution to the overall broadening will increase with pressure and temperature.

The homogeneous broadening can be described by a Lorentzian lineshape – this is characteristic of damped resonant systems. This is shown in Equation 1.26, which describes the optical transition, where Λ is the full width half maximum of the frequency broadening.

$$L(h\nu - E, \Lambda) = \frac{\Lambda}{\pi \left[(h\nu - E)^2 + \left(\frac{\Lambda}{2} \right)^2 \right]}$$

Equation 1.26

1.8.2 INHOMOGENEOUS BROADENING

Inhomogeneous broadening is defined as broadening which affects each transition differently. Each state is distinguishable and has a different transition frequency. The spectrum is now a spread of individual transition frequencies.

In a quantum dot laser, inhomogeneous broadening is due to fluctuations in the physical properties of the dots such as their size, shape and composition. For dots grown by a self-assembled growth mechanism, such as the Stranski-Krastanow growth method employed for the devices studied in this thesis, this is thought to be the dominant broadening mechanism^[23].

Inhomogeneous broadening is characterised by a Gaussian distribution as shown in Equation 1.27, which again describes the optical transition where σ is the standard deviation characterising the broadening.

$$B(E, \sigma) = \frac{1}{\sigma\sqrt{2\pi}} \exp\left[-\frac{(E - E_{ensemble})^2}{2\sigma^2}\right]$$

Equation 1.27

The homogeneous and inhomogeneous broadenings are illustrated in Figure 1.15 for the case where the inhomogeneous broadening dominates.

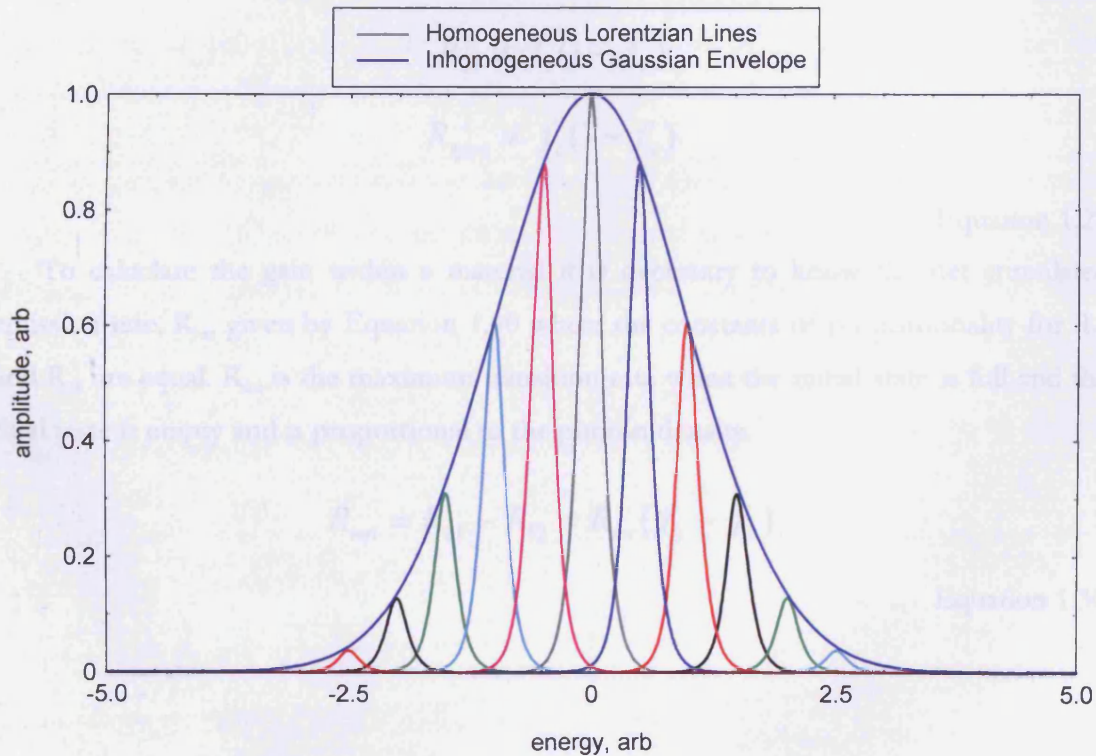


Figure 1.15 Homogeneous and inhomogeneous broadening illustrated for the situation where the homogeneous broadening of the individual dot transitions is significantly less than the inhomogeneous broadening due to the size and shape dispersion of the dots.

1.9 GAIN AND SPONTANEOUS EMISSION IN QUANTUM WELLS AND QUANTUM DOTS

If we go back to the equations describing the transmission rates for absorption, R_{12} , stimulated emission, R_{21} and spontaneous emission, R_{spont} , as discussed in Section 1.4.1, we will recall that the transition rate for absorption and stimulated emission are both proportional to the photon density. In addition, the transition rates are also proportional to the probabilities of the initial state being occupied and the final state being unoccupied. The probabilities that state 1 and state 2 are occupied are f_c and f_v respectively and can usually be described by the Fermi-Dirac distributions (Equation 1.28) using the quasi-Fermi levels for the electrons and holes, giving Equation 1.29.

$$f_i = \frac{1}{e^{(E_i - E_{F_i})/kT} + 1}$$

Equation 1.28

$$R_{12} \propto f_v(1 - f_c)$$

$$R_{21} \propto f_c(1 - f_v)$$

$$R_{\text{spont}} \propto f_c(1 - f_v)$$

Equation 1.29

To calculate the gain within a material it is necessary to know the net stimulated emission rate, R_{net} given by Equation 1.30 where the constants of proportionality for R_{12} and R_{21} are equal. R_{tot} is the maximum transition rate when the initial state is full and the final state is empty and is proportional to the photon density.

$$R_{\text{net}} = R_{21} - R_{12} = R_{\text{tot}}(f_c - f_v)$$

Equation 1.30

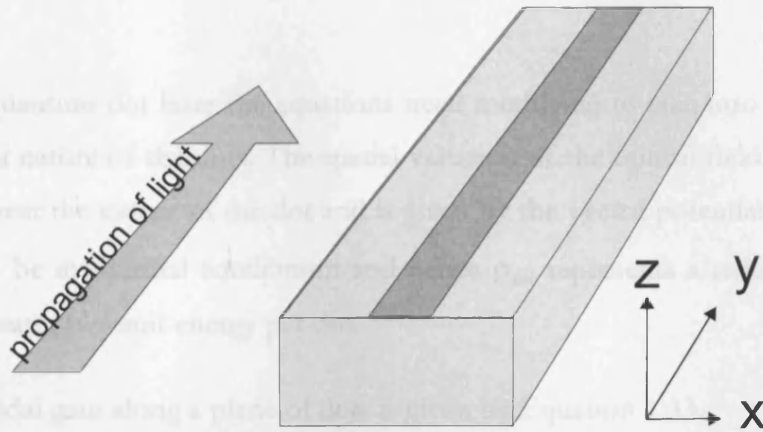


Figure 1.16 Schematic diagram showing the propagation direction for a conventional edge-emitting laser

For a conventional edge-emitting laser the optical field propagates in the plane of the quantum well (see Figure 1.16) and we can derive the equations for gain and spontaneous emission following the approach of Blood^[24]. The modal gain is defined as the fractional rate of increase of the total energy W_{tot} in the guided optical mode^[25] in the propagation direction (y). The optical mode is confined in the z direction by the slab waveguide and the intensity variation in this direction is $A(z)$ squared.

The gain for a quantum well can be given by Equation 1.31^[24], which has units of reciprocal length. M^2 is the momentum matrix element and the part in $\{ \}$ is the overlap integral of the normalised envelope functions, $F_{c,v}$ and the optical field. Together these describe the strength of the optical transition. The reduced density of state is given by ρ_{red}

$$G(h\nu) = \frac{4\pi\hbar}{nc\varepsilon_0(\hbar\omega)} \left(\frac{e}{2m_0} \right)^2 M^2 \frac{\left\{ \int F_v^*(z) A(z) F_c(z) dz \right\}^2}{\int A^2(z) dz} \rho_{red}(h\nu) (f_c - f_v)$$

Equation 1.31

Similarly, the spontaneous emission is given by Equation 1.32

$$R_{spont}(h\nu) = \frac{16\pi\hbar}{c^3 h^2 \varepsilon_0} (h\nu) \left(\frac{e}{2m_0} \right)^2 M^2 \left\{ \int F_v^*(z) F_c(z) dz \right\}^2 \rho_{red}(h\nu) \{ f_c (1 - f_v) \}$$

Equation 1.32

These equations both take into account the two-dimensional nature of the quantum well.

For a quantum dot laser the equations need modifying to take into account the zero dimensional nature of the dots. The spatial variation of the optical field is assumed to be negligible over the extent of the dot and is given by the vector potential A_0 . The dots are assumed to be in thermal equilibrium and hence ρ_{dot} represents a reduced ground state density of states per unit energy per dot.

The modal gain along a plane of dots is given by Equation 1.33.

$$G(h\nu) = \left[\frac{4\pi\hbar}{nc\varepsilon_0(\hbar\omega)} \left(\frac{e}{2m_0} \right)^2 M^2 \left\{ \int F_v^*(r) F_c(r) d^3r \right\}^2 \rho_{dot}(h\nu) (f_c - f_v) \right] \left[\frac{NA_0^2}{\int A^2(z) dz} \right]$$

Equation 1.33

This can also be written as in Equation 1.34 where σ represents a cross section with dimensions of area and w_{mod} is an effective mode width.

$$G = \sigma(f_c - f_v) N \frac{1}{w_{mod}}$$

Equation 1.34

1.9.1 POPULATION INVERSION FACTOR

If we take the quotient of the experimentally measured gain and unamplified spontaneous emission spectra then we can calculate a population inversion factor, P_F , spectrum. This describes the degree of population inversion in the device.

It can be seen that by dividing the equations for gain and spontaneous emission above (Equation 1.31 and Equation 1.32) we are left with something that is proportional to Equation 1.35, where f_1 and f_2 are the occupation probabilities of the electron and hole states respectively. The inversion factor equals one for energies where population inversion is achieved.

$$P_F = \frac{f_1 - f_2}{f_1(1 - f_2)}$$

Equation 1.35

If we have a thermal distribution then the P_F equals that derived from the Fermi - Dirac distribution as shown in Equation 1.36 and illustrated in Figure 1.17.

$$P_F = \frac{f_1 - f_2}{f_1(1 - f_2)} = 1 - \exp\left(\frac{h\nu - \Delta E_f}{kT}\right)$$

Equation 1.36

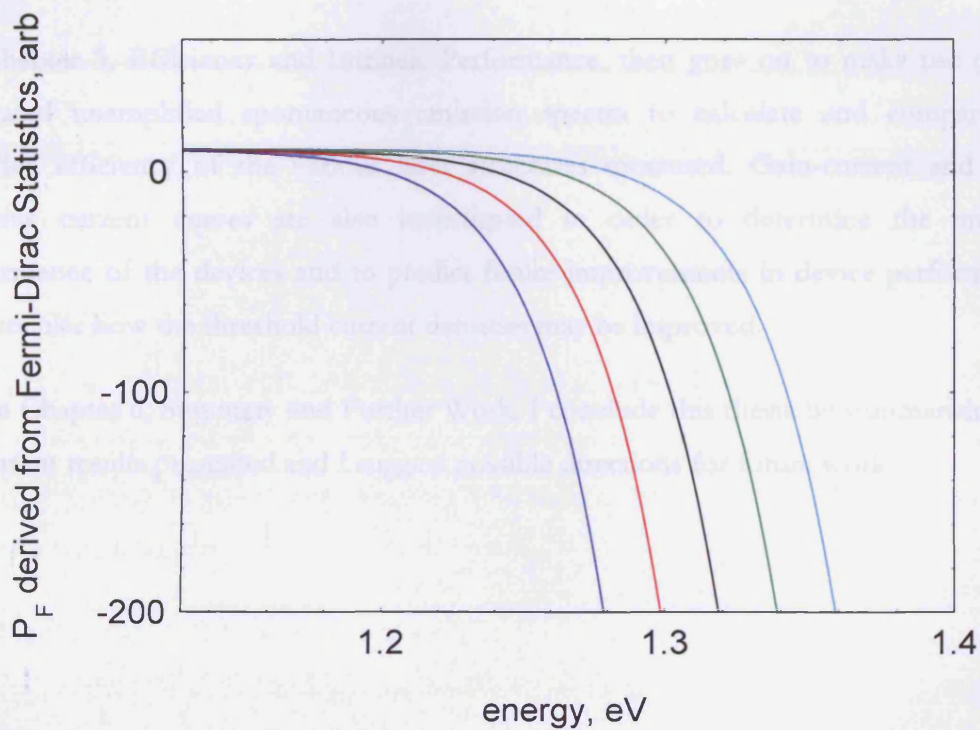


Figure 1.17 Calculated examples of the form of P_F spectra where the occupation of the states follows Fermi-Dirac Statistics. Lines from left to right are for increasing ΔE_f .

1.10 THESIS STRUCTURE

Following this chapter, the lasers structures measured within this project and the experimental techniques that have been used are described in Chapter 2, Device Characterization.

Chapter 3, Non-Thermal Carrier Distribution then goes on to present some of the experimental work that I have carried out on these devices and raises some interesting questions about how we can treat the data. In particular, I look at the inversion factor, P_i , spectra calculated from the quotient of the gain and unamplified spontaneous emission spectra.

The following chapter, Chapter 4, Modeling P_f uses a theoretical model I have developed to investigate how we could use a P_i spectrum that is not fully described by Fermi-Dirac statistics to calibrate the unamplified spontaneous emission spectra presented Chapter 3.

Chapter 5, Efficiency and Intrinsic Performance, then goes on to make use of the calibrated unamplified spontaneous emission spectra to calculate and compare the radiative efficiency of the various laser structures measured. Gain-current and gain-radiative current curves are also investigated in order to determine the intrinsic performance of the devices and to predict future improvements in device performance, in particular how the threshold current densities may be improved.

In Chapter 6, Summary and Further Work, I conclude this thesis by summarising the important results presented and I suggest possible directions for future work.

This chapter starts by describing the laser structures that have been studied before going on to introduce the initial experimental techniques employed for their characterisation. As well as being interesting experiments in themselves, the results from these measurements are used for rejecting faulty devices before progressing to the more time consuming measurements in the subsequent sections. These describe the multisection technique for measuring gain, loss and spontaneous emission.

2.1 DEVICE DETAILS

All the wafers described in this work were grown by Mark Hopkinson at the EPSRC National Centre for III-V Semiconductors in Sheffield, by Molecular Beam Epitaxy (MBE). Scanning Electron Microscopy (SEM) and photoluminescence measurements (PL) were also performed at the National Centre.

2.1.1 QUANTUM WELL STRUCTURE

Since the quantum well device is more conventional, I will describe it first. This structure was designed to emit in the same wavelength band ($1\mu\text{m}$) and to have a similar waveguide structure as the quantum dot structure; as such, it is not a fully optimised quantum well structure.

The quantum well devices studied consist of a 10nm wide quantum well consisting of $\text{In}_{0.22}\text{Ga}_{0.78}\text{As}$ set in a waveguide core of 80nm $\text{Al}_{0.15}\text{Ga}_{0.85}\text{As}$ and clad with 1200nm of $\text{Al}_{0.60}\text{Ga}_{0.40}\text{As}$ as shown in Figure 2.1. The quantum well and AlGaAs core are nominally undoped while the cladding layers are doped with Be and Si to form p and n-doped material at $\sim 2 \times 10^{18}$ and $5 \times 10^{18} \text{cm}^{-3}$ respectively. The material is grown on standard (100) orientated GaAs substrates. In addition, there is a p-doped top contact layer of GaAs doped $1 \times 10^{19} \text{cm}^{-3}$ to facilitate ohmic contact formation.

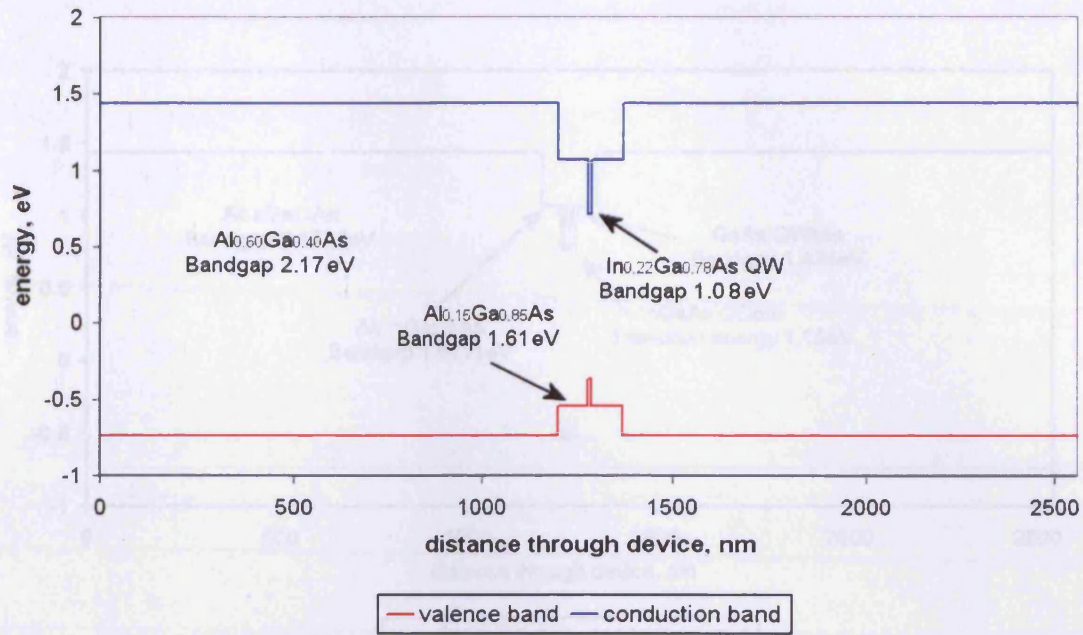


Figure 2.1 Schematic diagram of the band gap of the layers making up the quantum well laser. Note, the GaAs contact layers and the substrate are not shown.

2.1.2 QUANTUM DOT STRUCTURES

The main quantum dot structures studied consist of either three, five or seven layers of nominally $\text{In}_{0.5}\text{Ga}_{0.5}\text{As}$ quantum dots deposited within a 10 nm quantum well of GaAs. These GaAs layers are then separated by 7 nm of $\text{Al}_{0.15}\text{Ga}_{0.85}\text{As}$ and the rest of the waveguide core is made up $\text{Al}_{0.15}\text{Ga}_{0.85}\text{As}$. The width of this layer is adjusted to maintain a constant average effective mode width per quantum dot layer. The structures are then clad with 1200nm of doped $\text{Al}_{0.60}\text{Ga}_{0.40}\text{As}$ as shown in Figure 2.2. This is the type of structure commonly referred to in the literature as DWELL, or dots in well, structures. This can be seen in Figure 2.2. The rest of the structure was the same as in the quantum well structure.

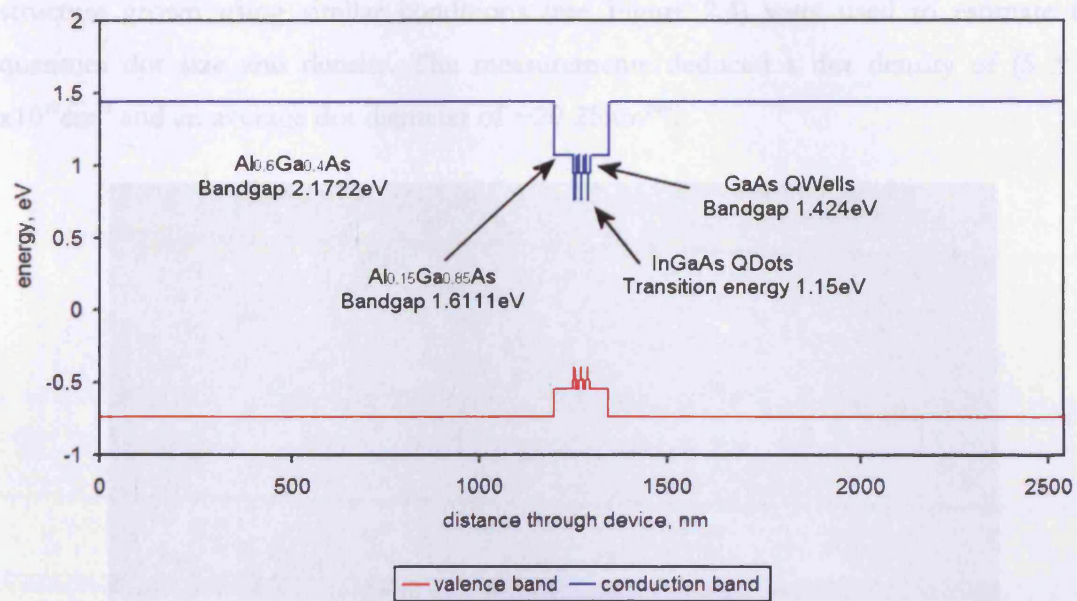


Figure 2.2 Schematic diagram of the band gap of the layers making up the quantum dot (DWELL) structures. Note, the GaAs contact layers and the substrate are not shown

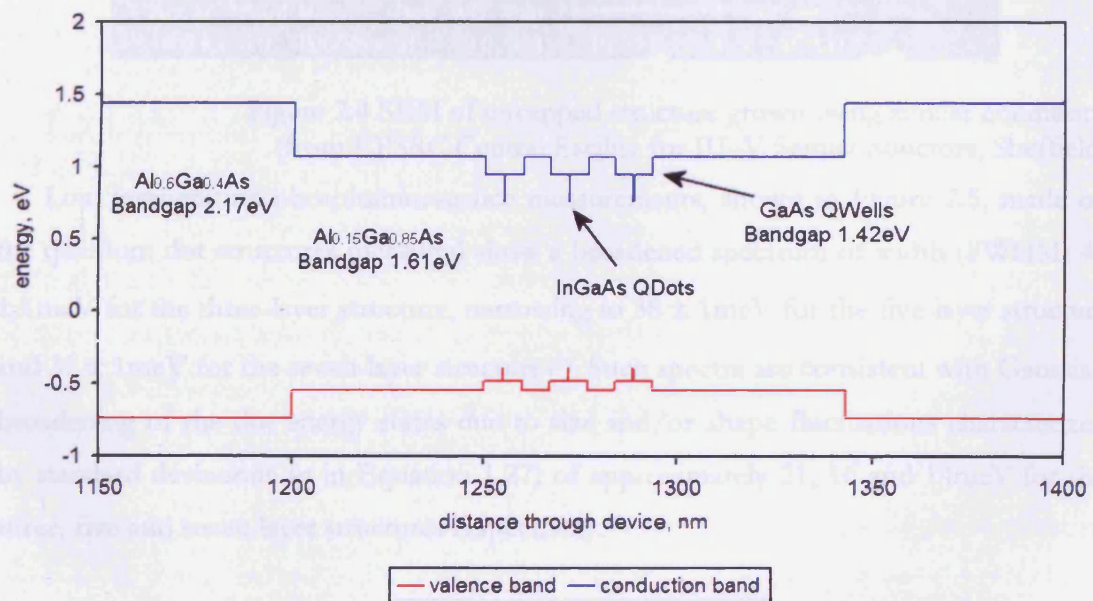


Figure 2.3 Enlargement of Figure 2.2, quantum dot (DWELL) structures

Field-emission scanning electron microscopy measurements on an uncapped structure grown using similar conditions (see Figure 2.4) were used to estimate the quantum dot size and density. The measurements deduced a dot density of $(5 \pm 1) \times 10^{10} \text{cm}^{-2}$ and an average dot diameter of $\sim 20\text{-}25 \text{nm}$ ^[26].

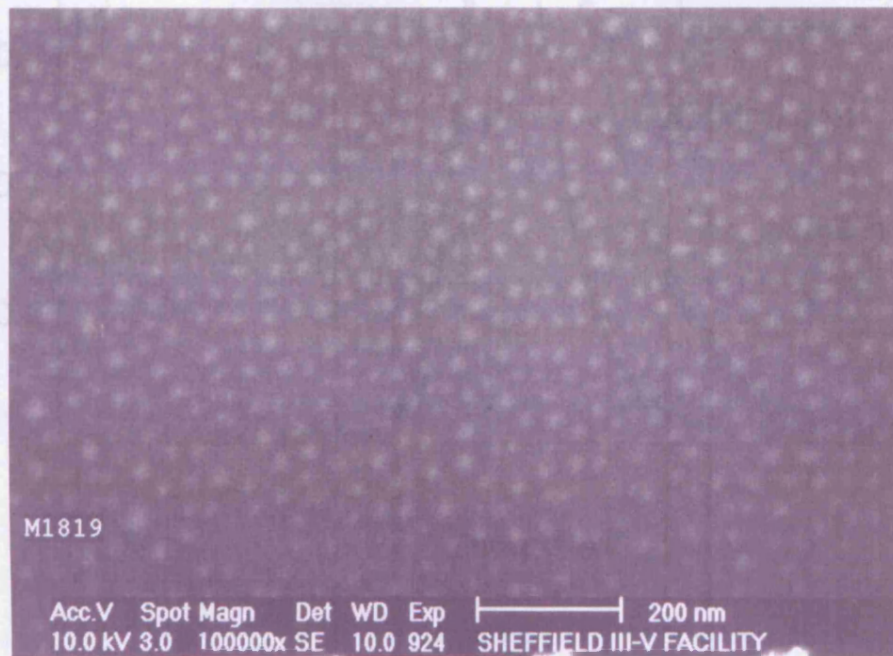


Figure 2.4 SEM of uncapped structure grown using similar conditions (from EPSRC Central Facility for III–V Semiconductors, Sheffield)

Low temperature photoluminescence measurements, shown in Figure 2.5, made on the quantum dot structures measured show a broadened spectrum of width (FWHM) $49 \pm 1 \text{meV}$ for the three-layer structure, narrowing to $38 \pm 1 \text{meV}$ for the five-layer structure and $32 \pm 1 \text{meV}$ for the seven-layer structure^[27]. Such spectra are consistent with Gaussian broadening of the dot energy states due to size and/or shape fluctuations characterized by standard deviations (σ in Equation 1.27) of approximately 21, 16 and 14meV for the three, five and seven layer structures respectively.

Other dot structures measured include similar structures but where the dot layers are deposited directly onto either $\text{In}_x\text{Ga}_{1-x}$ or bulk $\text{Al}_x\text{Ga}_{1-x}\text{As}$. Example diagrams of the band structure are shown in Figure 2.6 and Figure 2.7.

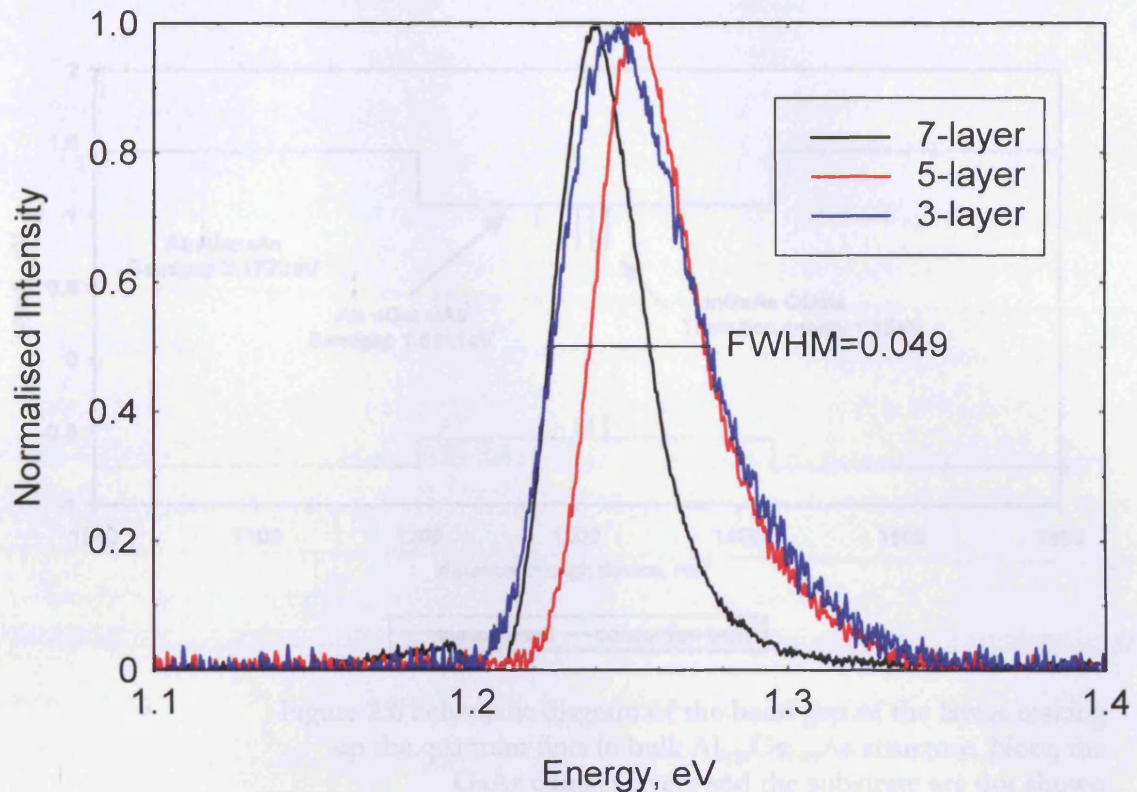


Figure 2.5 Low temperature PL measurements (Measured at Sheffield III-V Growth Facility)

It has been suggested in the literature that the narrowing of the low temperature PL spectra with increasing numbers of layers may be due to strain fields from initial layers seeding the growth of dots on subsequent layers and hence leading to a smaller distribution of dot sizes and shapes^[28]. Alternatively, it may be due to electronic coupling of dots in different layers^[29] however, due to the large separation between dot layers in our samples we believe the latter is unlikely (see section 2.1.3) and the linewidth narrowing is due to improved dot uniformity.

The peak position in Figure 2.5 shows no systematic change with the number of layers of dots and the seemingly random differences in peak energy may be due to small differences in the material growth conditions.

Other dot structures measured include similar structures but where the dot layers are deposited directly within either bulk GaAs or bulk $\text{Al}_{0.15}\text{Ga}_{0.85}\text{As}$. Example diagrams of the band structure are shown in Figure 2.6 and Figure 2.7.

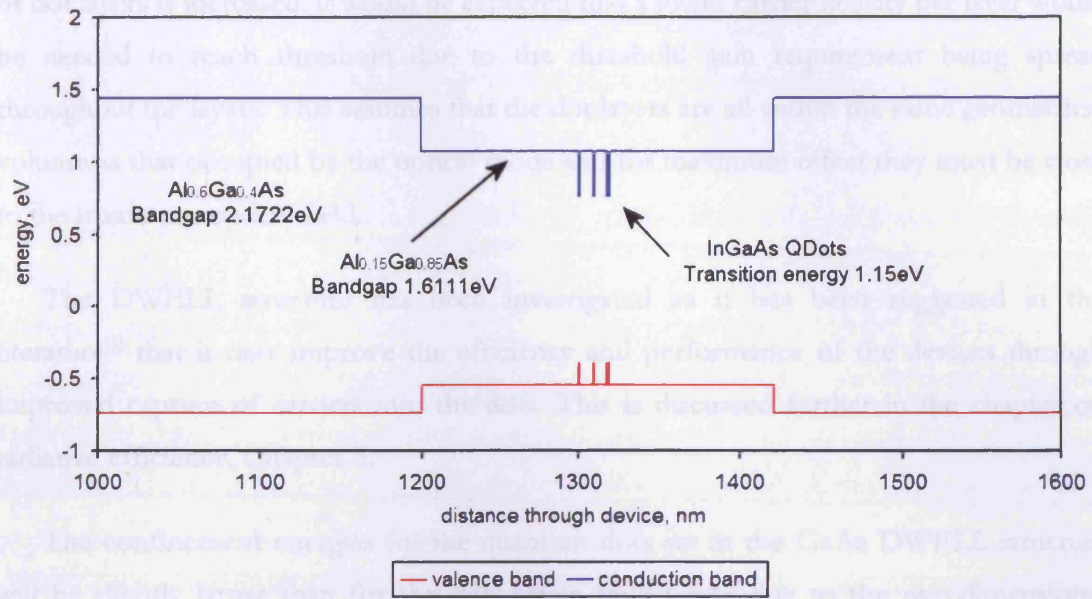


Figure 2.6 Schematic diagram of the band gap of the layers making up the quantum dots in bulk Al_{0.15}Ga_{0.85}As structure. Note, the GaAs contact layers and the substrate are not shown

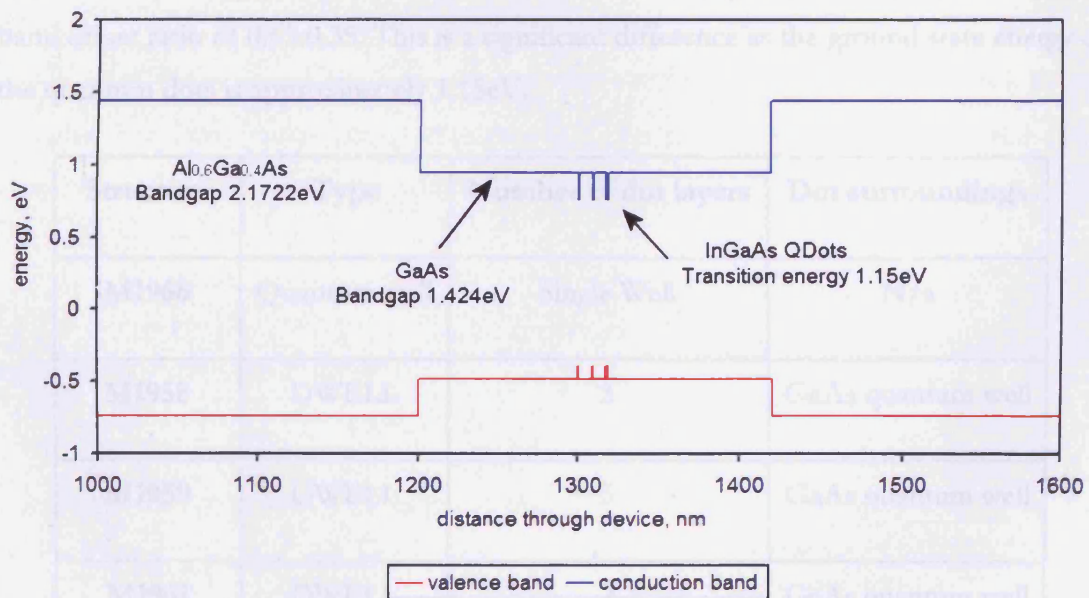


Figure 2.7 Schematic diagram of the band gap of the layers making up the quantum dots in bulk GaAs structure. Note, the GaAs contact layers and the substrate are not shown.

All the structures measured are summarised within Table 2.1 below. As the number of dot layers is increased, it would be expected that a lower carrier density per layer would be needed to reach threshold due to the threshold gain requirement being spread throughout the layers. This assumes that the dot layers are all within the same geometrical volume as that occupied by the optical mode and for maximum effect they must be close to the maximum optical field.

The DWELL structure has been investigated as it has been suggested in the literature^[1] that it may improve the efficiency and performance of the devices through improved capture of carriers into the dots. This is discussed further in the chapter on radiative efficiency, Chapter 5.

The confinement energies for the quantum dots set in the GaAs DWELL structure will be slightly larger than for the dots set in bulk GaAs due to the two-dimensional energy levels within the well. The electron confinement energy for the structure with the quantum dots set within $\text{Al}_{0.15}\text{Ga}_{0.85}\text{As}$ is 0.12eV greater due to the larger band gap of $\text{Al}_{0.15}\text{Ga}_{0.85}\text{As}$ as shown in the figures above. The corresponding difference in hole confinement energy is 0.06eV. Note this is obtained using a conduction band: valence band offset ratio of 0.65:0.35. This is a significant difference as the ground state energy of the quantum dots is approximately 1.15eV.

Structure	Type	Number of dot layers	Dot surroundings
M1966	Quantum well	Single Well	N/a
M1958	DWELL	3	GaAs quantum well
M1959	DWELL	5	GaAs quantum well
M1961	DWELL	7	GaAs quantum well
M1962	Quantum Dot	3	GaAs bulk
M1965	Quantum Dot	3	$\text{Al}_{0.15}\text{Ga}_{0.85}\text{As}$ bulk

Table 2.1 Summary of the structures measured

2.1.3 ELECTRONIC COUPLING

As the work in later chapters discusses the distribution of carriers amongst the various dot states, it is important to understand the degree to which the various states are electronically coupled.

The degree of electronic coupling between electrons in different layers and between holes in different layers has been investigated using a simple shooting method and literature values of material parameters^[30-32]. The transmission probability spectrum for an electron or hole to cross the structure has been calculated for our devices using this method by Angela Sobiesierski (née Kestle), Cardiff. I have then used these results to determine the tunnelling time, τ using Equation 2.1, where ΔE is the half-width at half-maximum of the Lorentzian transmission probability distribution.

$$\tau = \frac{\hbar}{\Delta E}$$

Equation 2.1

Calculated values are given in Table 2.2 for the broadest electron and light hole states. The dot layers are coupled if the tunnelling time is less than the recombination time, which is of the order of nanoseconds. An estimate of the recombination times in our samples has been made using Equation 2.2, where the density of dots has been determined from SEM measurements (Section 2.1.2), J is the current density and e the electronic charge. This gives a recombination time of less than 0.2ns.

$$\tau_{rec} \approx \frac{\text{densityofdots} \times \text{layers}}{J \times e}$$

Equation 2.2

Values are not given for the heavy holes, as it was impossible to resolve the peaks due to the energy resolution of the program, this would suggest that the half-width is small and hence the tunnelling time is large and the heavy holes must be uncoupled. The table shows that the electrons in the DWELL structures are definitely uncoupled and the light holes in the DWELLS are probably uncoupled, depending on the exact values of the recombination times but that the standard quantum dot structures are coupled.

Structure	ΔE , eV	τ , ns	Coupled?
3-layer DWELL electrons	1.44E-08	4.57E+01	No
3-layer DWELL light holes	6.78E-07	9.71E-01	No
5-layer DWELL electrons	9.27E-09	7.10E+01	No
5-layer DWELL light holes	4.60E-07	1.43E+00	No
7-layer DWELL electrons	6.95E-09	9.47E+01	No
7-layer DWELL light holes	3.41E-07	1.93E+00	No
3-layer dots in GaAs electrons	3.23E-05	2.04E-02	Yes
3-layer dots in GaAs light holes	1.65E-04	3.99E-03	Yes
3-layer dots in AlGaAs electrons	2.83E-06	2.32E-01	Yes
3-layer dots in AlGaAs light holes	3.44E-05	1.92E-02	Yes

Table 2.2 Calculated transmission times and coupling of layers

2.1.4 DEVICE PROCESSING

All the structures have been processed both into oxide isolated stripe contact Fabry-Perot laser devices as shown in Figure 2.8 and into multisection devices as described in the following sections. The process was performed by Mr Paul Hulyer in the Cardiff Cleanroom facility. The patterned oxide layer provides the lateral current confinement. A stripe width of 50 μm is used. After a bulk device, the oxide isolated stripe contact is the next simplest device architecture. It involves the least processing steps and therefore is most reproducible. It also has minimal effects on the material properties whilst still reducing the active area and hence the current required for operation.

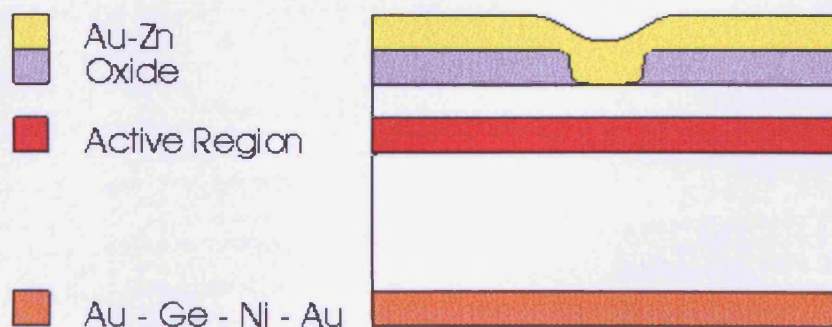


Figure 2.8 Schematic diagram of the cross-section of an oxide isolated stripe device

The wafers are cleaved into chips of width $300\mu\text{m}$ and lengths of between 300 and $1500\mu\text{m}$. The facets of the devices are left as cleaved as the reflectivity of the air-semiconductor boundary (0.3) is sufficient to allow laser action in the device lengths studied.

The device chips are then mounted on a copper heatsink, which is itself mounted on a TO-39 transistor header, using a conducting two part silver epoxy (Figure 2.9) and run in pulsed mode to reduce heating. The standard conditions are 1kHz and 300ns , which have been tested by varying the pulse length and repetition rate and looking for any temperature induced changes in the operating characteristics. For measurements designated as being taken at room temperature or 300K , there is no additional cooling.

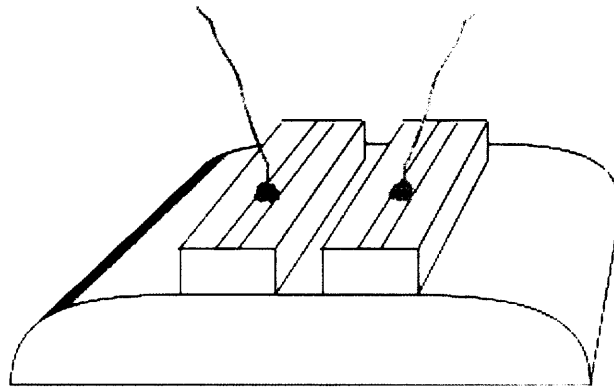


Figure 2.9 Schematic diagram of two separate laser devices mounted on copper heatsink

2.2 OPERATING WAVELENGTH AND SPECTRAL SHAPE

As all our devices emit light in the plane of the junction then the operating wavelengths of all our quantum dot and quantum well lasers are determined mainly by the material properties due to the large optical cavity length and hence the small cavity effects. Although Fabry-Perot modes are visible, due to the cavity, the position of the peak gain determines the laser wavelength. This is in contrast to a VCSEL where, due to the much smaller cavity size, cavity effects dominate the wavelength selection.

The laser operating wavelength and spectral shape can be determined using the experimental apparatus as shown in Figure 2.10. This includes a boxcar for measuring the applied currents (using a transformer to measure the voltage generated by the current pulse) and a monochromator, photo-multiplier tube and additional boxcar channel for measuring the voltage output from the photo-multiplier tube. For measurements where the light signal is large, then it is also necessary to use an intervening neutral density filter between the laser and monochromator to prevent saturation of and damage to the photo-multiplier tube. A linear polarizing filter is also normally used to separate the contributions from TE and TM polarised light (unless otherwise specified we are normally looking at the TE emission). It is important that this is used for any accurate measurements as the system spectral response is different for each polarization and hence the calibration of this assumes the polarizing filter is present. These measurements are normally repeated as a function of operating current.

The apparatus is set up for complete automated data acquisition using a computer for control and to save the data. Necessary inputs are the desired start, stop and step wavelengths and the desired current to be supplied to the device.

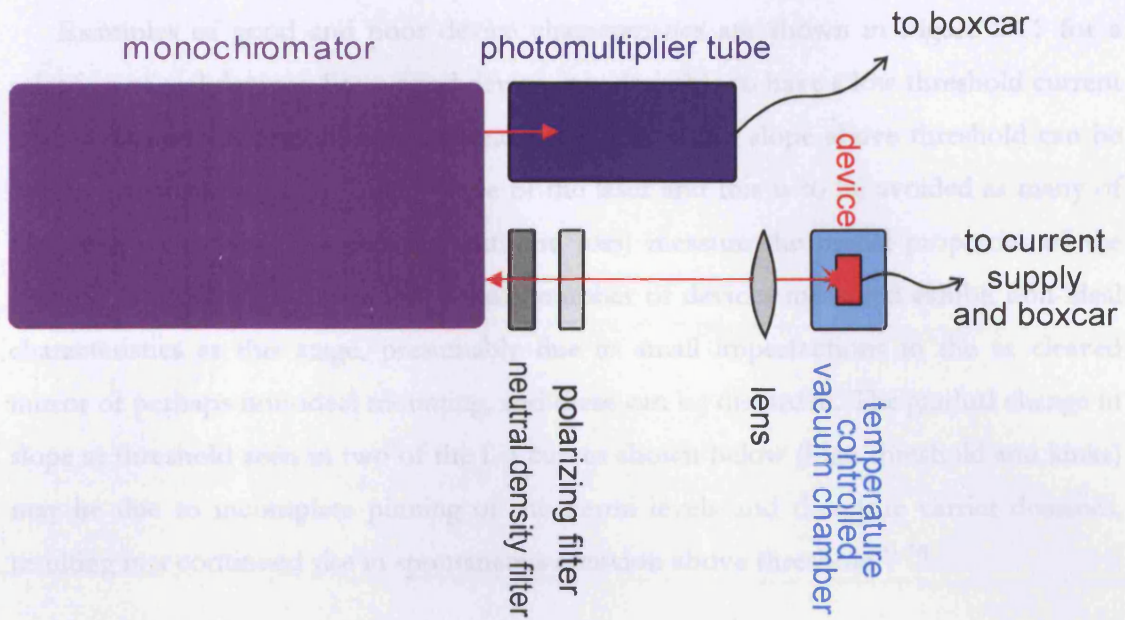


Figure 2.10 Schematic diagram of the experimental apparatus for spectral measurements

2.3 LIGHT-CURRENT CHARACTERISTICS

2.3.1 INTRODUCTION

A great deal of information can be obtained simply from measuring the light-current (L-I) characteristics of a laser. Once the electrical characteristics have been checked on a curve tracer this is often the first measurement taken on every device. In this case, the optical power is determined using a standard p-i-n photodiode operated in photoconductive mode and a boxcar to measure the voltage generated by the photoconductive current through a known resistor. The current through the laser is again measured using a pulse transformer.

Examples of good and poor device characteristics are shown in Figure 2.11 for a selection of real devices. For a good device, it is desirable to have a low threshold current and a constant steep slope above threshold. Kinks in the slope above threshold can be due to a change in the operating mode of the laser and this is to be avoided as many of the subsequent measurements (eg gain and loss) measure the modal properties of the devices. It is usually the case that a small number of devices measured exhibit non-ideal characteristics at this stage, presumably due to small imperfections in the as cleaved mirror or perhaps non-ideal mounting, and these can be discarded. The gradual change in slope at threshold seen in two of the L-I curves shown below (high threshold and kinks) may be due to incomplete pinning of the Fermi levels and therefore carrier densities, resulting in a continued rise in spontaneous emission above threshold^[33, 34].

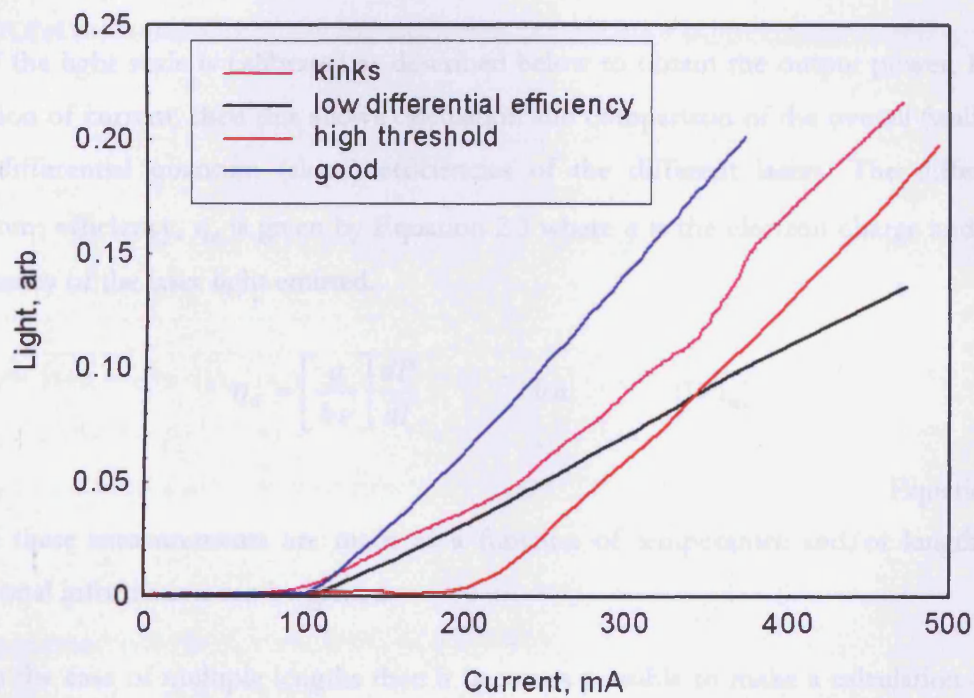


Figure 2.11 Examples of some of the L-I characteristics measured. Non-ideal characteristics are indicated.

When we are looking at the potential for high power operation of lasers the threshold current is not as important as the slope efficiency, as in use the devices would be driven at many times threshold. Also important in this case is that there is no thermal rollover in light output due to heating within the device. This is seen more often when devices are operated in continuous current (CW) mode as opposed to pulsed current mode. It is also more prevalent in VCSEL devices as the geometry is much smaller. As heating is more a property of the device geometry and heat sinking arrangements rather than a material property, the interest of this thesis, the devices are run in pulsed mode to try to eliminate any effects due to this. The absence of significant heating during the pulsed measurements has been verified by repeating a measurement with different pulse lengths and repetition rates and checking for any heating induced differences in threshold current and wavelength.

If the light scale is calibrated as described below to obtain the output power, P , as a function of current, then this allows calculation and comparison of the overall (wall plug) and differential quantum (slope) efficiencies of the different lasers. The differential quantum efficiency, η_d is given by Equation 2.3 where q is the electron charge and ν the frequency of the laser light emitted.

$$\eta_d = \left[\frac{q}{h\nu} \right] \frac{dP}{dI} \quad \text{for} \quad (I > I_{th})$$

Equation 2.3

If these measurements are made as a function of temperature and/or length then additional information can be gained.

In the case of multiple lengths then it becomes possible to make a calculation of the net internal optical loss, the internal differential quantum efficiency and the threshold modal gain^[25] although it is more accurate to use the multisection method as described in section 2.4. The net internal optical modal loss, α_i and the internal differential quantum efficiency, η_i can be calculated by plotting the reciprocal differential quantum efficiency versus length for a number of devices. The values of α_i and η_i can be calculated from the gradient and intercept respectively as shown in Equation 2.4.

$$\frac{1}{\eta_d} = \frac{\alpha_i}{\eta_d \ln\left(\frac{1}{R}\right)} L + \frac{1}{\eta_i}$$

Equation 2.4

The threshold modal gain is defined as being equal to the sum of the net optical loss and the mirror loss as shown in Equation 2.5, repeated from Equation 1.8.

$$G_{th} = \alpha_i + \frac{\ln\left(\frac{1}{R}\right)}{L}$$

Equation 2.5

2.3.2 EXPERIMENTAL METHOD

As the measurement of the light-current characteristics is performed in pulsed mode then it is necessary to measure the current, voltage and light using a boxcar. This piece of apparatus allows measurement of the experimental parameters only during defined measurement time windows. These time windows are aligned within the current pulse by use of a multiple channel oscilloscope. The average value within the measurement window is then transmitted to the computer by the boxcar.

The light is measured by a silicon photodetector placed immediately above the device. If the device is placed at a fixed distance and in a fixed position relative to the photodetector, then it is possible to calibrate the light scale using the known photodetector response and knowing the emission wavelength of the laser (see section 2.2). The photodetector response is shown in Figure 2.12. It can be seen that the photodetector response is changing rapidly within the wavelength range of the lasers measured in this thesis ($\sim 1000\text{nm}$) therefore an accurate wavelength measurement is essential for this calibration.

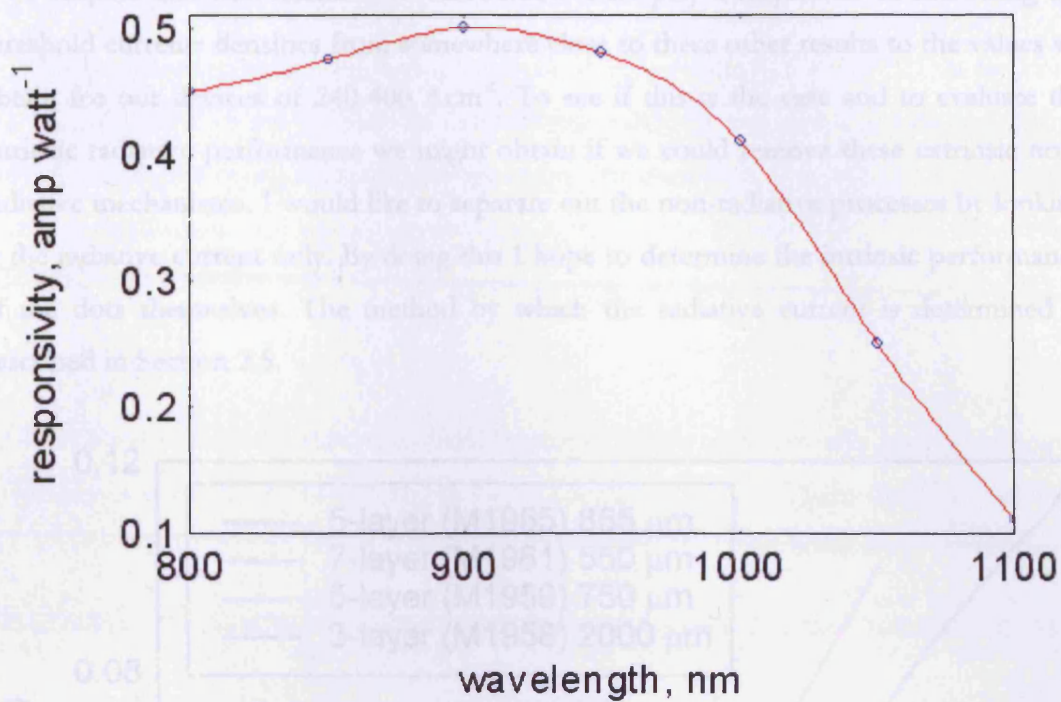


Figure 2.12 The spectral response of the Si detector used in the measurements

2.3.3 RESULTS

Shown below (Figure 2.13) are some example light current curves for a selection of our quantum dot structures. With extremely low threshold current densities of 24 and 25 Acm^{-2} being reported in the literature^[35-37] it can be seen that our threshold current densities are larger than the best devices. However, although these were also DWELL structures, the devices used were 19.2mm long and 14mm respectively, almost ten times the maximum device length of 2mm that we have measured. Slightly higher threshold current densities of 26 Acm^{-2} have been reported by G.T Liu et al^[38] with shorter devices of 7.8mm. More recent results for dots emitting at 1.3 μm demonstrate that even for shorter 5mm long devices with uncoated facets, threshold current densities as low as 32.5 Acm^{-2} can be achieved^[39].

I suspect that non-radiative recombination must play a major role in increasing the threshold currents densities from somewhere close to these other results to the values we obtain for our devices of 240-400 Acm^{-2} . To see if this is the case and to evaluate the intrinsic radiative performance we might obtain if we could remove these extrinsic non-radiative mechanisms, I would like to separate out the non-radiative processes by looking at the radiative current only. By doing this I hope to determine the intrinsic performance of the dots themselves. The method by which the radiative current is determined is described in Section 2.5.

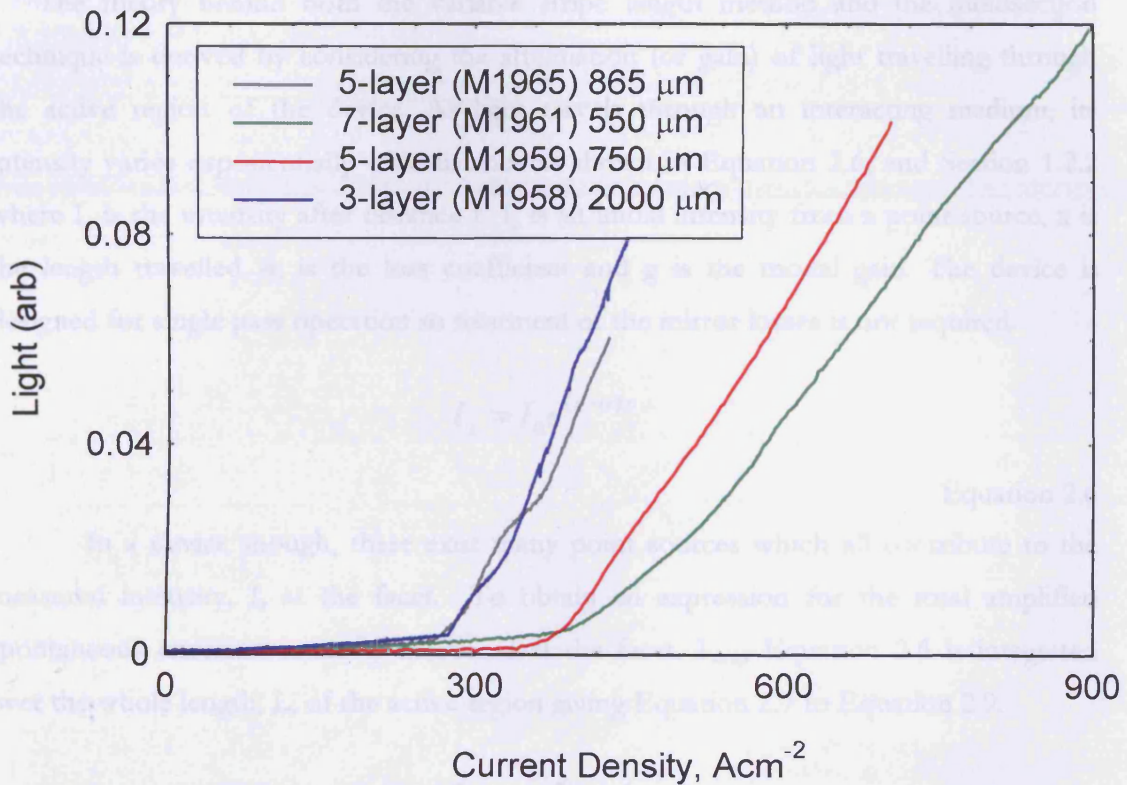


Figure 2.13 Light vs. current density for a selection of devices

2.4 THE MULTISECTION TECHNIQUE AND APPLICATIONS

The multisection technique was developed by co-workers in Cardiff^[40]. It is based on the variable stripe length method of determining gain^[41, 42], but with the advantage of all the measurements being taken on a single chip. The approach does not require as high a wavelength resolution as the Hakki-Paoli gain measurement technique^[43], which needs a resolution of the order of 0.5\AA ^[44] compared to only 10\AA for the multisection technique.

2.4.1 THEORY

The theory behind both the variable stripe length method and the multisection technique is derived by considering the attenuation (or gain) of light travelling through the active region of the device. As light travels through an interacting medium, its intensity varies exponentially with distance as shown in Equation 2.6, and Section 1.2.2 where I_x is the intensity after distance x , I_0 is an initial intensity from a point source, x is the length travelled, α_i is the loss coefficient and g is the modal gain. The device is designed for single pass operation so treatment of the mirror losses is not required.

$$I_x = I_0 e^{(g-\alpha)x}$$

Equation 2.6

In a device though, there exist many point sources which all contribute to the measured intensity, I , at the facet. To obtain an expression for the total amplified spontaneous emission intensity measured at the facet, I_{ASE} , Equation 2.6 is integrated over the whole length, L , of the active region giving Equation 2.7 to Equation 2.9.

$$I_{ASE} = \int_0^L I_x = \int_0^L I_0 e^{(g-\alpha_i)x} dx$$

Equation 2.7

$$I_{ASE} = I_0 \left[\frac{e^{(g-\alpha_i)x}}{(g-\alpha_i)} \right]_0^L$$

Equation 2.8

$$I_{ASE} = \frac{I_0}{(g-\alpha_i)} (e^{(g-\alpha_i)L} - 1)$$

Equation 2.9

By measuring this amplified spontaneous emission spectrum for two or more different lengths, L , the gain, g , losses, α_i , and unamplified spontaneous emission, I_0 can be derived.

2.4.2 EXPERIMENTAL DETAILS

The Fabry-Perot laser structure described earlier in Section 2.1.4 is modified by etching the top contact into equal sized sections. Angled facets and an absorber region at the back are used to ensure a single pass measurement. A window can be etched in the top of the device to allow a check to be made of the pumping levels of the sections. For the equations below to be valid, the length of the sections used and the pumping levels of these sections must be the same. For the measurements performed in this work, only the front two sections need to be contacted with the gold wire. The devices are mounted on a copper header as before and are run in pulsed mode to reduce heating. The device structure is illustrated in Figure 2.14.

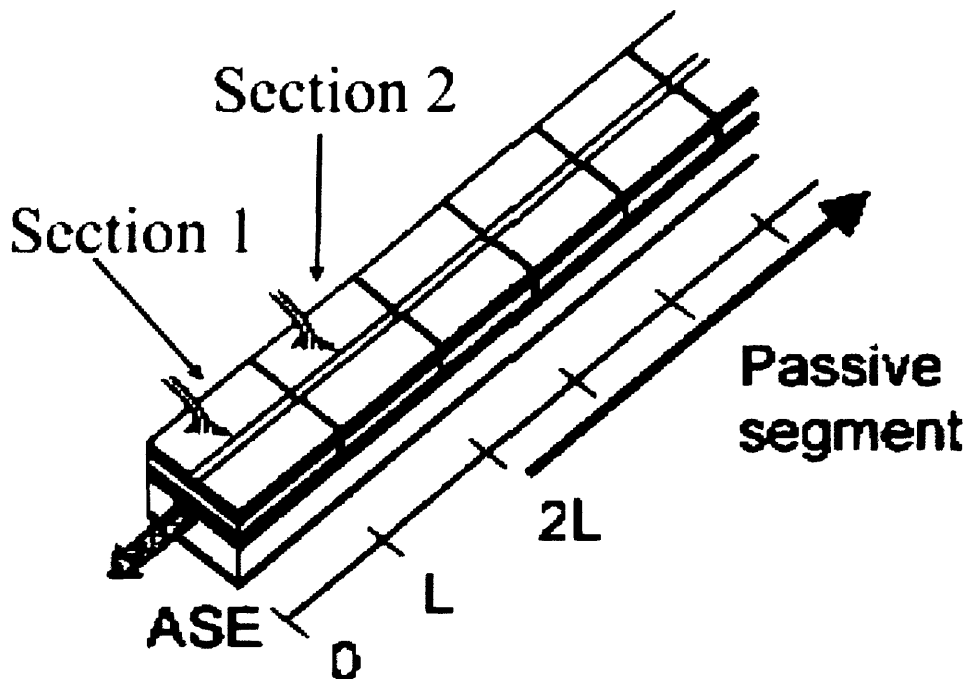


Figure 2.14 Schematic diagram of the multisection device used for measurements of the gain, loss and unamplified spontaneous emission spectra^[40]

To apply the currents and measure the light emitted, the experimental apparatus used is similar to that described in Section 2.2 for the standard spectral measurements but with the addition of a second current supply for section 2. For each current range in use, the currents for the two sections are carefully calibrated using a current probe.

A gated photon counter is used for measuring the light instead of the boxcar due to the small light signal levels present in spontaneous emission. The speed of measurement is set from the computer. This controls the signal to noise ratio as it determines for how long the photon counter averages. The standard settings are fast (2seconds), medium (20seconds), slow (200seconds). The signal to noise ratio is proportional to the square root of the time as shown in Equation 2.10. For the standard time settings above, the signal to noise ratio is increased by a factor of $\sqrt{10}$ or 3.16 for each step. This in turn means that we need the signal to increase by a factor of approximately three in order to reduce the measurement time by one step.

$$S/N \propto \sqrt{T}$$

Equation 2.10

The current pulses and measurement gates are set up using an oscilloscope and are illustrated in Figure 2.15 and Figure 2.16 below. For the gain measurements, the front section is pumped using a double length pulse with the second section only being pumped during the latter half of this. This allows the amplified spontaneous emission to be collected almost instantaneously when both the front section only and the front two sections are being pumped. These measurements are necessary to derive the gain as described in Equation 2.11. For the loss measurements, first the front section is pumped, then the second section. The gates are arranged such that the light gates are set within the current gates, as the photon counter is the most sensitive and this avoids interference from the rapidly varying current pulses.

If we measure the light emitted from the facet when only the front section is pumped this gives us the initial intensity, which as the sections are all identical will be the same for any section of the device.

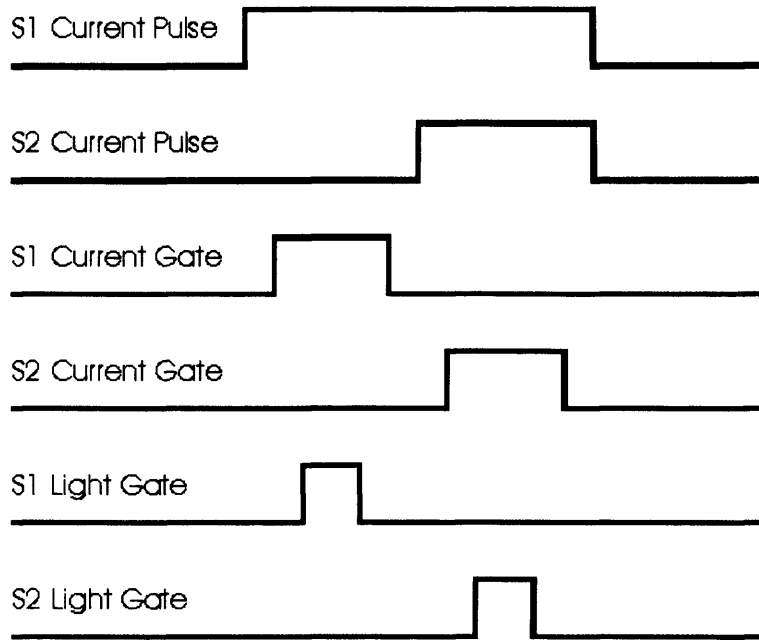


Figure 2.15 Current pulses and measurement gates for gain measurements

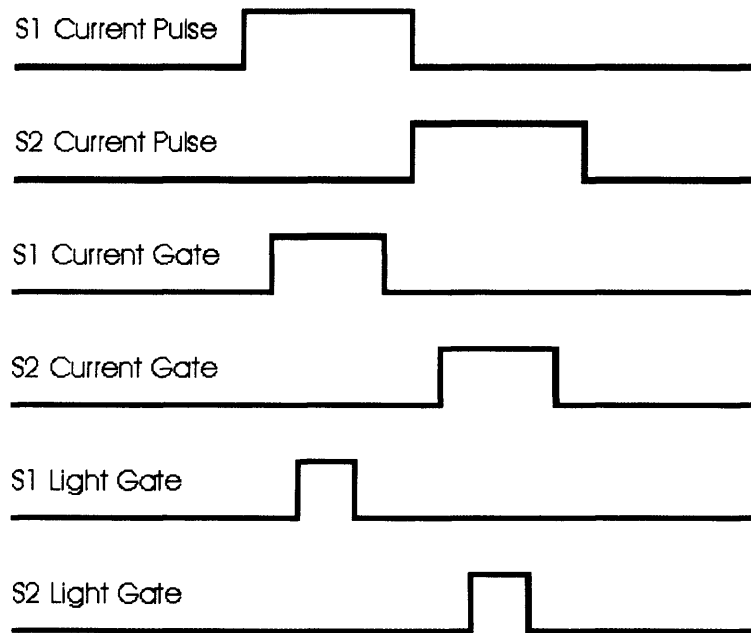


Figure 2.16 Current pulses and measurement gates for loss measurements

2.4.3 NET GAIN

To measure the net modal gain the front section is first pumped to provide a reference spectrum I_1 . Both sections are then pumped together to the same current density to give a signal I_{1+2} . In this configuration, the front section then provides gain to the light travelling through from the 'identical' back section. This gain can be calculated using Equation 2.11 where L is the section length. In this equation, the gain calculated is the net modal gain. To get the total modal gain you must add on the modal loss, the calculation of which is described in the next section.

$$gain = (G - \alpha_i) = \ln\left(\frac{I_{1+2}}{I_1} - 1\right) / L$$

Equation 2.11

An example of the raw data spectra and the calculated gain spectrum is shown in Figure 2.17.

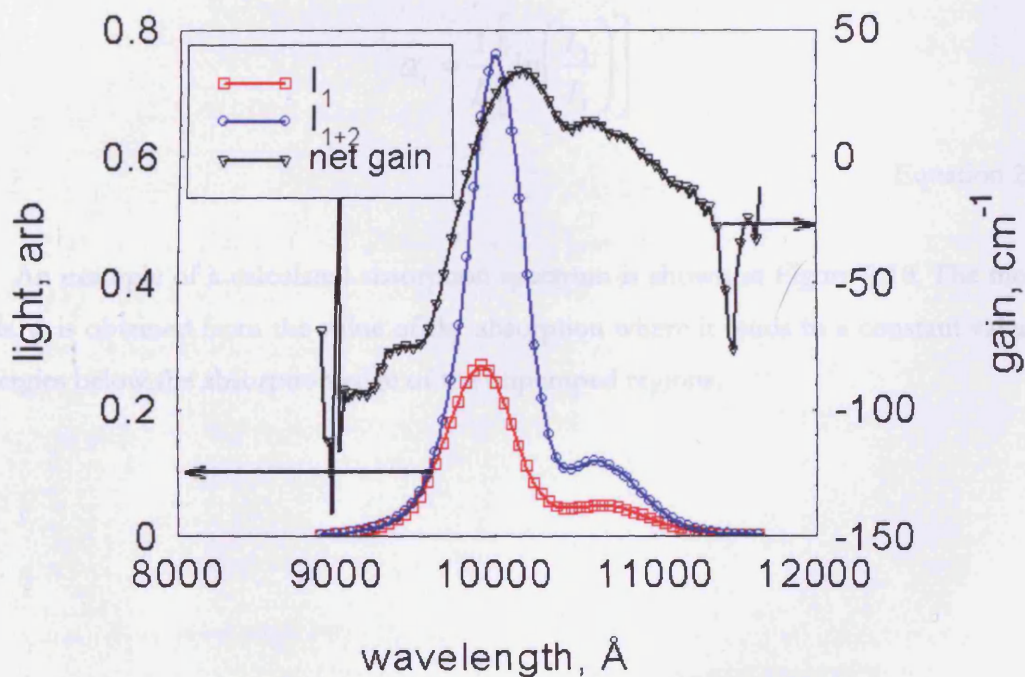


Figure 2.17 Example amplified spontaneous emission and gain spectra for a seven-layer quantum dot structure taken with a drive current of 150mA

2.4.4 LOSS

Many-body effects within pumped sections cause emission at energies below the absorption edge of the unpumped regions. As this emission is guided along the device it is attenuated only by internal scattering – this allows us to calculate the internal loss coefficient α_i using Equation 2.6, where gain (absorption) equals zero, by plotting the natural log of the transmitted intensity against the length of unpumped section. The gradient is equal to α_i .

By a similar method to that used for the gain, we can spectrally resolve the absorption by comparing the ASE intensity from any two measurements with different unpumped lengths but the same pumped length. The simplest way of doing this is to take the ASE spectra when pumping first the front section only to provide a reference signal, I_1 and then the second section only to the same current density, I_2 and use Equation 2.12. The absorption can be calculated by measuring the light transmitted through the absorbing front section of the device from the ‘identical’ back section, I_2 .

$$\alpha_i = \frac{1}{L} \left[\ln \left(\frac{I_2}{I_1} \right) \right]$$

Equation 2.12

An example of a calculated absorption spectrum is shown in Figure 2.18. The modal loss, α_i is obtained from the value of the absorption where it tends to a constant value at energies below the absorption edge of the unpumped regions.

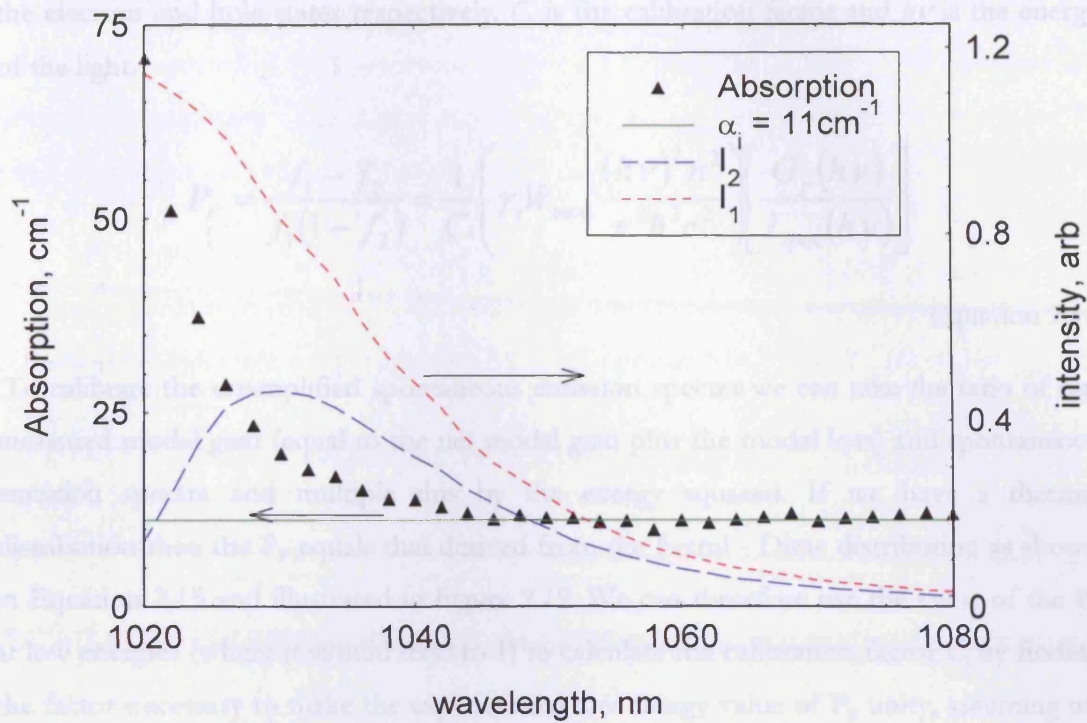


Figure 2.18 Example absorption spectrum for a quantum well device, showing the measured amplified spontaneous emission spectra and the value of the loss fitted at long wavelengths

2.4.5 UNAMPLIFIED SPONTANEOUS EMISSION AND P_F FACTOR

The unamplified spontaneous emission can also be found by transforming the same data taken for the gain using Equation 2.13. This equation allows us to correct the measured amplified spontaneous emission for the effects of gain and absorption along the cavity, hence allowing us to extract the true spontaneous emission.

$$I_{\text{spon}} = \left[\ln \left(\frac{I_{1+2}}{I_1} - 1 \right) / L \right] \times \left[\frac{I_1^2}{I_{1+2} - 2I_1} \right]$$

Equation 2.13

However, although though this gives the correct shape for the spontaneous emission it is in arbitrary units that are dependent on the units of I_1 and I_{1+2} , which are in arbitrary units due to the unknown proportion of light detected in the experiment. To calibrate this collection factor we can make use of the inversion factor, P_F . This is calculated as shown in Equation 2.14 where $G_p(h\nu)$ is the modal gain (which is the measured net modal gain spectrum with the addition of the loss) and $I_{\text{spon}}(h\nu)$ is the uncalibrated unamplified spontaneous emission spectrum. The symbols f_1 and f_2 are the occupation probabilities of

the electron and hole states respectively, C_i is the calibration factor and $h\nu$ is the energy of the light.

$$P_F = \frac{f_1 - f_2}{f_1(1 - f_2)} = \frac{1}{C_i} \left(\gamma_i W_{\text{mod}} \frac{(h\nu)^2 n^2}{\pi^2 \hbar^3 c^2} \right) \left[\frac{G_p(h\nu)}{I_{\text{spont}}(h\nu)} \right]$$

Equation 2.14

To calibrate the unamplified spontaneous emission spectra we can take the ratio of our measured modal gain (equal to the net modal gain plus the modal loss) and spontaneous emission spectra and multiple this by the energy squared. If we have a thermal distribution then the P_F equals that derived from the Fermi - Dirac distribution as shown in Equation 2.15 and illustrated in Figure 2.19. We can therefore use the value of the P_F at low energies (where it should tend to 1) to calculate the calibration factor C_i by finding the factor necessary to make the experimental low energy value of P_F unity, assuming we either know or can calculate the other constants.

$$P_F = \frac{f_1 - f_2}{f_1(1 - f_2)} = 1 - \exp\left(-\frac{h\nu - \Delta E_f}{kT}\right)$$

Equation 2.15

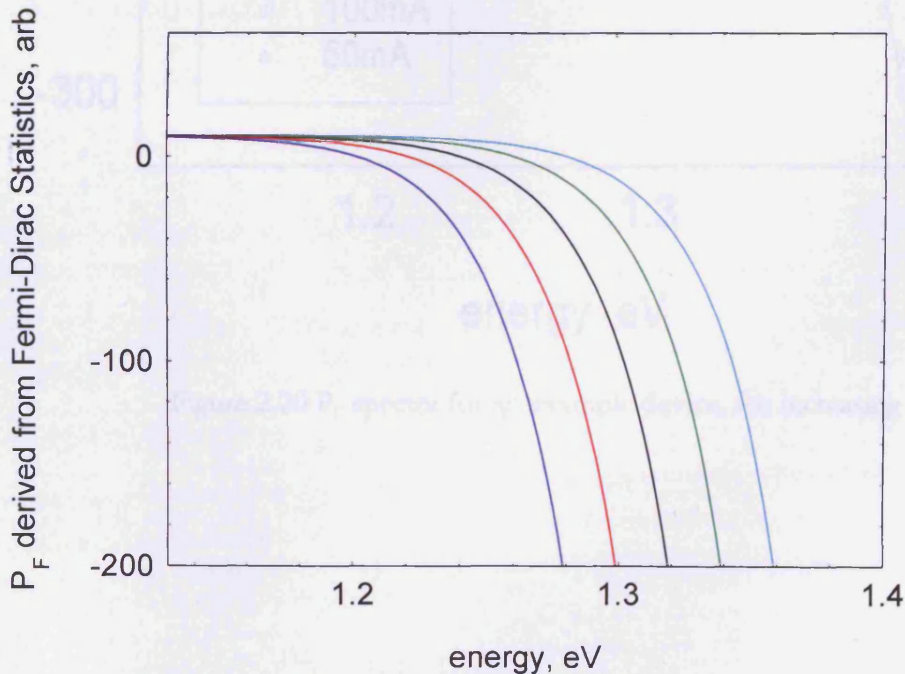


Figure 2.19 Calculated examples of the form of P_F spectra where the occupation of the states follows Fermi-Dirac Statistics. Lines from left to right are for increasing ΔE_f .

If we don't have a thermal distribution, it may still be possible to use this method to calibrate the unamplified spontaneous emission provided that a region can be identified where P_F equals unity. This region can be identified by a region where the measured P_F takes its maximum value *and* saturates with respect to increasing current^[45]. Sample P_F spectra are shown in Figure 2.20

The calibration factor C_i can then be used to normalise the unamplified spontaneous emission spectra as shown in Equation 2.16 and illustrated in Figure 2.21.

$$R_{\text{spont}}(h\nu) = C_i \times I_{\text{spont}}(h\nu)$$

Equation 2.16

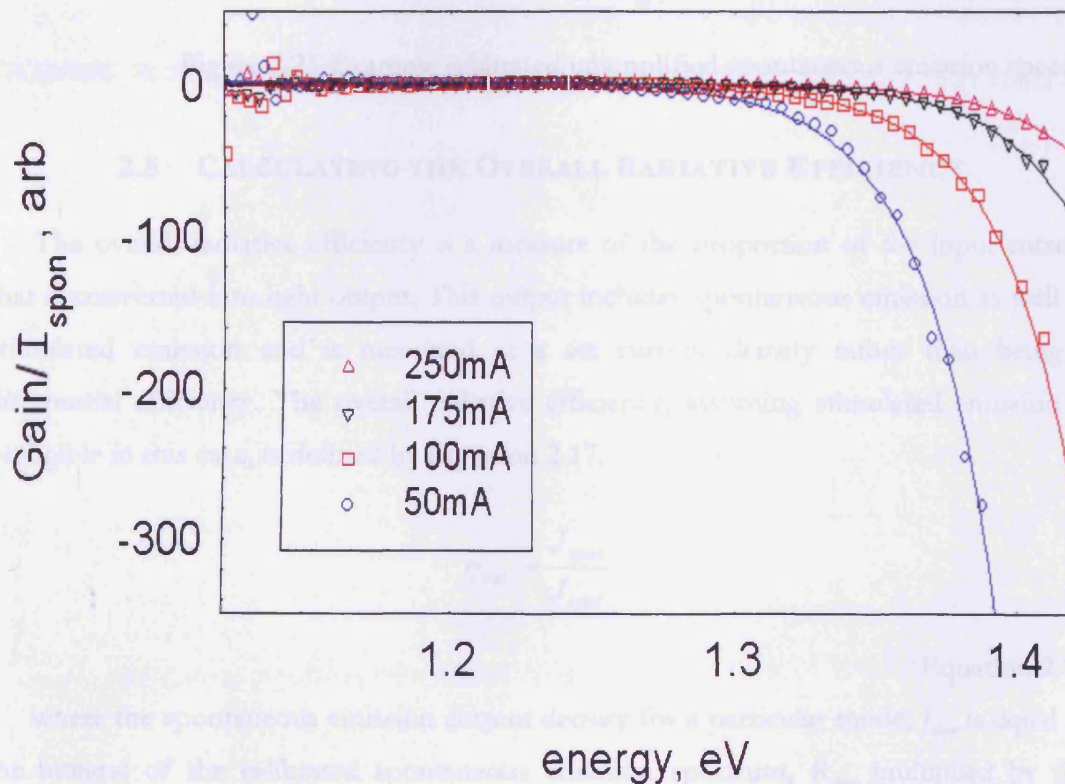


Figure 2.20 P_F spectra for an example device, for increasing currents

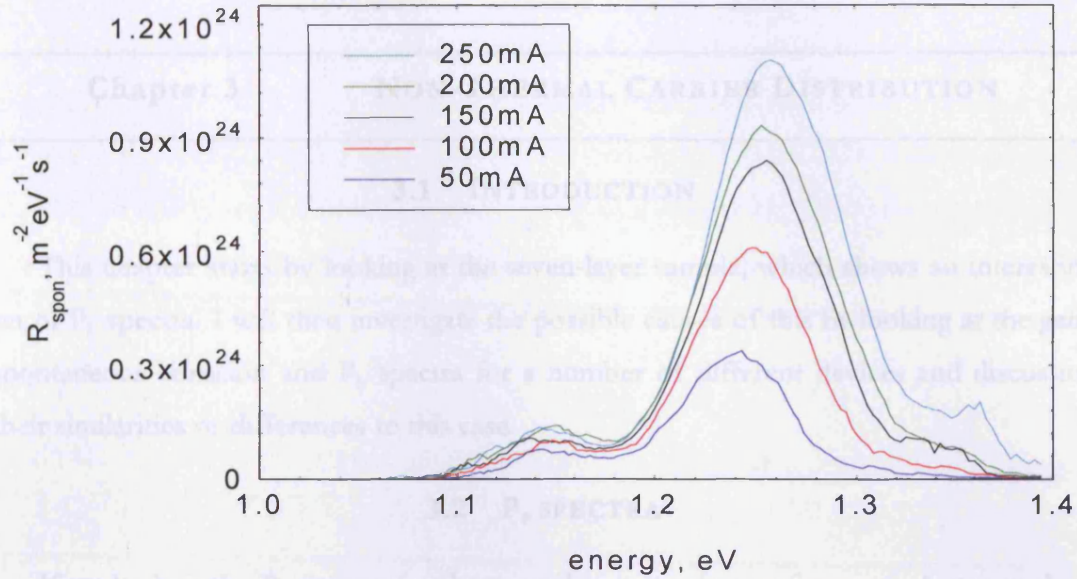


Figure 2.21 Example calibrated unamplified spontaneous emission spectra

2.5 CALCULATING THE OVERALL RADIATIVE EFFICIENCY

The overall radiative efficiency is a measure of the proportion of the input current that is converted into light output. This output includes spontaneous emission as well as stimulated emission and is measured at a set current density rather than being a differential efficiency. The overall radiative efficiency, assuming stimulated emission is negligible in this case, is defined by Equation 2.17.

$$\eta_{rad} = \frac{J_{spon}}{J_{total}}$$

Equation 2.17

where the spontaneous emission current density for a particular mode, J_{spon} is equal to the integral of the calibrated spontaneous emission spectrum, R_{spon} multiplied by the electronic charge.

$$J_{spon} = e \int I_{spon} d(h\nu)$$

Equation 2.18

3.1 INTRODUCTION

This chapter starts by looking at the seven-layer sample, which shows an interesting set of P_F spectra. I will then investigate the possible causes of this by looking at the gain, spontaneous emission and P_F spectra for a number of different devices and discussing their similarities or differences to this case.

3.2 P_F SPECTRA

If we look at the P_F spectra for the seven-layer sample as a function of current there are several interesting points to note (see Figure 3.1).

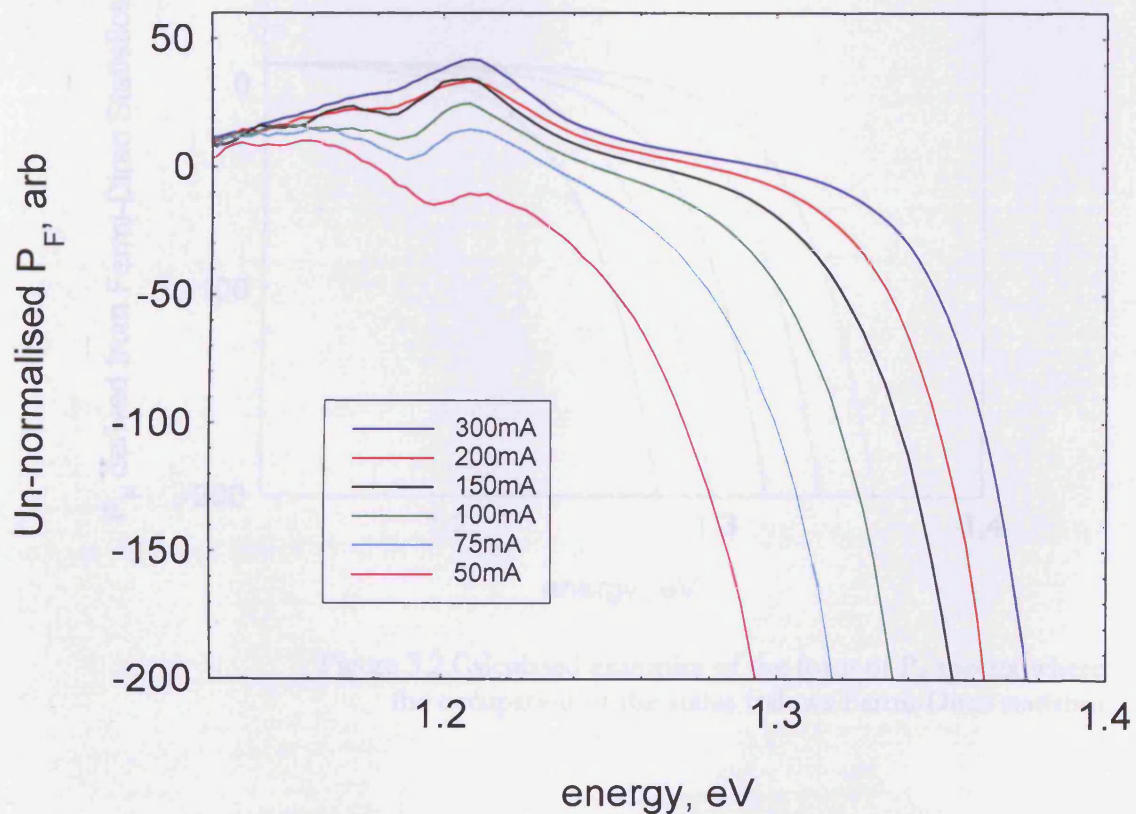


Figure 3.1 P_F Spectra for the seven-layer sample, measured at 300K

It is clear that the sample is not in full thermal equilibrium, as at lower energies the P_F does not resemble that given by Fermi Dirac statistics (see Equation 3.1, repeated from Section 2.4.5 and illustrated in Figure 3.2). It can also be seen that there is no easily identifiable energy region in which the P_F tends to a maximum value that saturates with increasing current^[45]. As such, it is unclear how we can use this P_F to calibrate the spontaneous emission spectra and hence obtain the intrinsic performance of the sample using the method in Section 2.4.5.

$$P_F = \frac{f_1 - f_2}{f_1(1 - f_2)} = 1 - \exp\left(\frac{h\nu - \Delta E_f}{kT}\right)$$

Equation 3.1

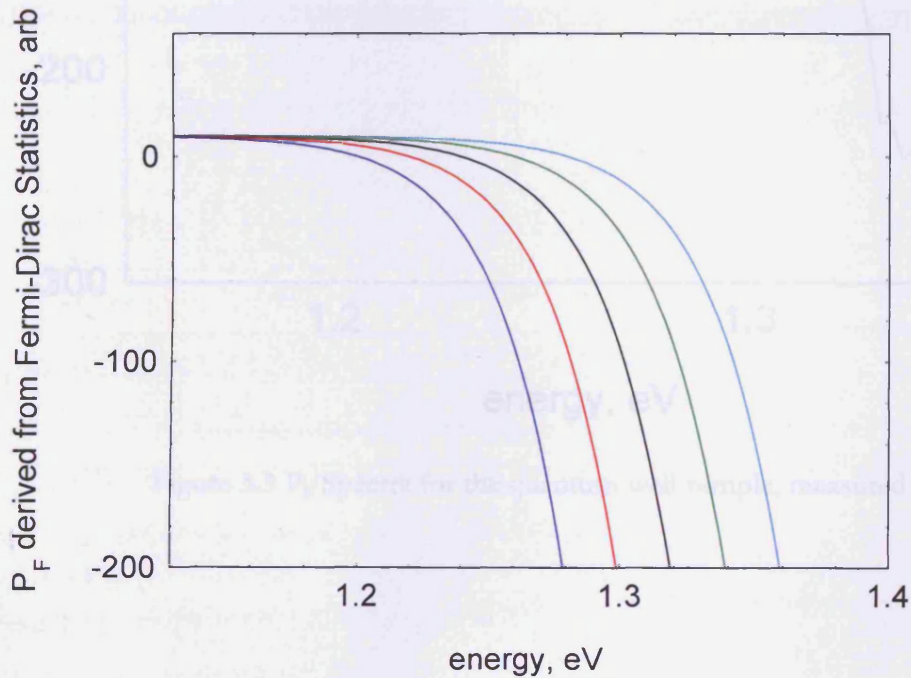


Figure 3.2 Calculated examples of the form of P_F spectra where the occupation of the states follows Fermi-Dirac statistics

Other samples, such as the quantum well sample and the three-layer quantum dot layer sample do show 'normal' P_F spectra as illustrated in Figure 3.3 and Figure 3.4 respectively. At low energies, the spectra are noisy due to the very low light levels.

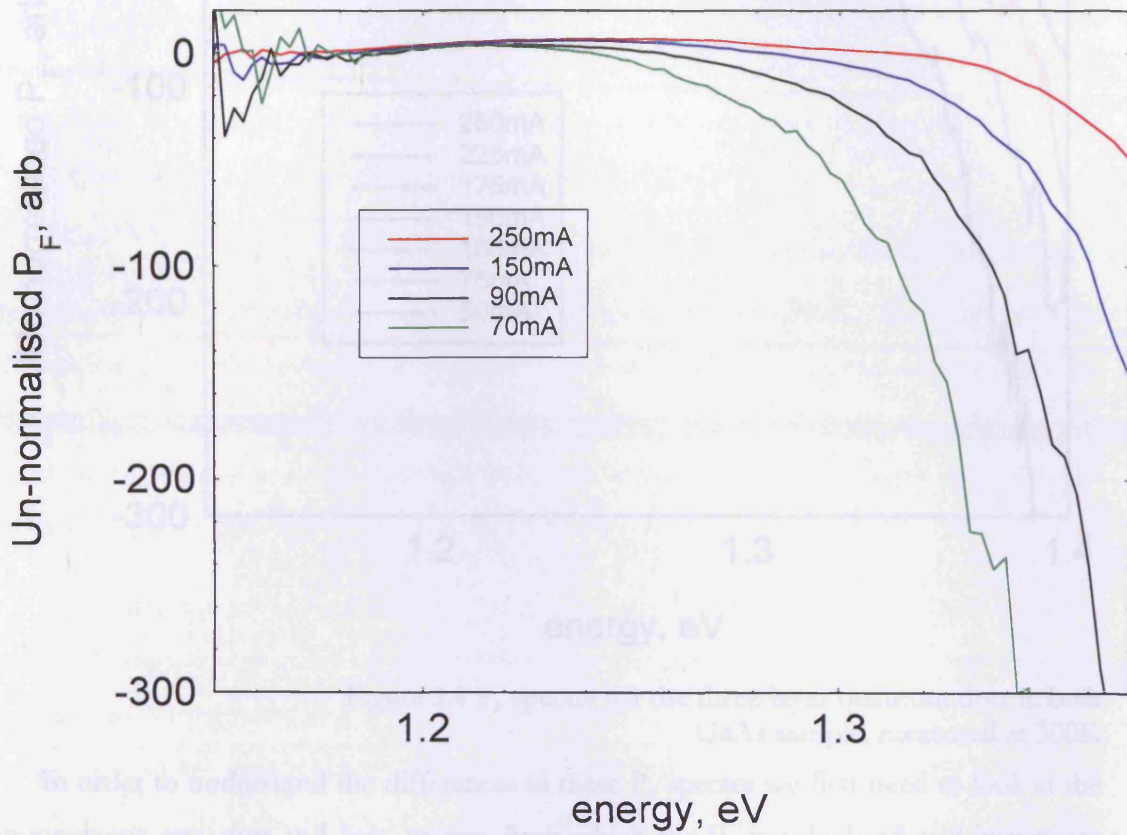


Figure 3.3 P_F Spectra for the quantum well sample, measured at 300K

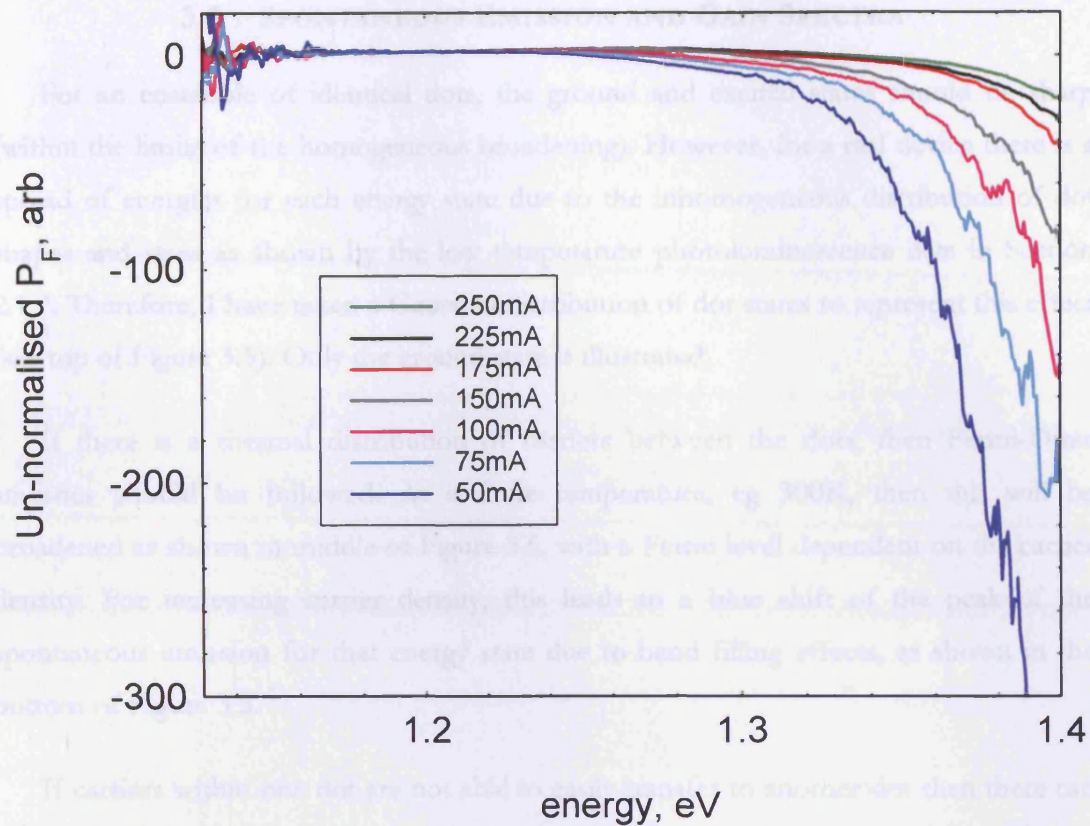


Figure 3.4 P_F spectra for the three-layer quantum dots in bulk GaAs sample, measured at 300K

In order to understand the differences in these P_F spectra we first need to look at the spontaneous emission and gain spectra from which the P_F is calculated and investigate how these should look when the population of the states follows Fermi-Dirac statistics and how they might look for other carrier distributions.

The gain spectra should show similar trends as the increasing current as the spontaneous emission.

3.3 SPONTANEOUS EMISSION AND GAIN SPECTRA

For an ensemble of identical dots, the ground and excited states should be sharp (within the limits of the homogeneous broadening). However, for a real device there is a spread of energies for each energy state due to the inhomogeneous distribution of dot shapes and sizes as shown by the low temperature photoluminescence data in Section 2.1.2. Therefore, I have taken a Gaussian distribution of dot states to represent this effect (see top of Figure 3.5). Only the ground state is illustrated.

If there is a thermal distribution of carriers between the dots, then Fermi-Dirac statistics should be followed. At a finite temperature, eg 300K, then this will be broadened as shown in middle of Figure 3.5, with a Fermi level dependent on the carrier density. For increasing carrier density, this leads to a blue shift of the peak of the spontaneous emission for that energy state due to band filling effects, as shown in the bottom of Figure 3.5.

If carriers within one dot are not able to easily transfer to another dot then there can be no thermal distribution of carriers between the various dot states. If for example, carriers can be captured into a dot but cannot subsequently leave that dot, then the dots will be populated according to the carrier capture and recombination rates of dots of different sizes. This could result in equal capture into all dots in which case the dots' energy states will then fill up randomly with increasing carrier density, leading to no net change in wavelength of the peak of the spontaneous emission for that energy state as shown in Figure 3.6. This fixed spectral shape would also be true for any system where the relative carrier density within each dot does not change with increasing injection level, not just where there is equal population of the dots^[46].

The gain spectra should show similar trends with increasing current as the spontaneous emission.

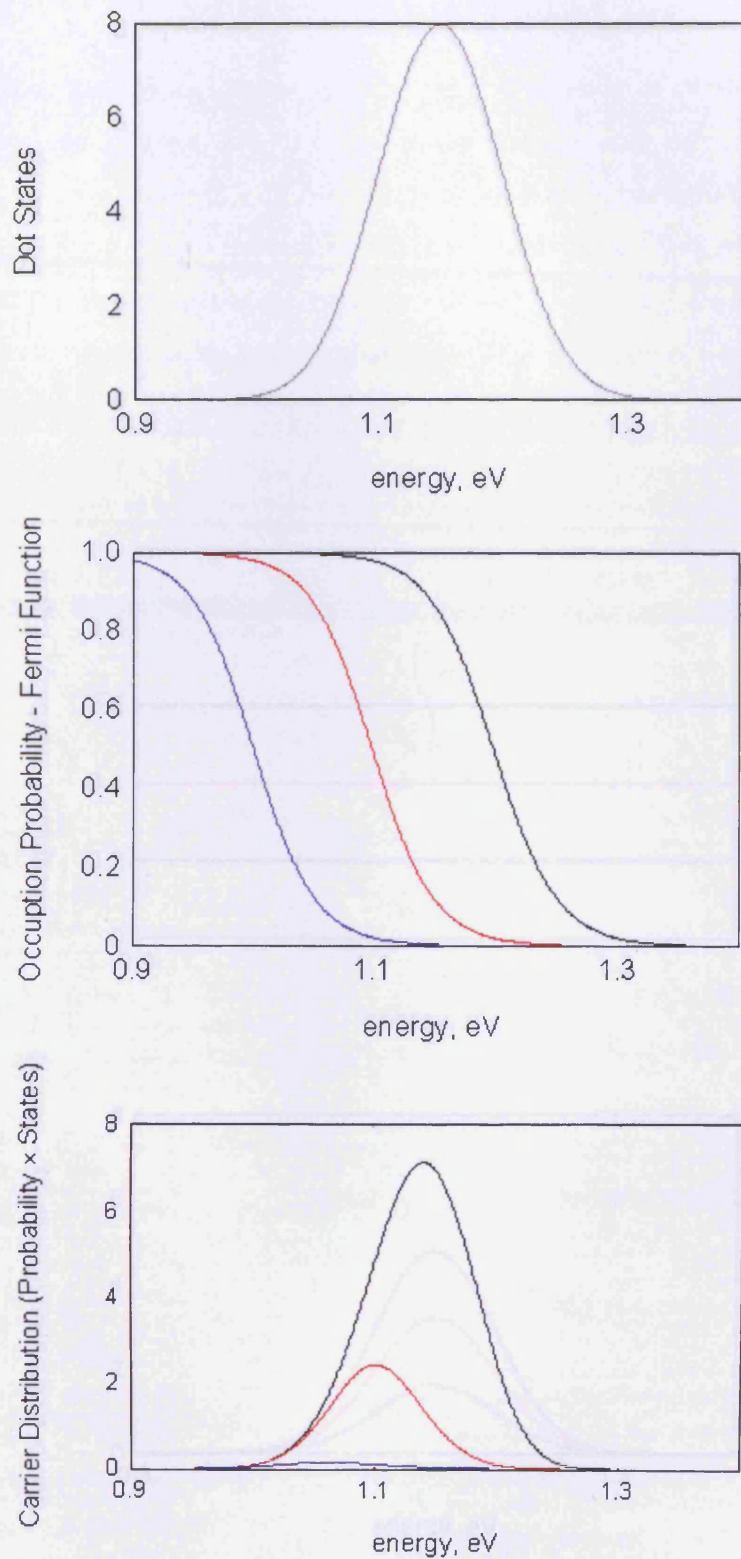


Figure 3.5 Illustration of the change with increasing carrier density of the occupation probability and carrier distribution showing the shift in peak energy due to band filling

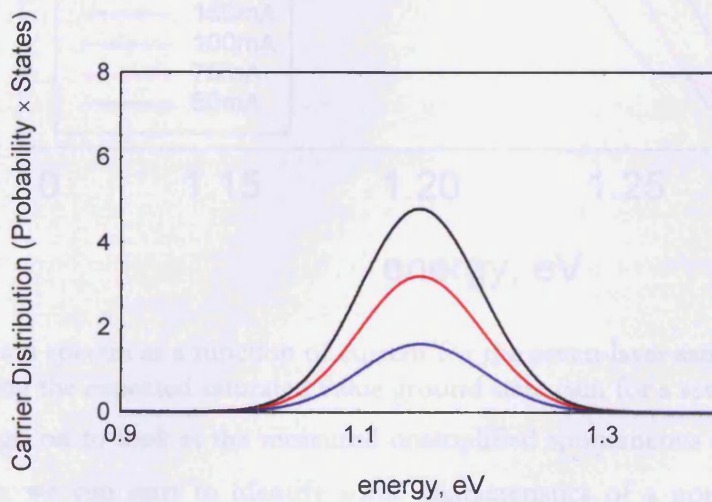
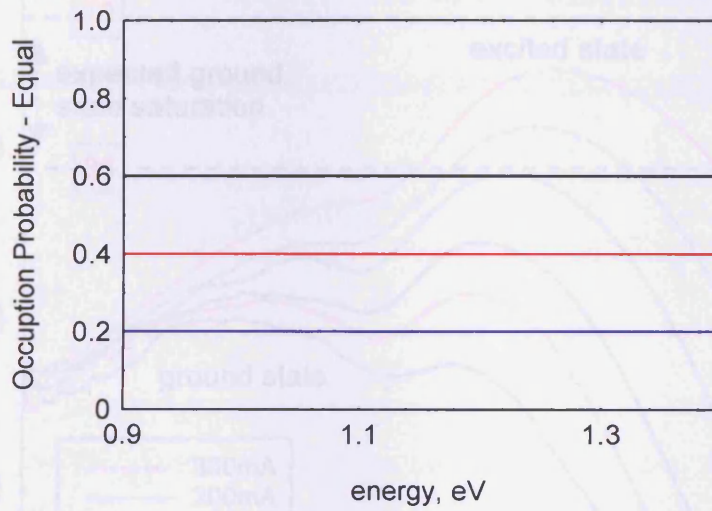
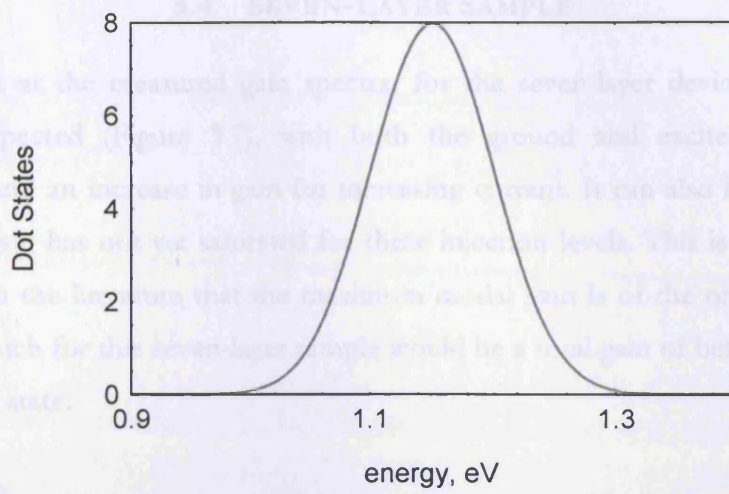


Figure 3.6 Illustration of the change with increasing carrier density of the dot states, occupation probability and carrier distribution where there is equal filling of dot states

3.4 SEVEN-LAYER SAMPLE

If we look at the measured gain spectra, for the seven-layer device they do look broadly as expected (Figure 3.7), with both the ground and excited states clearly distinguished and an increase in gain for increasing current. It can also be seen that the ground state gain has not yet saturated for these injection levels. This is consistent with observations in the literature that the maximum modal gain is of the order of $5\text{-}10\text{cm}^{-1}$ per layer^[27], which for this seven-layer sample would be a total gain of between $35\text{-}70\text{cm}^{-1}$ for the ground state.

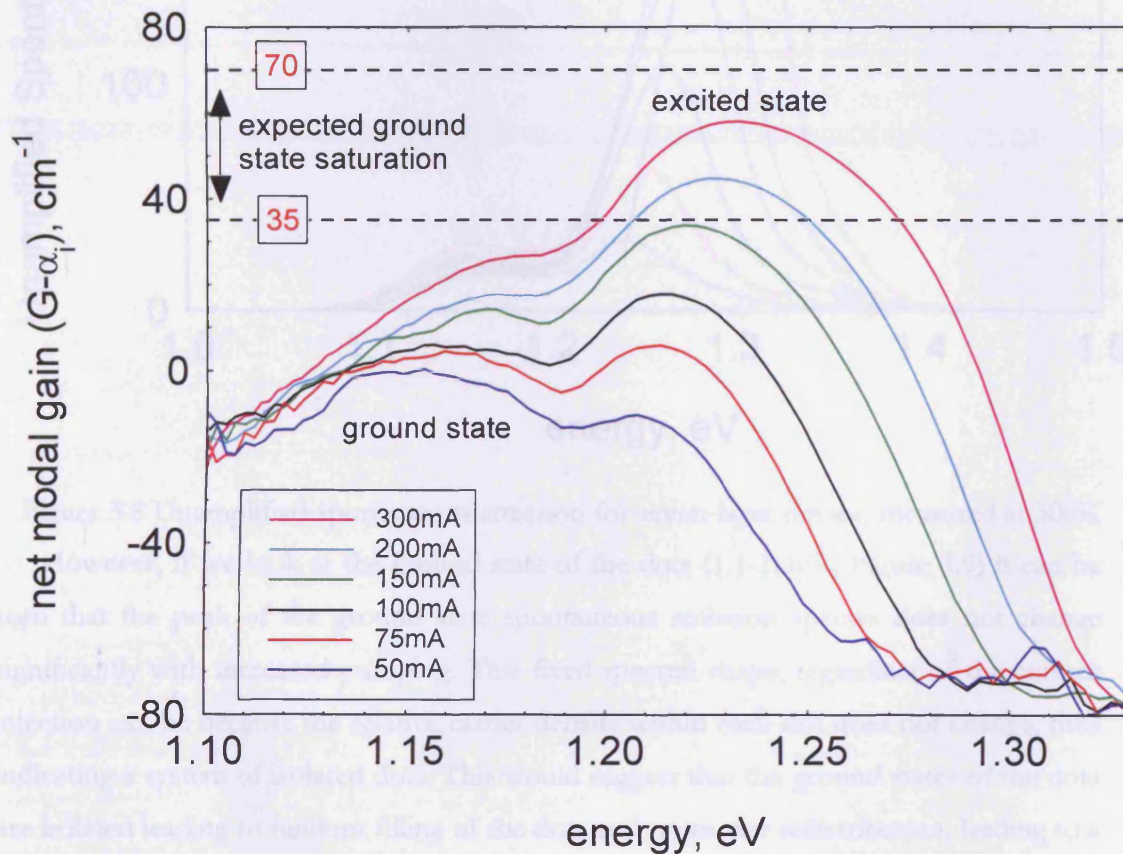


Figure 3.7 Gain spectra as a function of current for the seven-layer sample, with dotted lines indicating the expected saturated value ground state gain for a seven-layer sample.

If we then go on to look at the measured unamplified spontaneous emission spectra for this sample, we can start to identify some characteristics of a non-thermal carrier distribution (Figure 3.8). It can be seen that the peak wavelength of the excited state ($1.20\text{-}1.30\text{eV}$) is behaving as expected for a thermal distribution of carriers with a distinct blue shift as previously described.

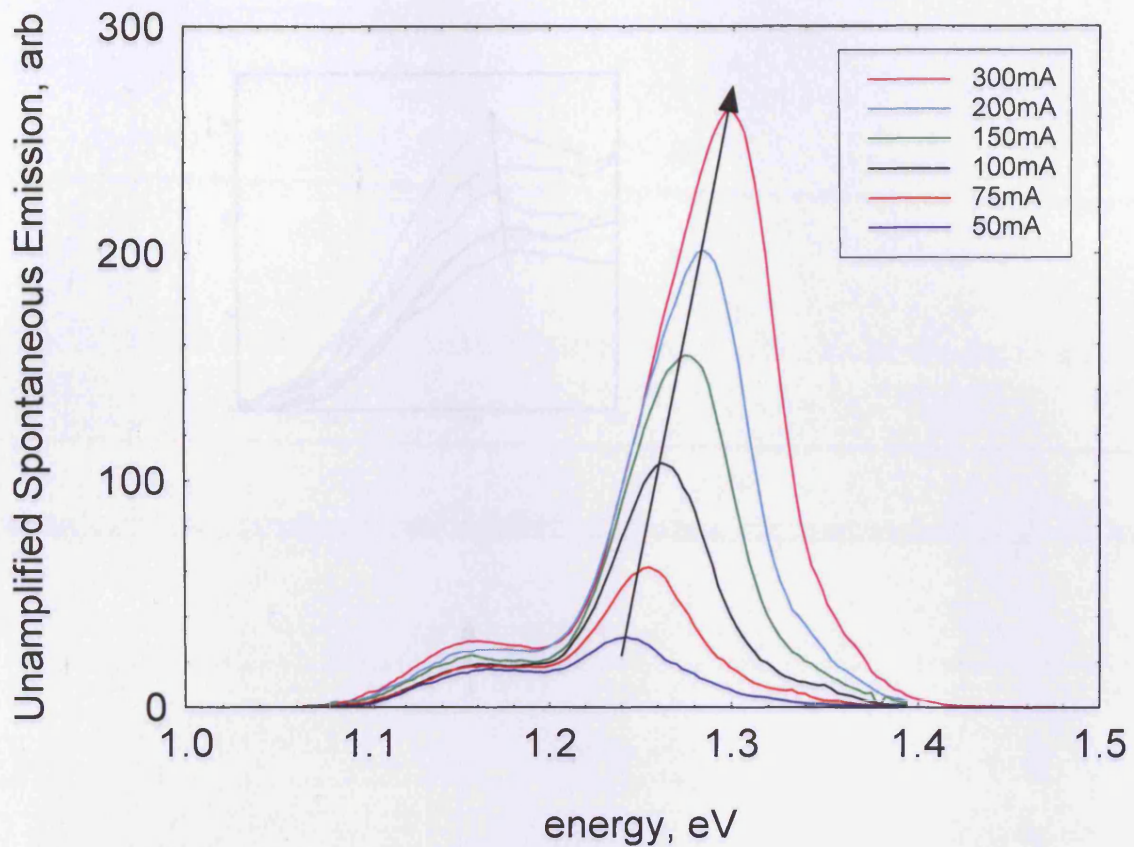


Figure 3.8 Unamplified spontaneous emission for seven-layer device, measured at 300K

However, if we look at the ground state of the dots (1.1-1.2eV, Figure 3.9) it can be seen that the peak of the ground state spontaneous emission spectra does not change significantly with increased pumping. This fixed spectral shape, regardless of the current injection can be because the relative carrier density within each dot does not change, thus indicating a system of isolated dots. This would suggest that the ground states of the dots are isolated leading to random filling of the dots and no carrier redistribution, leading to a non-thermal distribution. The slight red shift highlighted in the inset of Figure 3.9 may be due to many body Coulomb effects narrowing the transition energies of the dots. Such effects should still occur in dot structures due to the presence of carriers in the 2D wetting layer^[47, 48].

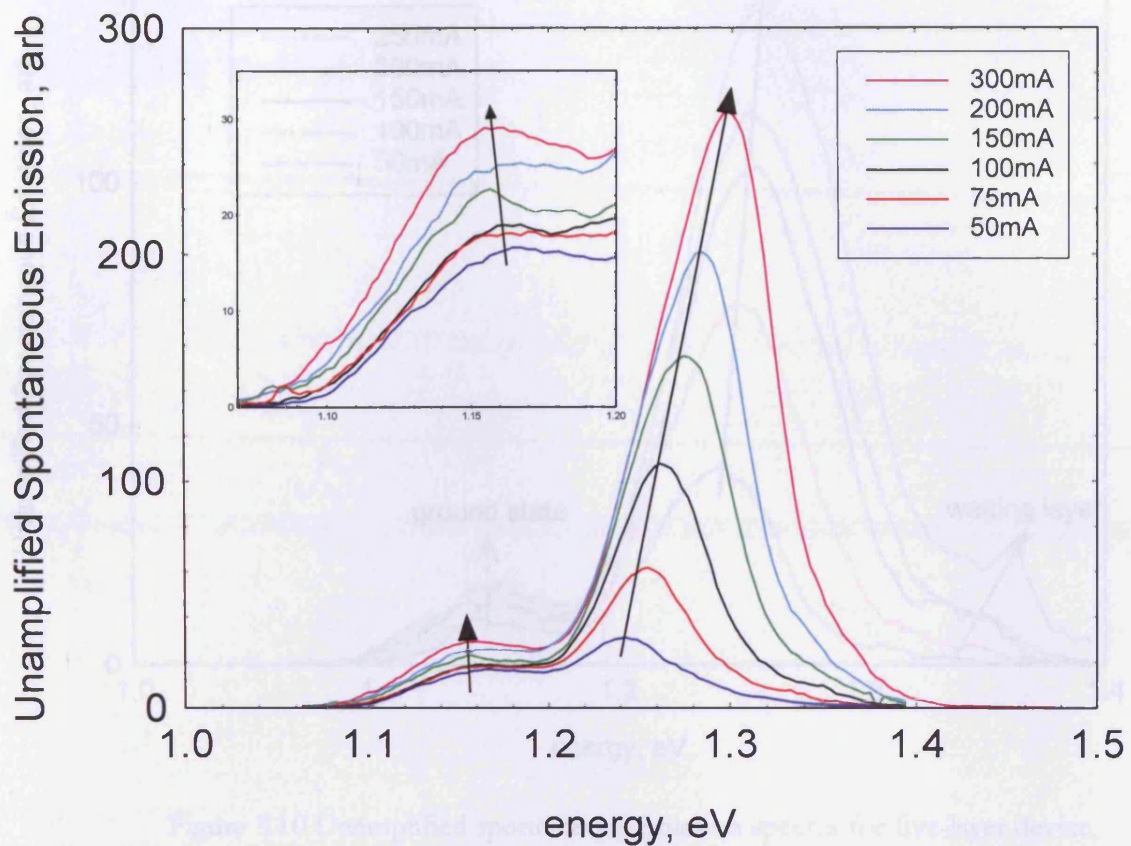


Figure 3.9 Expansion of ground state in Figure 3.8 above

3.5 SUMMARY OF OTHER STRUCTURES MEASURED

The same effect as seen in the seven layer sample, a non-thermal ground state combined with a thermal excited state, can be seen in the spectra taken from the five-layer device as shown in Figure 3.10. It is also possible in this case to distinguish the wetting layer emission, as identified in the figure. This is due to the lower number of dot ground and excited states, due to the fewer dot layers, meaning that the wetting layer becomes occupied at lower total current densities^[49].

The peak emission of the wetting layer appears to increase in energy at a faster rate than the dot excited state. However, this is unlikely to be the case since it would imply that the number of pairs of states per unit energy is smaller in the wetting layer than in the dot excited state.

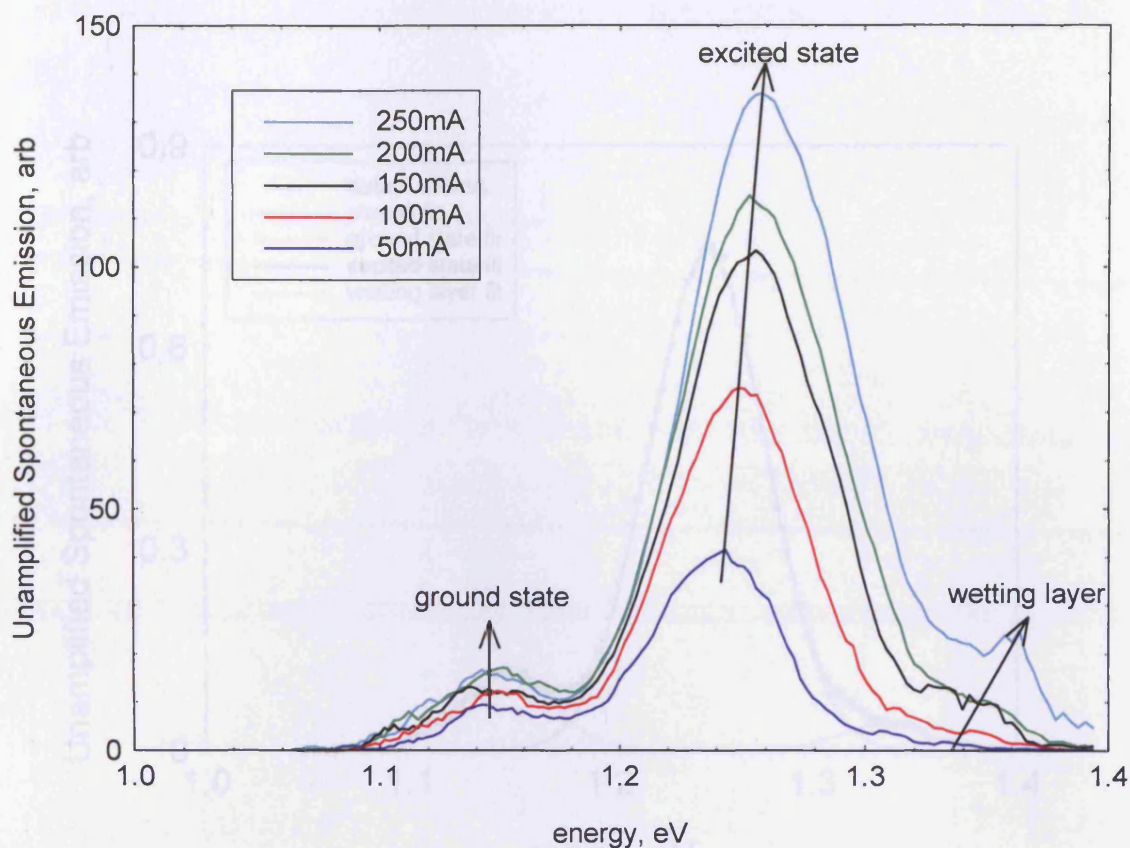


Figure 3.10 Unamplified spontaneous emission spectra for five-layer device, measured at 300K

To look in closer detail, the spontaneous emission spectra have been fitted with multiple Gaussian curves using Origin. This uses a fitting program to determine the combination of Gaussian curves that when summed together gives the best overall fit to the spontaneous emission spectra. This allows accurate determination of the positions of the ground, excited and wetting layer states. An example fit is shown in Figure 3.11 for the 100mA current spectra in Figure 3.10.

From this it is possible to plot the peak energy of the ground state versus the current for a selection of different structures. This comparison is shown in Figure 3.12.

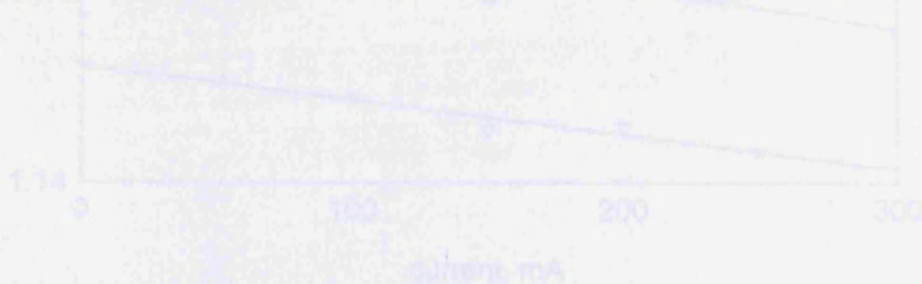


Figure 3.12 Peak energy of the ground state versus the current

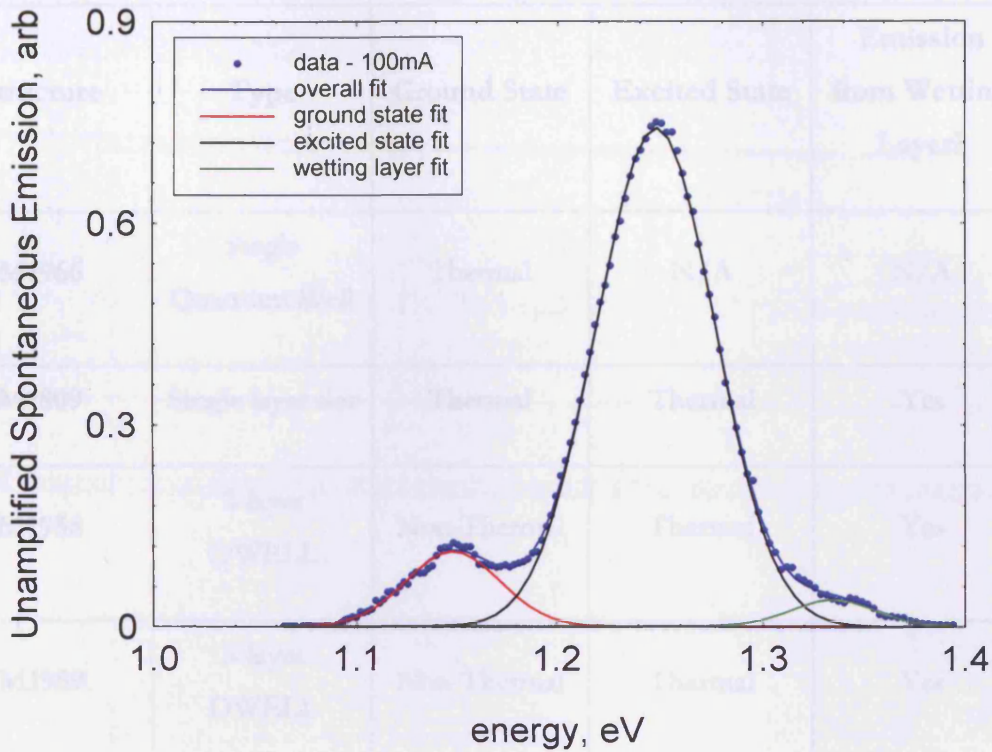


Figure 3.11 Unamplified spontaneous emission spectrum fitted with Gaussian curves

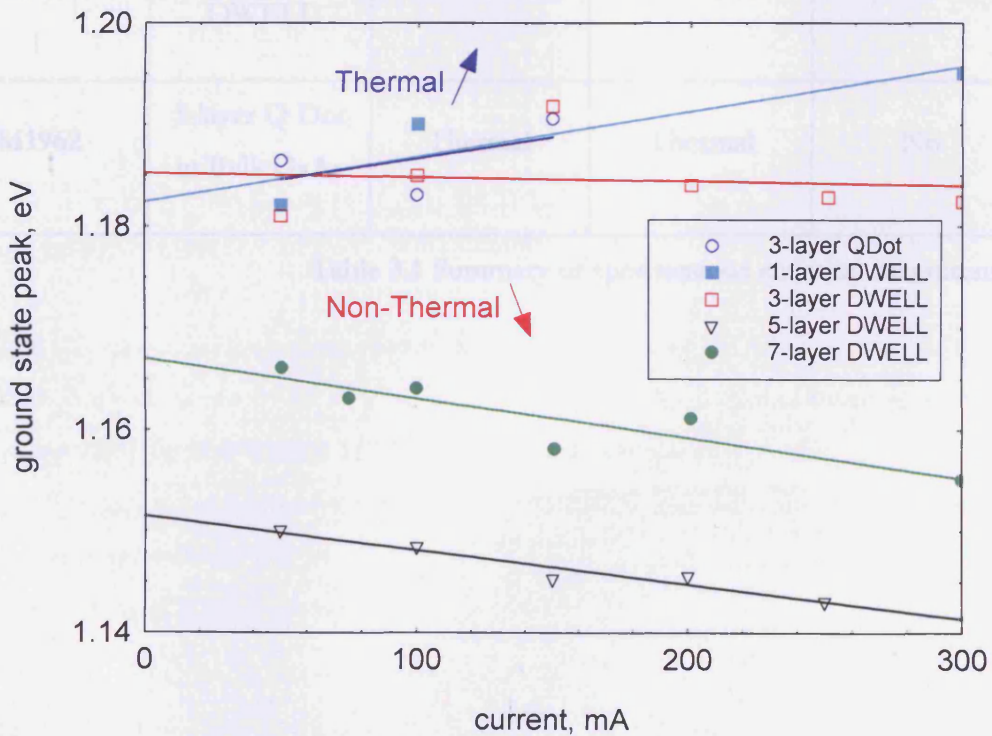


Figure 3.12 Peak energy of the ground state versus the current

The results for all the different structures measured are summarised in Table 3.1 below.

Structure	Type	Ground State	Excited State	Emission from Wetting Layer?
M1966	Single Quantum Well	Thermal	N/A	N/A
M1809	Single layer dot	Thermal	Thermal	Yes
M1958	3-layer DWELL	Non-Thermal	Thermal	Yes
M1959	5-layer DWELL	Non-Thermal	Thermal	Yes
M1961	7-layer DWELL	Non-Thermal	Thermal	No
M1962	3-layer Q Dot in Bulk GaAs	Thermal	Thermal	No

Table 3.1 Summary of spontaneous emission measurements

The one-layer sample appears to be in full thermal equilibrium. Example measured unamplified spontaneous emission spectra for this device are shown in Figure 3.13. It can be seen that the peak wavelengths of both the ground and excited (and wetting layer) states show a clear blue shift.

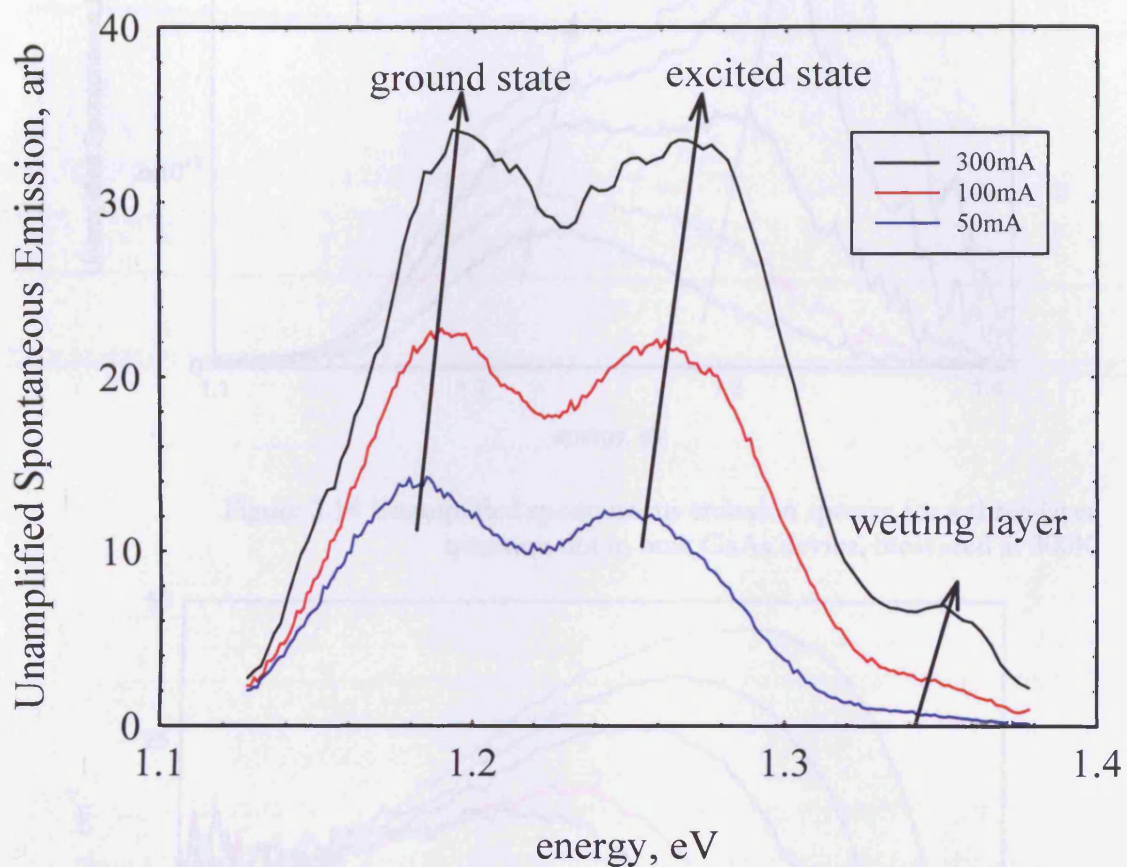


Figure 3.13 Unamplified Spontaneous Emission Spectra for Device with a Single Quantum Dot Layer, measured at 300K

Perhaps more surprising is that a multiple layer sample such as the three-layer quantum dot sample could be in thermal equilibrium as for a global Fermi-level to exist this infers that the layers must be coupled. This is consistent with the modelling of the electronic coupling in Section 2.1.3. The spontaneous emission, gain and P_F spectra are shown in Figure 3.14, Figure 3.15 and Figure 3.16 respectively for the three-layer quantum dot in bulk GaAs sample.

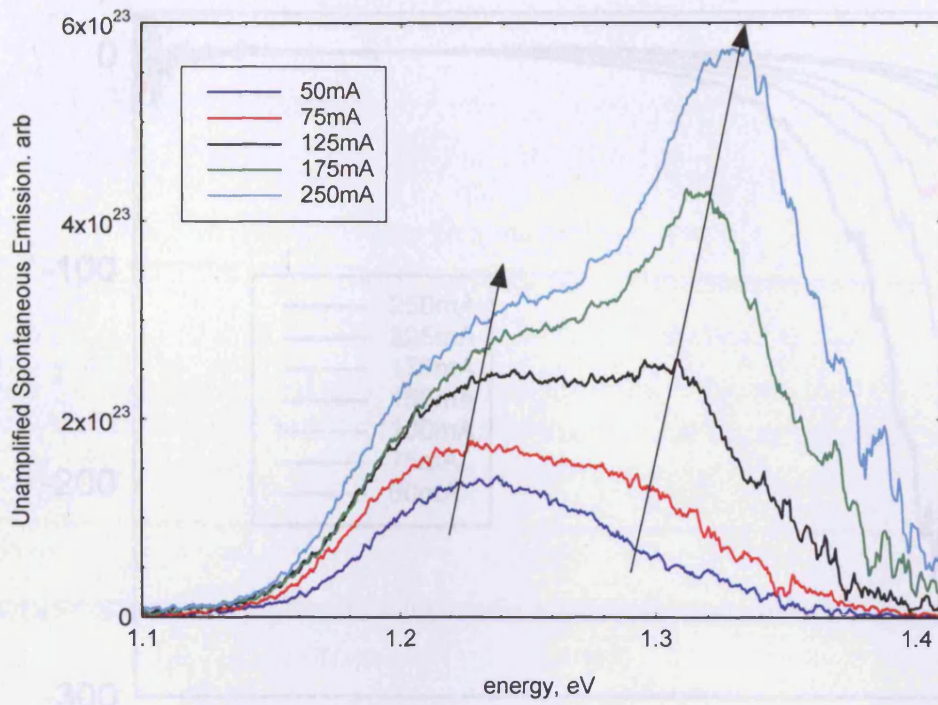


Figure 3.14 Unamplified spontaneous emission spectra for a three-layer quantum dot in bulk GaAs device, measured at 300K

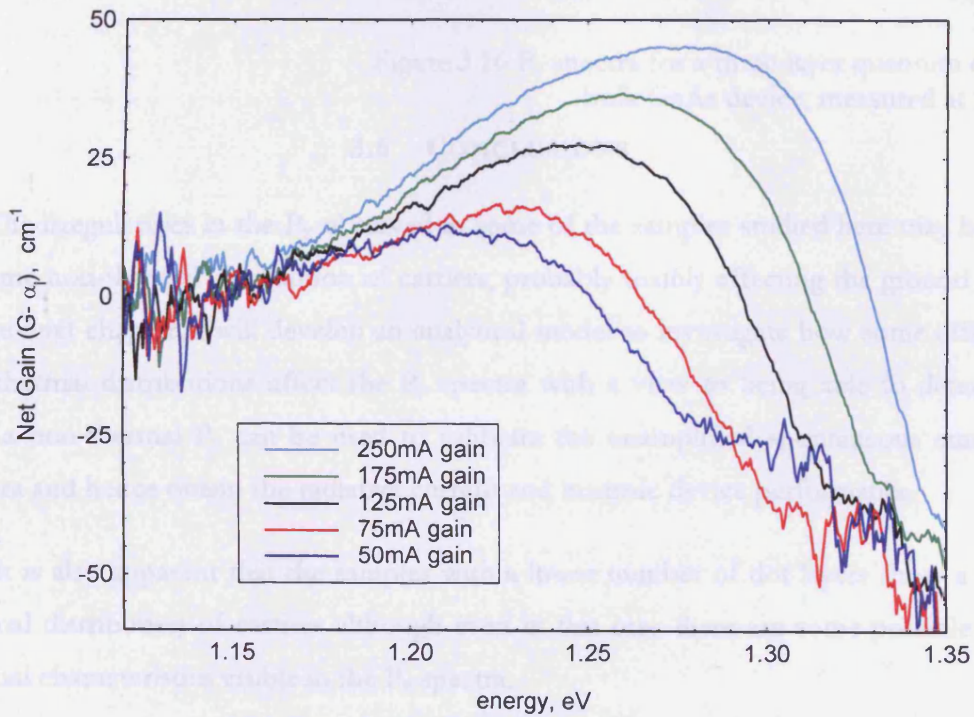


Figure 3.15 Gain spectra for a three-layer quantum dot in bulk GaAs device, measured at 300K

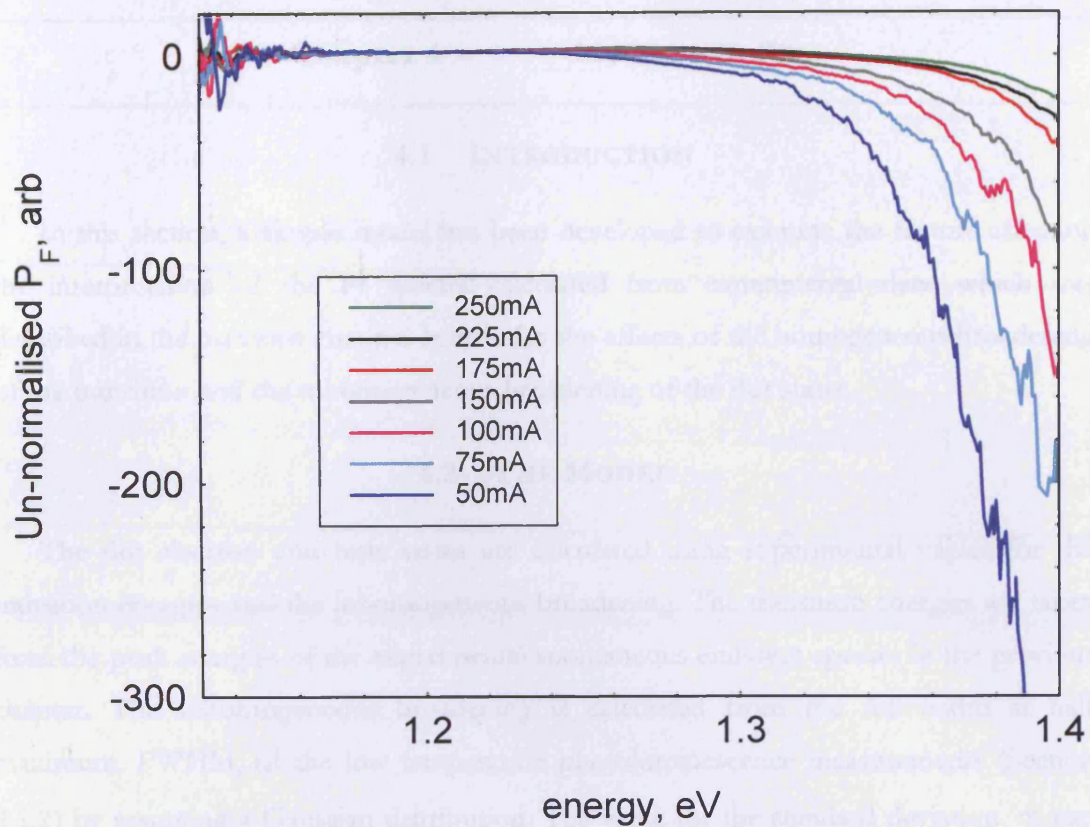


Figure 3.16 P_F spectra for a three-layer quantum dot in bulk GaAs device, measured at 300K

3.6 CONCLUSIONS

The irregularities in the P_F observed in some of the samples studied here may be due to some non-thermal distribution of carriers, probably mainly affecting the ground state. In the next chapter, I will develop an analytical model to investigate how some different non-thermal distributions affect the P_F spectra with a view to being able to determine how a non-thermal P_F can be used to calibrate the unamplified spontaneous emission spectra and hence obtain the radiative current and intrinsic device performance.

It is also apparent that the samples with a lower number of dot layers show a more thermal distribution of carriers although even in this case there are some possible non-thermal characteristics visible in the P_F spectra.

4.1 INTRODUCTION

In this section, a simple model has been developed to examine the factors affecting the interpretation of the Pf spectra calculated from experimental data, which was described in the previous chapter. It includes the effects of the homogeneous broadening of the transition and the inhomogeneous broadening of the dot states.

4.2 THE MODEL

The dot electron and hole states are calculated using experimental values for the transition energies and the inhomogeneous broadening. The transition energies are taken from the peak energies of the experimental spontaneous emission spectra in the previous chapter. The inhomogeneous broadening is calculated from the full width at half maximum, FWHM, of the low temperature photoluminescence measurements (Section 2.1.2) by assuming a Gaussian distribution. The value for the standard deviation, σ , can be found from Equation 4.1.

$$\sigma = \frac{\text{FWHM}}{2\sqrt{(2\ln 2)}} = \frac{\text{FWHM}}{2.35}$$

Equation 4.1

The heavier hole mass produces a Gaussian distribution of states that is much narrower than that of the electron states^[49].

The position, in energy, of the electron and hole states were calculated with reference to the wetting layer where the top of the wetting layer hole states was defined as zero energy. The calculated inhomogeneously broadened density of states can be seen in Figure 4.1 where the blue lines denote the dot ground state and the red lines the dot excited state. Due to the symmetrical nature of our experimental dots in the growth plane (see Section 2.1.2), a degeneracy of two is assumed for the quantum dot excited states from the equivalence of the two in-plane directions.

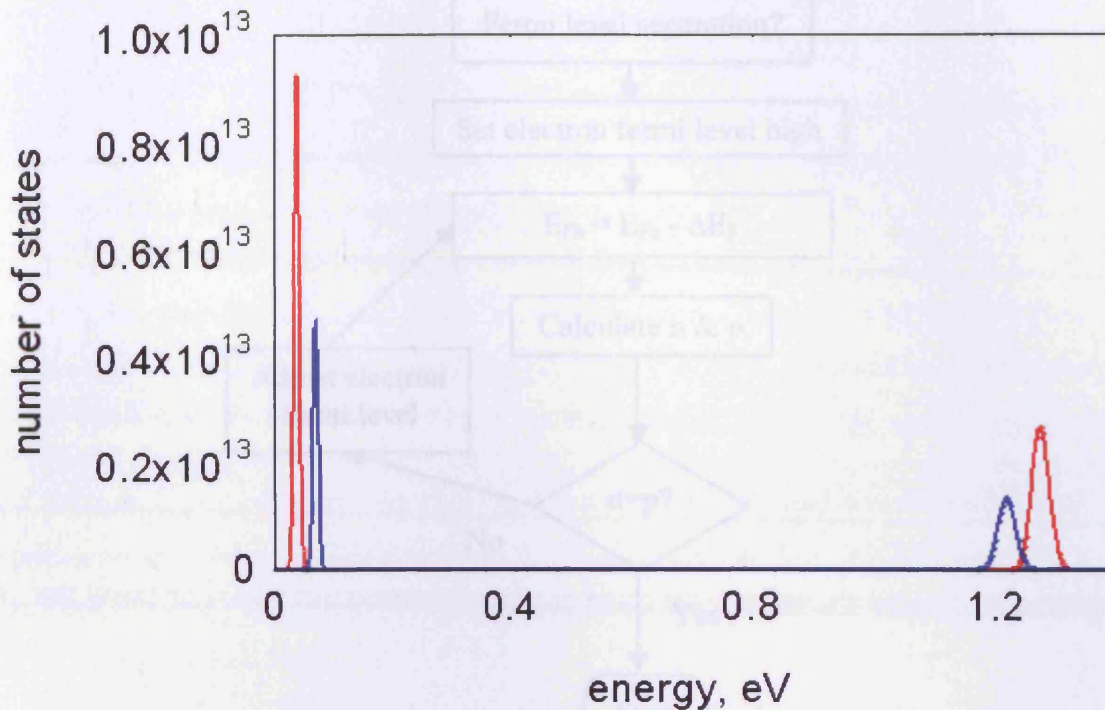


Figure 4.1 Calculated inhomogeneously broadened dot states, where the blue lines denote the dot ground state and the red lines the dot excited state

The positions of the quasi Fermi levels were determined as follows. Using an input quasi-Fermi level separation it is possible to calculate the electron (n) and hole (p) density and iteratively calculate the position of the electron and hole Fermi levels until charge neutrality is satisfied (i.e. until $n=p$). The process used to achieve this is shown in Figure 4.2.

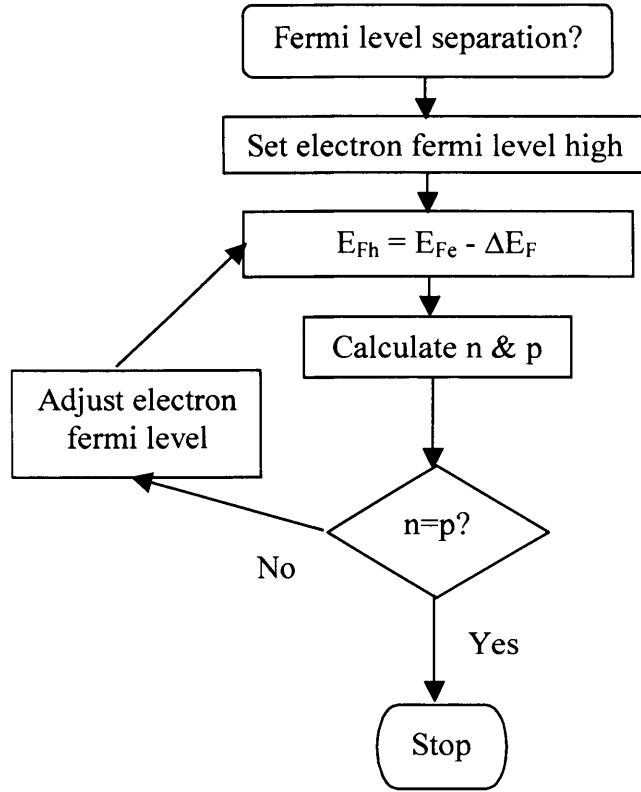


Figure 4.2 Calculation of Quasi-Fermi levels

The values of n and p can be calculated by using Equation 4.2 and the equivalent formula for holes, Equation 4.3^[25].

$$n = \frac{kTm_e^*}{\pi\hbar^2} \sum_{n_x} \ln[1 + e^{(E_{Fe} - E_{n_x})/kT}]$$

Equation 4.2

$$p = \frac{kTm_h^*}{\pi\hbar^2} \sum_{n_x} \ln[1 + e^{(0 - E_{Fh})/kT}]$$

Equation 4.3

These equations are derived by integrating the density of states multiplied by the Fermi function as shown in Equation 4.4 for electrons and the equivalent formula for holes Equation 4.5. $\rho_c(E)$ and $\rho_v(E)$ are the density of states (per unit area per unit energy) in the conduction and valence bands respectively..

$$n = \int \rho_c(E) f(E) dE$$

Equation 4.4

$$p = \int \rho_v(E)[1 - f(E)]dE$$

Equation 4.5

Equation 4.2 and Equation 4.3 are applicable to a two-dimensional quantum well layer and so this approach assumes that the wetting layer states determine the position of the quasi-Fermi levels. This would have been valid as a first approximation due to the relatively low number of states in the zero-dimensional dots compared for the two-dimensional wetting layer^[49], however the program was further refined to include the contribution from the dot states.

The number density of dot states is $15 \times 10^{10} \text{ cm}^{-2}$ calculated using Equation 4.6 and an experimentally determined dot density of $5 \times 10^{10} \text{ cm}^{-2}$ (see Section 2.1.2). This is for a single layer of dots. The density of wetting layer states, for the first sub-band, is $3.01 \times 10^{29} \text{ cm}^{-2} \text{ eV}^{-1}$ given by Equation 4.7.

$$\text{density of dot states} = \text{number density of dots} \times \sum_{\text{states}} (\text{state} \times \text{degeneracy})$$

Equation 4.6

$$DoS_{WL} = \frac{m^*}{\pi \hbar^2}$$

Equation 4.7^[24]

The difference in quasi-Fermi levels obtained with and without the dot states included is indeed small, for example with an input Fermi level separation of 1.2eV the difference is less than 0.01%. Although the correction is small, in the following discussions the Fermi level has been calculated explicitly including the contribution from the dot states.

The quasi-Fermi levels are then used to calculate the probability of occupation of the states for the particular energy pair E_1 and E_2 . The energy pairing is determined by allowing electrons to recombine only with a hole in the same size dot. This has the effect of pairing the higher energy electron states with the lower energy hole states within the same energy level Gaussian distribution (see Figure 4.1). Although in reality the selection rule in quantum dot systems is one of position selection (i.e. recombination only within the same dot) this is a useful approximation to make, as it is closer to reality than allowing free recombination between any electrons and holes.

These occupation probabilities f_1 and f_2 are then input into the general model of Equation 4.8 where the sum over the states refers to the ground and excited state. By comparison with the equations for gain and spontaneous emission derived in Section 1.9 we can see that the numerator determines the gain and the denominator, the spontaneous emission. The gain (absorption) and spontaneous emission are not calculated for the quantum well.

$$P_f(h\nu) = \frac{\sum_{states} \int |M|^2 B(E_i, \sigma) L(h\nu - E_i, \gamma) [f_2(E_i) - f_1(E_i)] dE_i}{\sum_{states} \int |M|^2 B(h\nu, \sigma) L(h\nu - E_i, \gamma) [f_2(E_i) \{1 - f_1(E_i)\}] dE_i}$$

Equation 4.8

Equation 4.9 determines the inhomogeneous broadening (in eV) due to the dispersion of dot sizes and shapes as discussed in Section 1.8.2.

$$B(E, \sigma) = \frac{1}{\sigma\sqrt{2\pi}} \exp\left[-\frac{(E - E_{ensemble})^2}{2\sigma^2}\right]$$

Equation 4.9

Equation 4.10 determines the homogeneous broadening (in eV).

$$S(h\nu - E, \gamma) = \frac{1}{\pi\gamma} \operatorname{sech}\left(\frac{h\nu - E}{\gamma}\right)$$

Equation 4.10

The homogeneous broadening is applied by calculating, for each inhomogeneously broadened energy state, the energy distribution due to the homogeneous broadening. These homogeneously broadened energy distributions are then summed together to give the overall distribution.

Note that the hyperbolic secant function is commonly used in gain calculations to replace the Lorentzian function^[50] that was described in Section 1.8.1 (and repeated in Equation 4.11 below) because a Lorentzian broadening function leads to the unphysical absorption at energies below the band gap as shown in Figure 4.3.

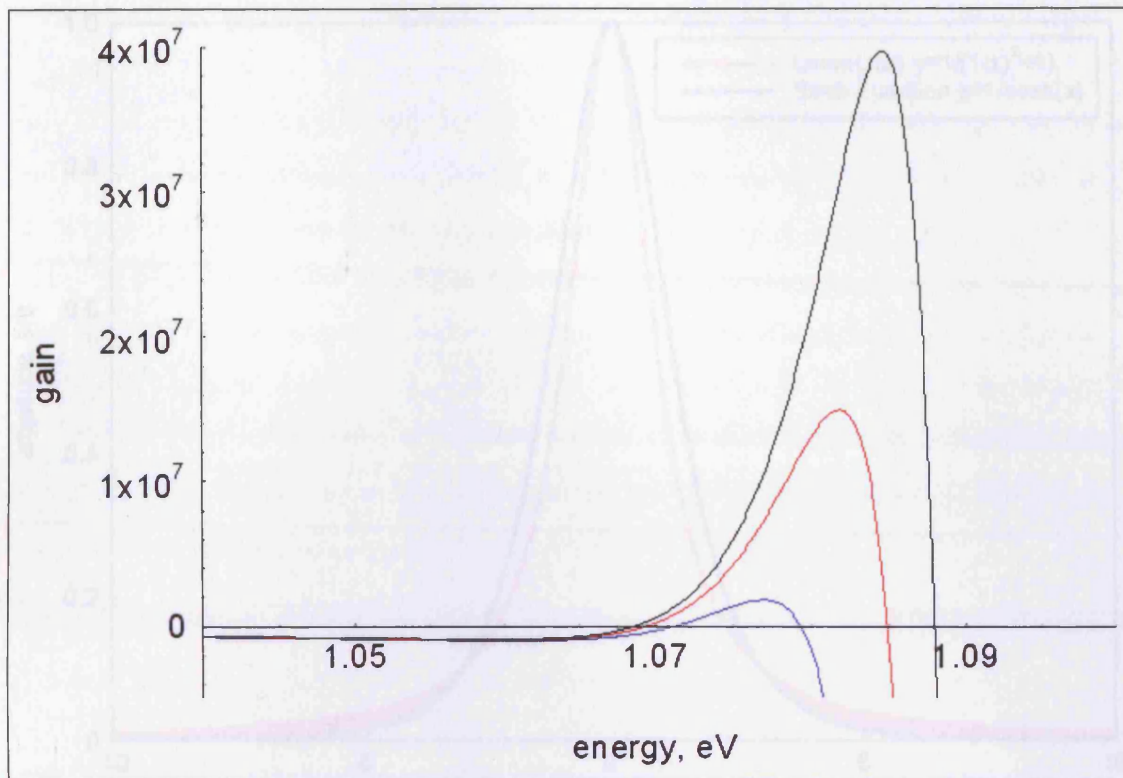


Figure 4.3 Gain calculations using Lorentzian form of homogeneous broadening, showing the unphysical absorption at energies below the band gap

The main difference between the two functions is the differing amounts in the tails, shown in Figure 4.4 as the red shaded area.^[50] The Lorentzian over estimates the effect of the homogeneous broadening due to this slowly decaying tail. The widths of the Sech and Lorentzian functions are denoted as γ and Λ respectively to highlight that these values are not the same, this can be seen in Figure 4.4.

$$L(h\nu - E, \Lambda) = \frac{\Lambda}{\pi \left[(h\nu - E)^2 + \left(\frac{\Lambda}{2} \right)^2 \right]}$$

Equation 4.11

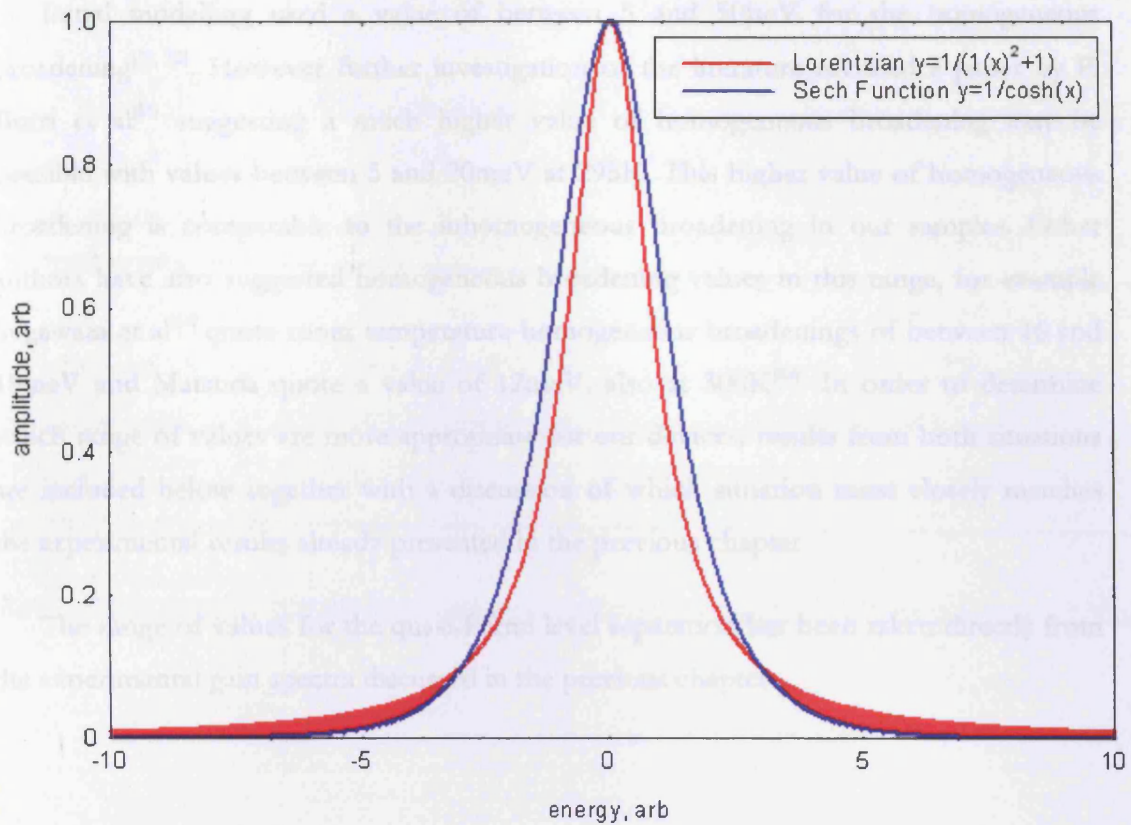


Figure 4.4 Comparison of the Sech and the Lorentzian lineshape functions

4.3 INPUTS

Most of the values used in the calculation are taken from experimental data or literature values of material parameters and these are summarised in Table 4.1 below. The main variables are the inhomogeneous broadening, the homogeneous broadening, and the quasi Fermi level separation.

The inhomogeneous broadening has been varied in the range of $\sigma = 5\text{meV}$ to 50meV with 15meV being the standard value. This value was taken from the experimental values derived from low temperature photoluminescence measurements as detailed in Section 2.1.2.

Initial modelling used a value of between 5 and 50 μeV for the homogeneous broadening^[51, 52]. However further investigation of the literature revealed a paper by P. Borri et al^[53] suggesting a much higher value of homogeneous broadening may be possible with values between 5 and 20meV at 295K. This higher value of homogeneous broadening is comparable to the inhomogeneous broadening in our samples. Other authors have also suggested homogeneous broadening values in this range, for example Sugawara et al^[54] quote room temperature homogeneous broadenings of between 16 and 19meV and Matsuda quote a value of 12meV, also at 300K^[55]. In order to determine which range of values are more appropriate for our devices, results from both situations are included below together with a discussion of which situation most closely matches the experimental results already presented in the previous chapter.

The range of values for the quasi-Fermi level separation has been taken directly from the experimental gain spectra discussed in the previous chapter.

Variable	Range (Standard)	Source
Inhomogeneous broadening, σ	5-50 (15) meV	Low temp PL, Section 2.1.2
Homogeneous broadening, γ	5-50 (20) μ eV 5-25 (15) meV	Sugiyama, Y., et al ^[51] P. Borri et al ^[53]
Quasi-Fermi level separation, ΔE_F	1.1-1.3eV	Gain Spectra, Chapter 3
Ground State Energy	1.15eV	Spontaneous Emission Spectra, Chapter 3
Excited State Energy	1.24eV	Spontaneous Emission Spectra, Chapter 3
Wetting Layer Energy	1.35eV	Spontaneous Emission Spectra, Chapter 3
Dot Density	$5 \times 10^{10} \text{cm}^{-2}$	SEM, Section 2.1.2

Table 4.1 Inputs to the model

4.4 TRUE THERMAL DISTRIBUTION

The initial situation modelled is that of a well-behaved quantum dot system described by a single quasi-Fermi level separation, as this is the simplest to compare to accepted experimental results and theory. The lower range of homogeneous broadening was used and experimental values of inhomogeneous broadening.

Output from the program can be seen in Figure 4.5 showing that the P_F as defined in Section 2.4.5 and calculated from the ratio of the gain and spontaneous emission does fit that derived from Fermi-Dirac statistics, as expected.

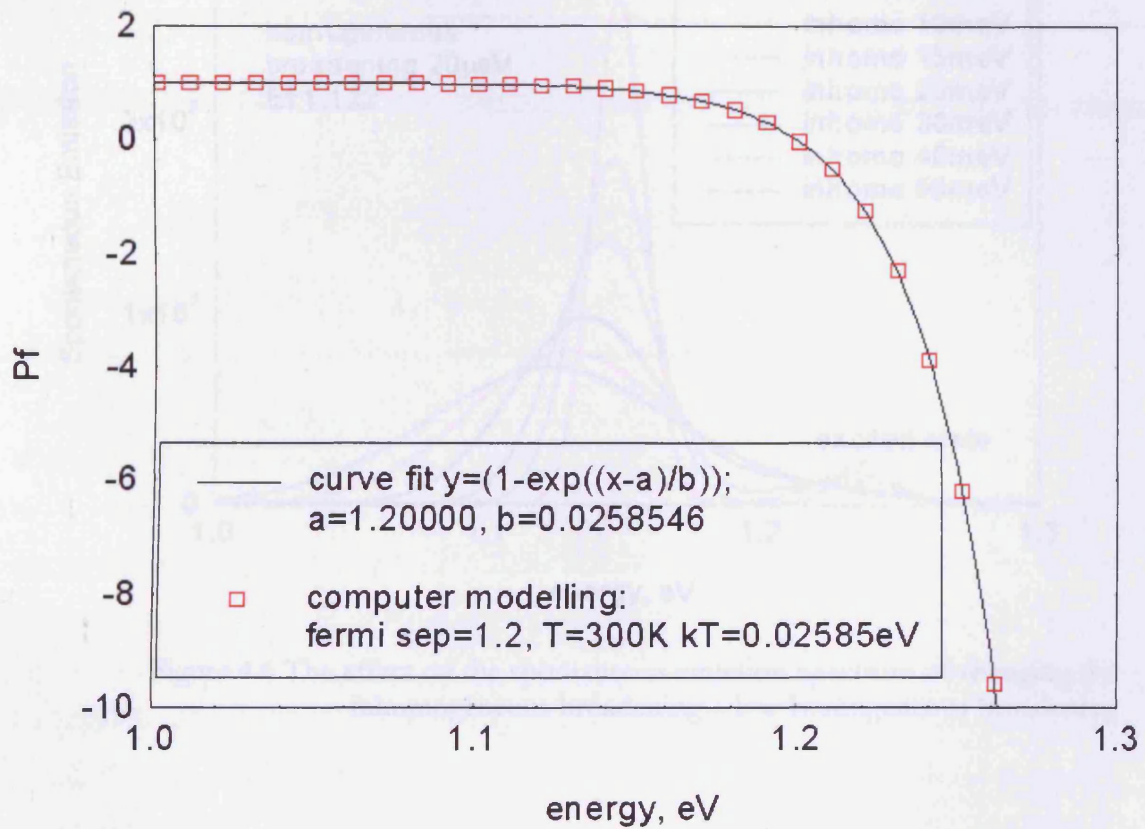


Figure 4.5 Output of Thermal Model Fitted with Equation for a Thermal P_F

Using the lower range of homogeneous broadening, altering the value of the inhomogeneous and the homogeneous broadening has no apparent effect on the modelled P_F shown above in Figure 4.5. This is to be expected as a true thermal P_F can be characterised completely using only the quasi-Fermi level separation and the temperature. Changing the inhomogeneous broadening does however affect the modelled gain and spontaneous emission as shown in Figure 4.6 and Figure 4.7 but these effects cancel in the calculation of the P_F .

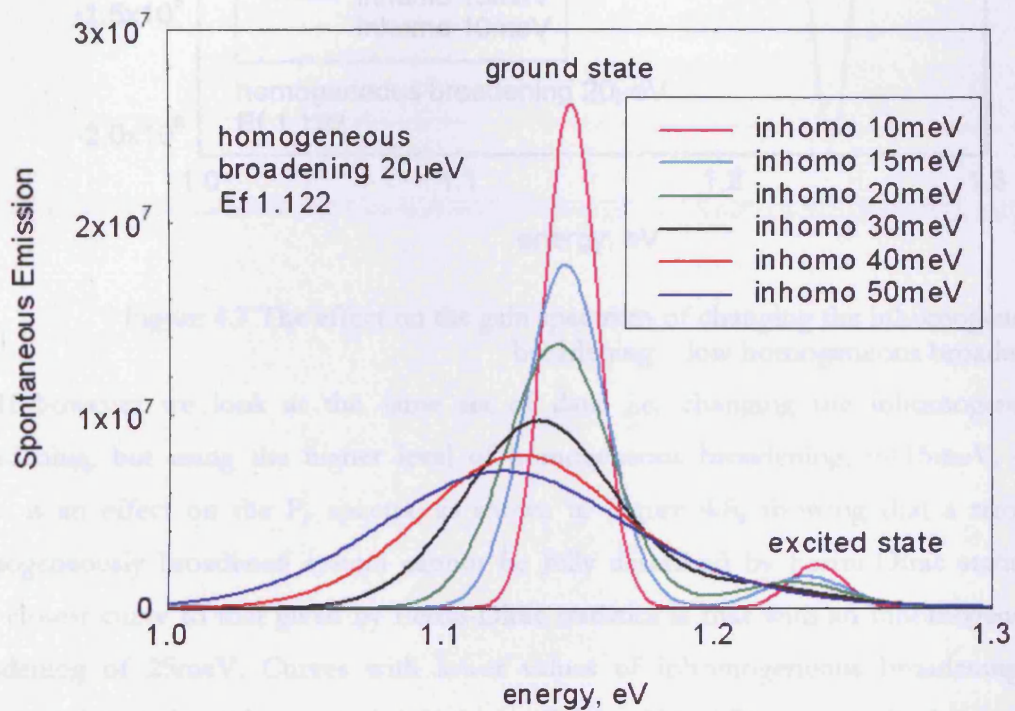


Figure 4.6 The effect on the spontaneous emission spectrum of changing the inhomogeneous broadening – low homogeneous broadening

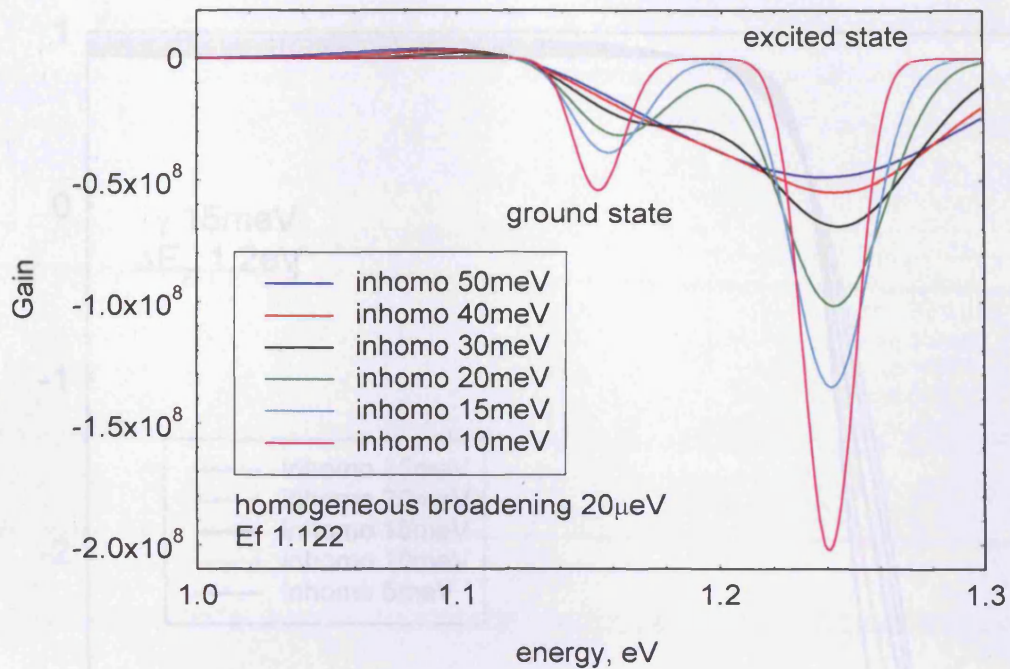


Figure 4.7 The effect on the gain spectrum of changing the inhomogeneous broadening – low homogeneous broadening

If however we look at the same set of data, i.e. changing the inhomogeneous broadening, but using the higher level of homogeneous broadening, $\gamma=15\text{meV}$, then there is an effect on the P_F spectra, as shown in Figure 4.8, showing that a strongly homogeneously broadened system cannot be fully described by Fermi-Dirac statistics. The closest curve to that given by Fermi-Dirac statistics is that with an inhomogeneous broadening of 25meV . Curves with lower values of inhomogeneous broadening no longer tend to unity at low energies as expected from Fermi-Dirac statistics but instead tend to a lower value. The shape of the curves is also altered. This would suggest that where inhomogeneous broadening dominates then Fermi-Dirac statistics can be used to describe the system but where homogeneous broadening dominates this is no longer an accurate description. As inhomogeneous broadening is reduced in experimental devices due to improvements in growth techniques, then this will become increasingly important.

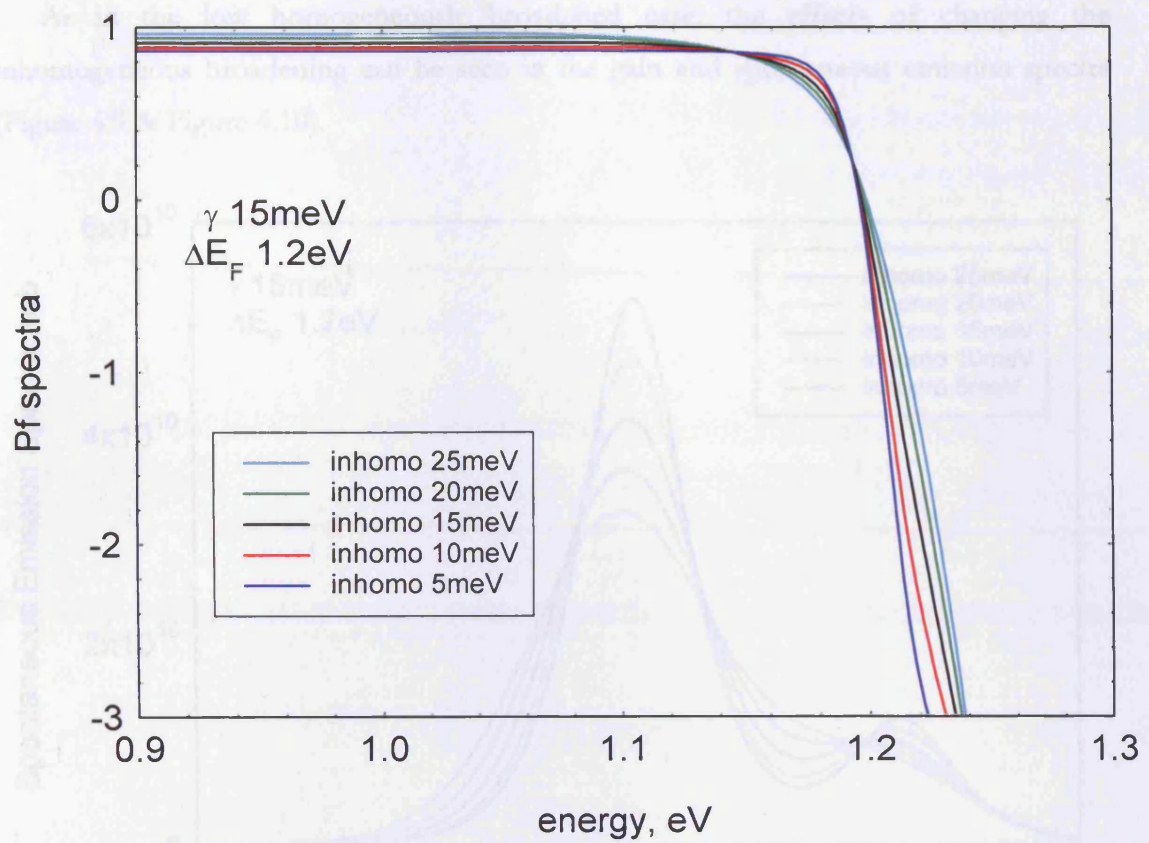


Figure 4.8 P_f spectra with varying inhomogeneous broadening levels for the high homogeneous broadening case.

Figure 4.9 The effect on the spontaneous emission spectrum of changing the inhomogeneous broadening - large homogeneous versus broadening. It can be seen in Figure 4.9 that as the inhomogeneous broadening is increased, the spontaneous emission peak broadens and reduces in intensity. For the largest levels of inhomogeneous broadening, it is difficult to distinguish the ground and excited states. The standard deviation characterizing the inhomogeneous broadening that was obtained from our experimental device by low temperature PL spectra scans, varied between 14 and 21meV depending on the structure. For the 10 meV peak width curves of 15 and 20meV in figure 4.9 it can be seen that the ground and excited states are distinguishable, as was observed in the experimental results presented in the previous chapter.

As in the low homogeneously broadened case, the effects of changing the inhomogeneous broadening can be seen in the gain and spontaneous emission spectra (Figure 4.9 & Figure 4.10).

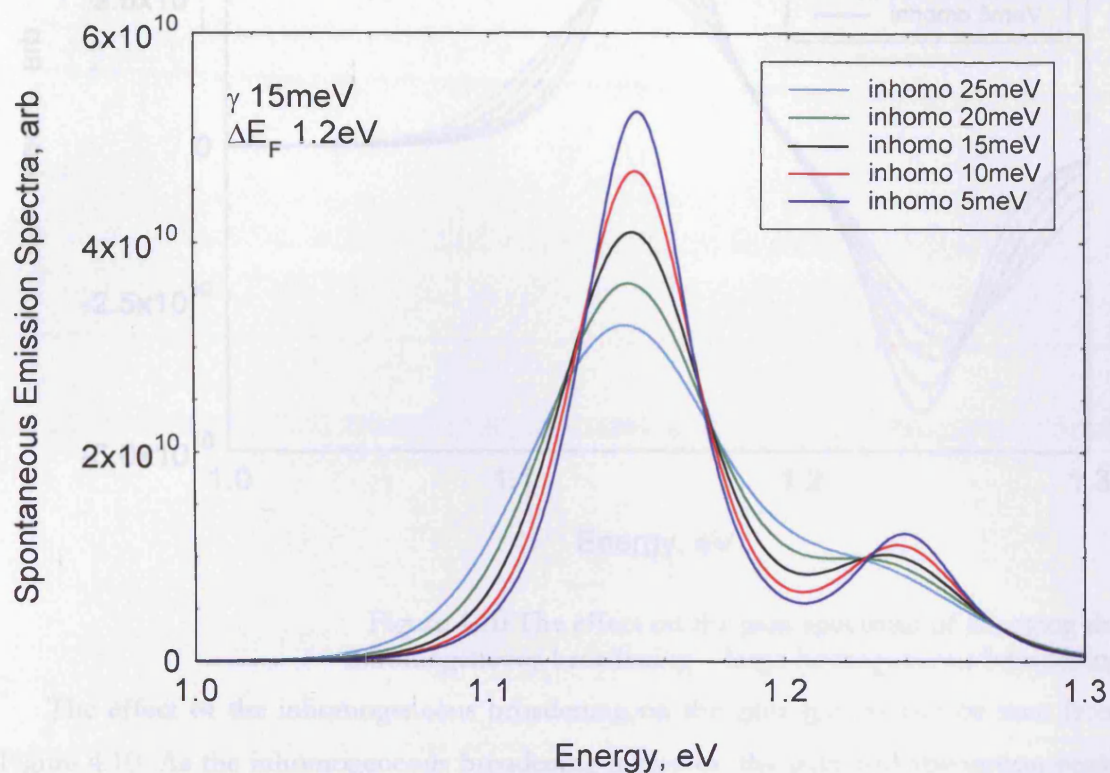


Figure 4.9 The effect on the spontaneous emission spectrum of changing the inhomogeneous broadening – large homogeneous broadening

It can be seen in Figure 4.9 that as the inhomogeneous broadening is increased, the spontaneous emission peaks broaden and reduce in intensity. For the largest levels of inhomogeneous broadening, it is difficult to distinguish the ground and excited states. The standard deviation characterising the inhomogeneous broadening that was obtained from our experimental devices by low temperature PL measurements, varied between 14 and 21meV depending on the structure. For the corresponding curves of 15 and 20meV in Figure 4.9 it can be seen that the ground and excited states are distinguishable, as was observed in the experimental results presented in the previous chapter.

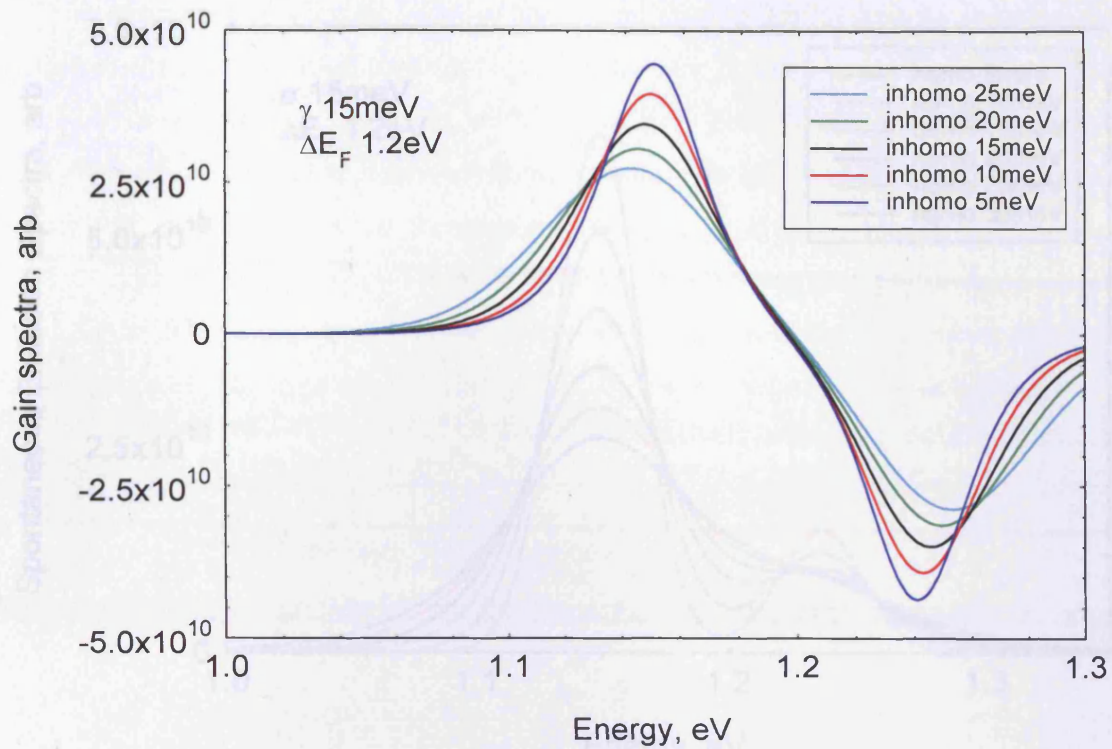


Figure 4.10 The effect on the gain spectrum of changing the inhomogeneous broadening – large homogeneous broadening

The effect of the inhomogeneous broadening on the gain spectra can be seen from Figure 4.10. As the inhomogeneous broadening increases, the gain and absorption peaks consequently broaden and reduce in intensity.

Changing the value of the homogeneous broadening has a similar effect on the gain and spontaneous emission to that of the inhomogeneous broadening. This can be seen in Figure 4.11 and Figure 4.12 for the higher range of homogeneous broadening. With an inhomogeneous broadening value of 15meV, the curve in Figure 4.11 closest in form to the experimental curves in Chapter 3 is that where the homogeneous broadening is between 10 and 15meV. This would suggest that the homogeneous broadening in our samples is comparable to the inhomogeneous broadening.



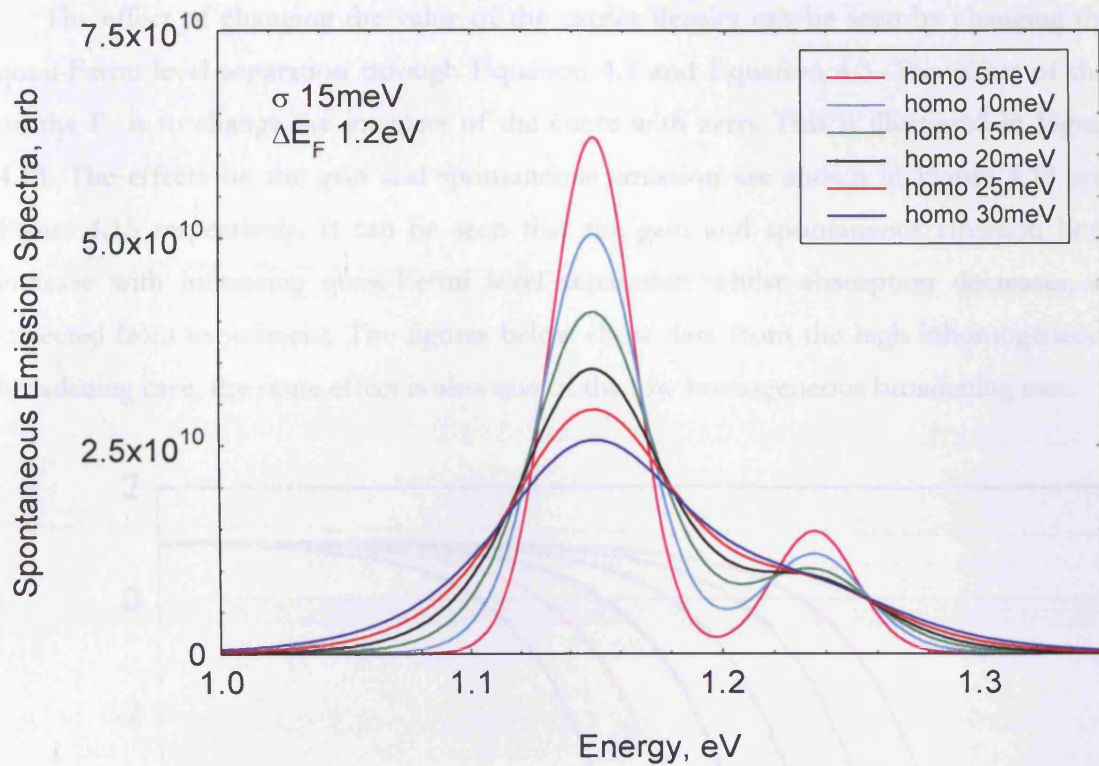


Figure 4.11 Spontaneous emission – inhomogeneous broadening 15meV, varying homogeneous broadening

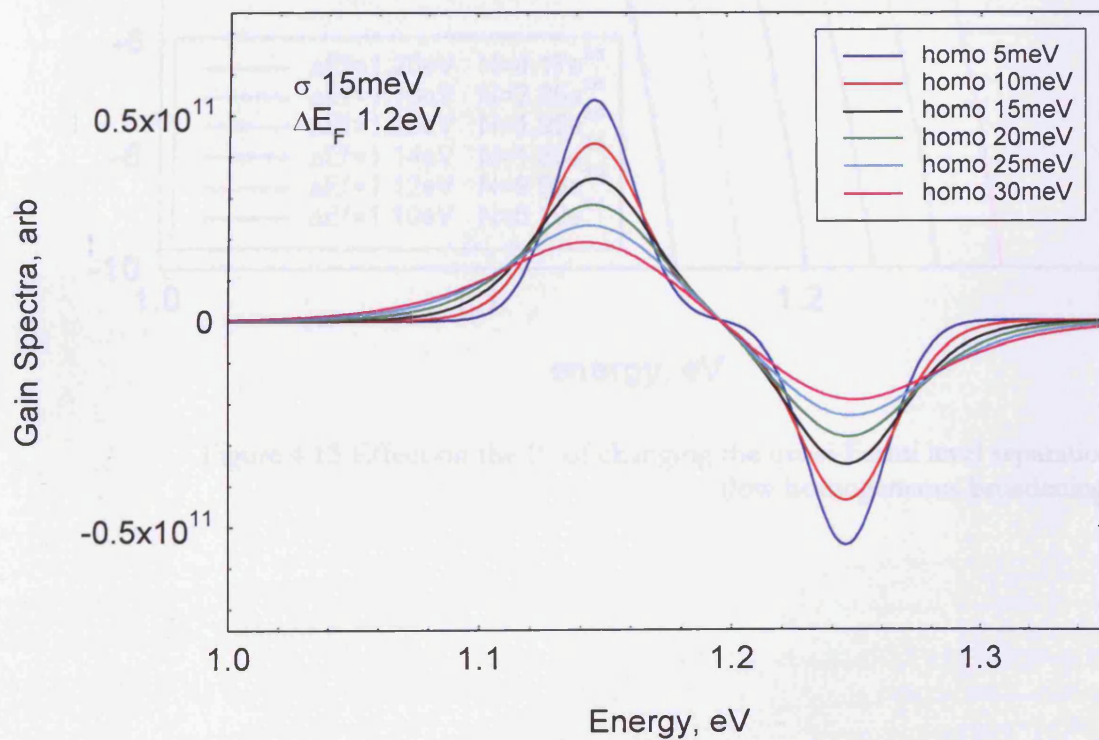


Figure 4.12 Gain spectra – inhomogeneous broadening 15meV, varying homogeneous broadening

The effect of changing the value of the carrier density can be seen by changing the quasi-Fermi level separation through Equation 4.2 and Equation 4.3. The effect of this on the P_F is to change the intersect of the curve with zero. This is illustrated in Figure 4.13. The effects on the gain and spontaneous emission are shown in Figure 4.14 and Figure 4.15 respectively. It can be seen that the gain and spontaneous emission both increase with increasing quasi-Fermi level separation whilst absorption decreases, as expected from experiment. The figures below show data from the high inhomogeneous broadening case, the same effect is also true of the low homogeneous broadening case.

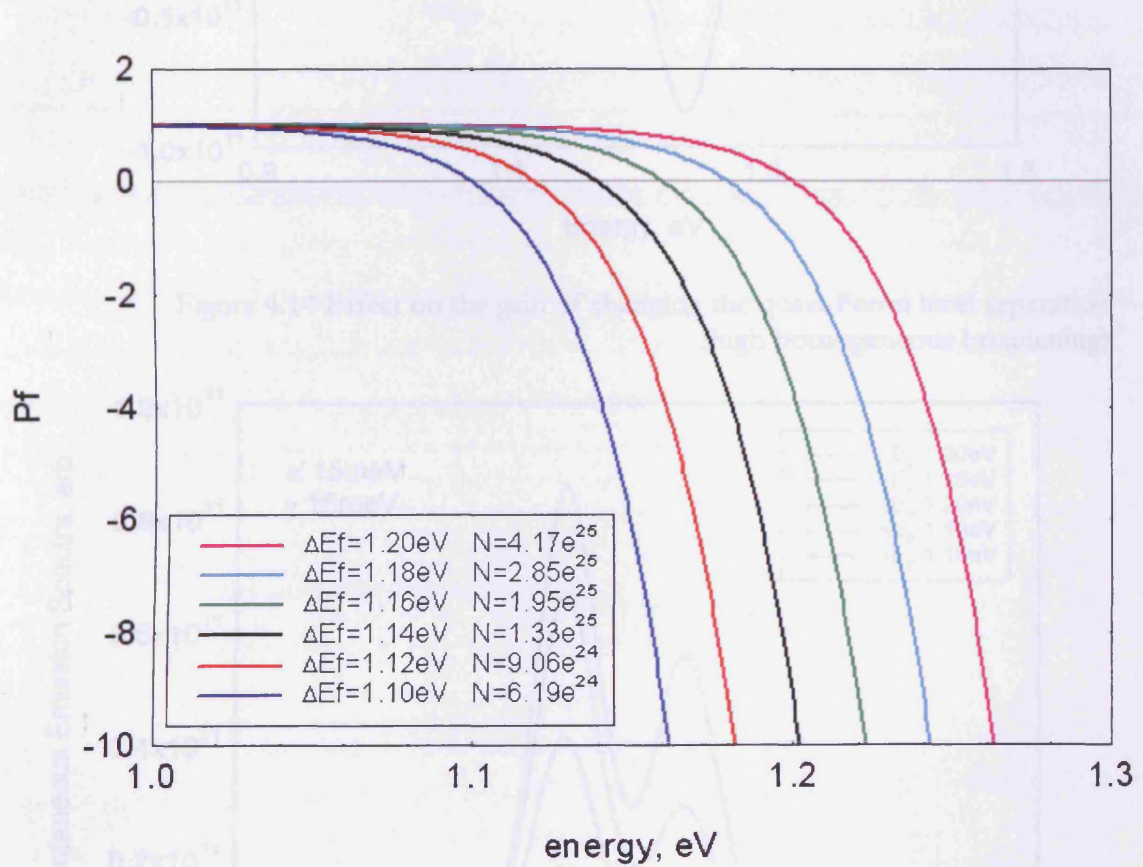


Figure 4.13 Effect on the P_F of changing the quasi-Fermi level separation (low homogeneous broadening)

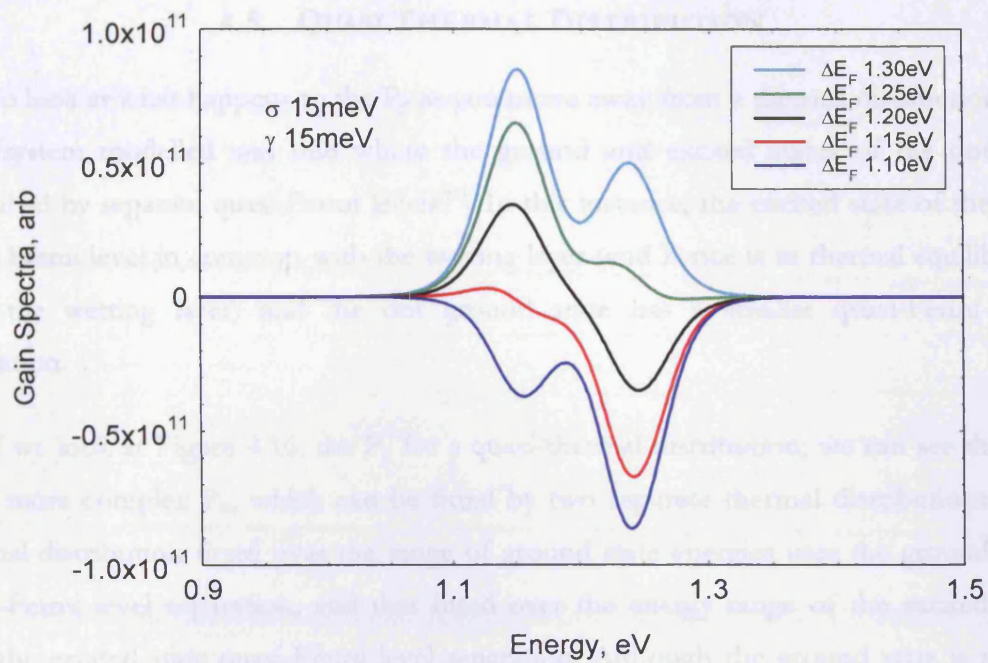


Figure 4.14 Effect on the gain of changing the quasi-Fermi level separation (high homogeneous broadening)

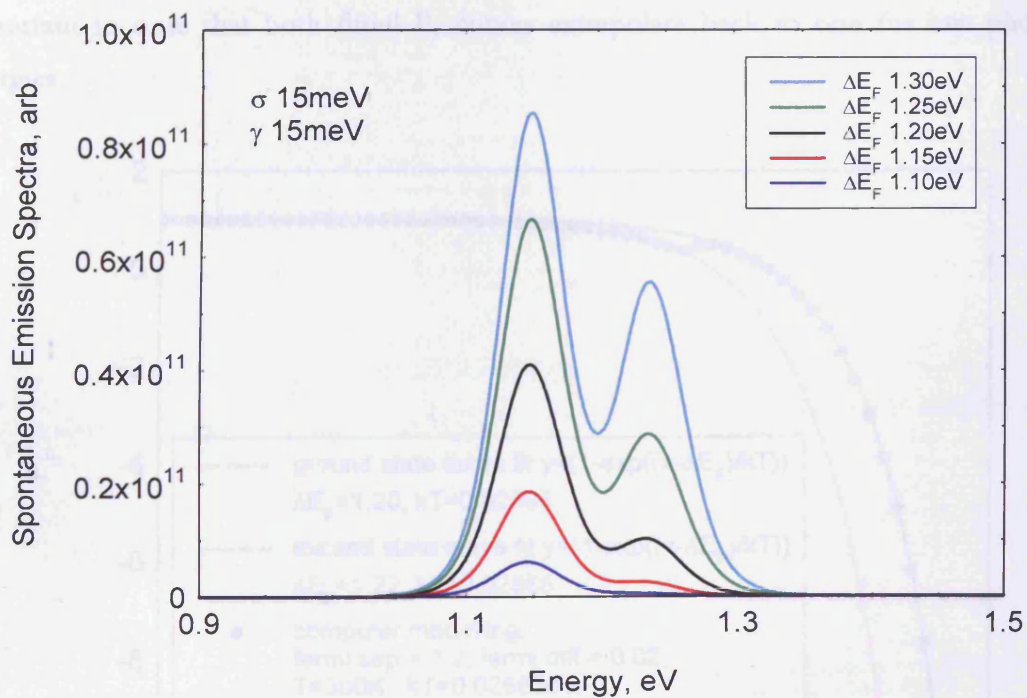


Figure 4.15 Effect on the spontaneous emission of changing the quasi-Fermi level separation (high homogeneous broadening)

4.5 QUASI THERMAL DISTRIBUTION

To look at what happens to the P_F as you move away from a thermal distribution, the next system modelled was one where the ground and excited states of the dots are described by separate quasi-Fermi levels^[56]. In this instance, the excited state of the dots has a Fermi level in common with the wetting layer (and hence is in thermal equilibrium with the wetting layer) and the dot ground state has a smaller quasi-Fermi level separation.

If we look at Figure 4.16, the P_F for a quasi-thermal distribution, we can see that we get a more complex P_F , which can be fitted by two separate thermal distributions. The thermal distribution fitted over the range of ground state energies uses the ground state quasi-Fermi level separation, and that fitted over the energy range of the excited state uses the excited state quasi-Fermi level separation. Although the ground state is not in thermal equilibrium with the excited state, as this would need a global quasi-Fermi level separation, the carriers within it are distributed according to Fermi-Dirac statistics. It is important to note that both fitted P_F curves extrapolate back to one for low photon energies.

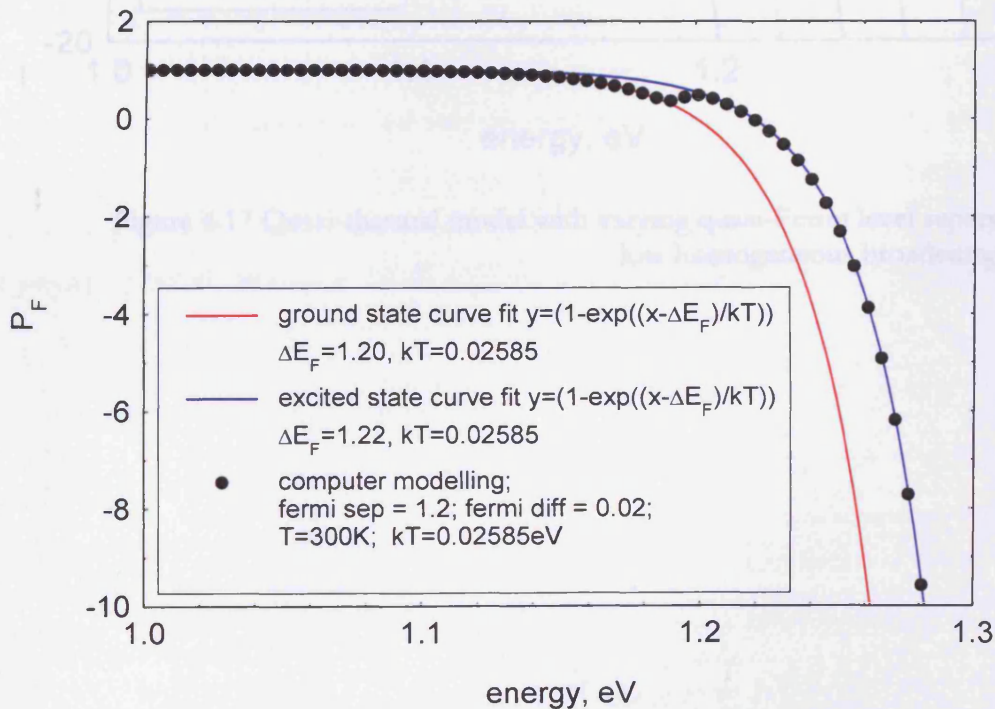


Figure 4.16 Output of quasi-thermal model fitted with equations for thermal P_F , low homogeneous broadening case

As the difference in the quasi-Fermi level separations is increased, it becomes possible to have Pf spectra that cross zero twice, once for the ground state and again for the excited state. This is shown in Figure 4.17 below. Similar results are obtained for the high homogeneous broadening case as shown in Figure 4.18.

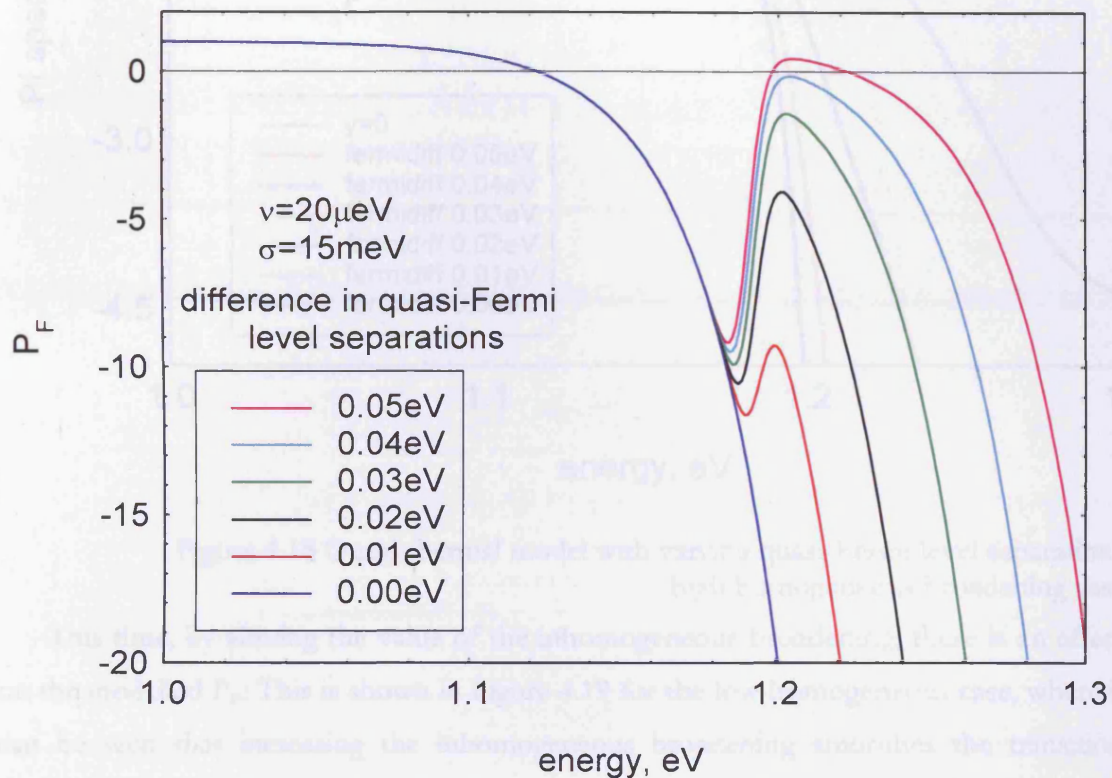


Figure 4.17 Quasi-thermal model with varying quasi-Fermi level separations low homogeneous broadening case

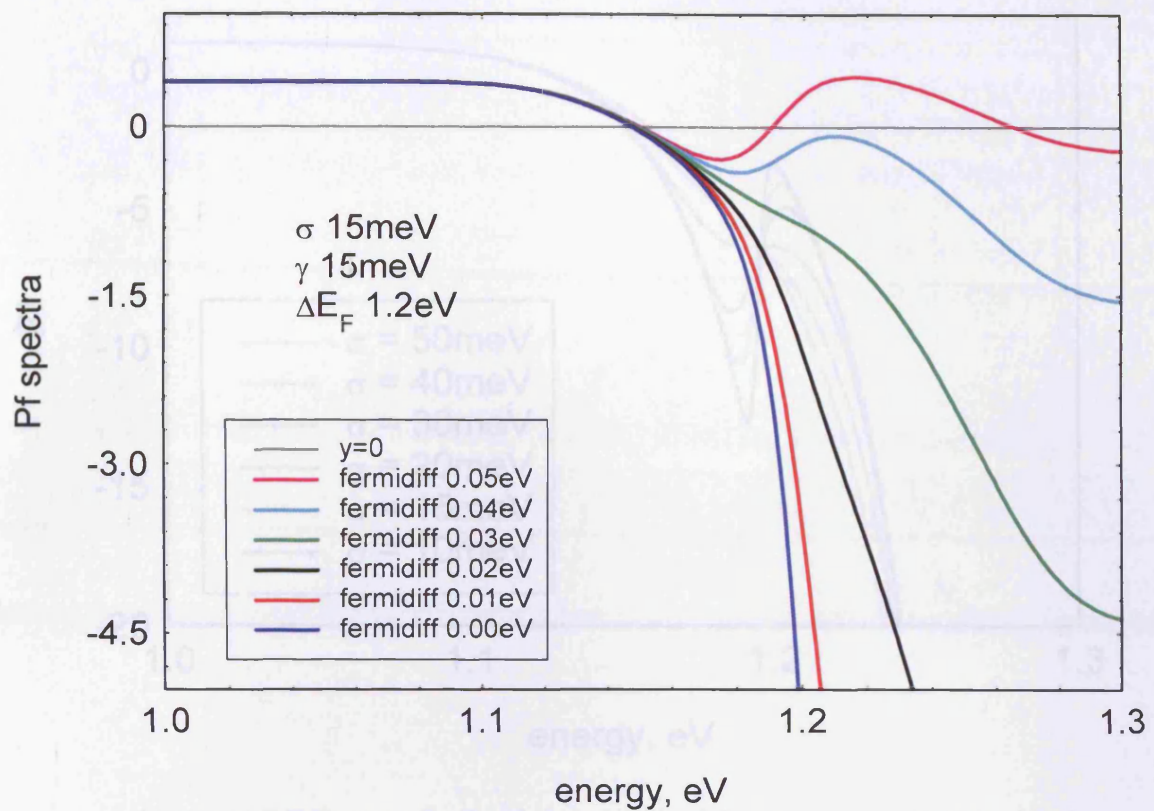


Figure 4.18 Quasi-thermal model with varying quasi-Fermi level separations high homogeneous broadening case

This time, by altering the value of the inhomogeneous broadening, there is an effect on the modelled P_f . This is shown in Figure 4.19 for the low homogeneous case, where it can be seen that increasing the inhomogeneous broadening smooths the transition between the ground and excited state, as might be expected. Changing the inhomogeneous broadening affects the modelled gain and spontaneous emission in the same way as for the thermal case. The results are shown in Figure 4.20 and Figure 4.21.

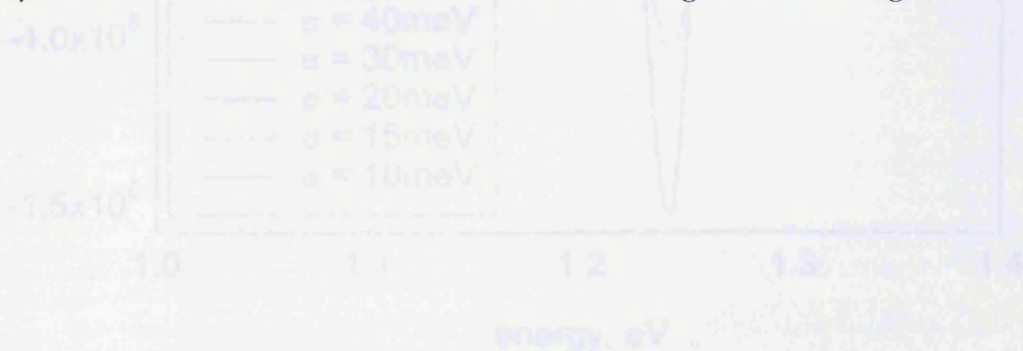


Figure 4.20 Effect on the gain of changing the inhomogeneous broadening for a homogeneous σ of a laser of 20meV

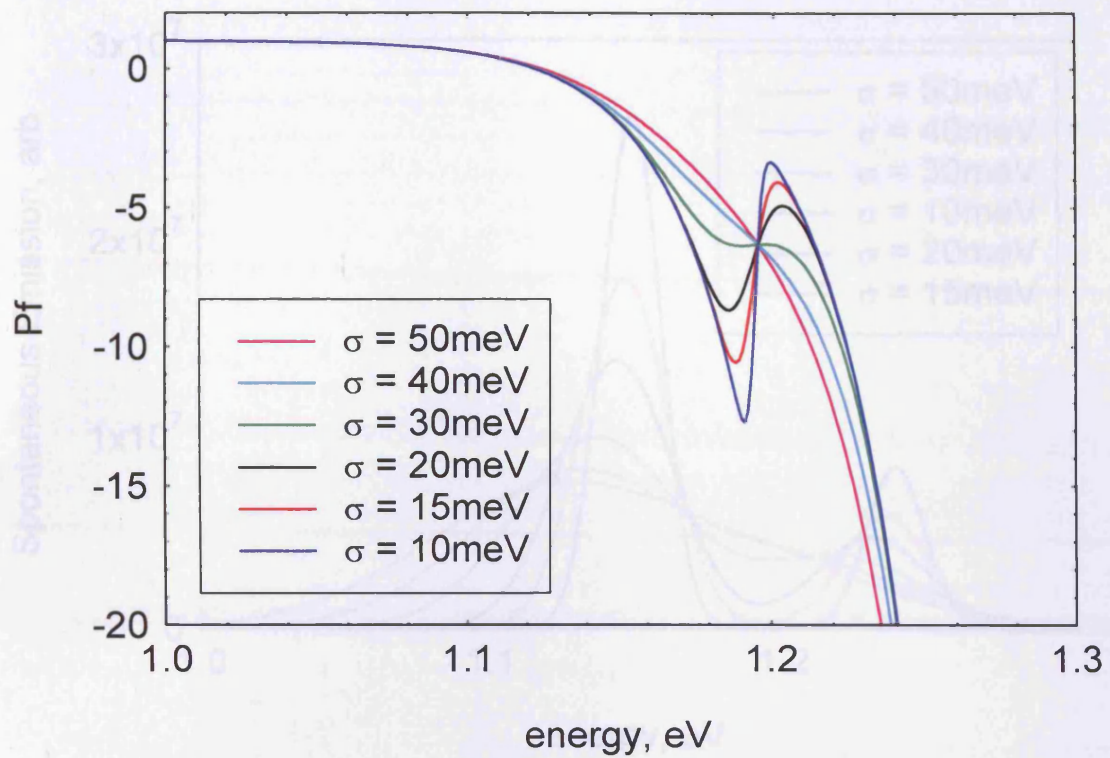


Figure 4.19 Effect on the P_F of changing the inhomogeneous broadening for a homogeneous broadening of $20 \mu\text{eV}$

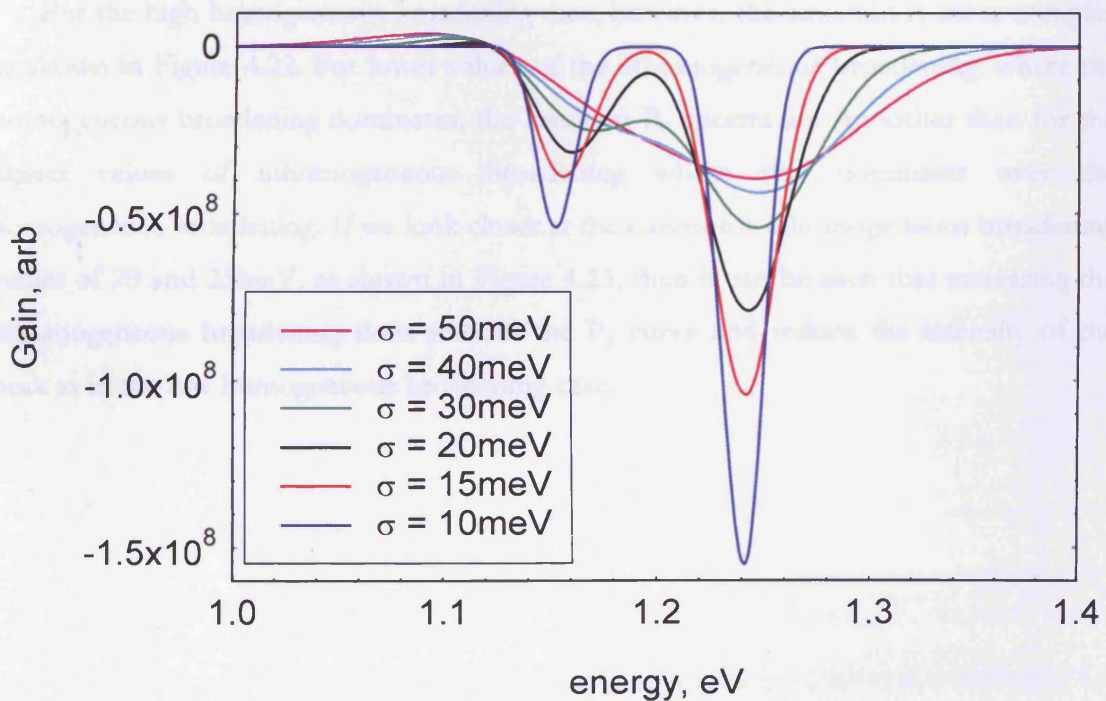


Figure 4.20 Effect on the gain of changing the inhomogeneous broadening for a homogeneous broadening of $20 \mu\text{eV}$

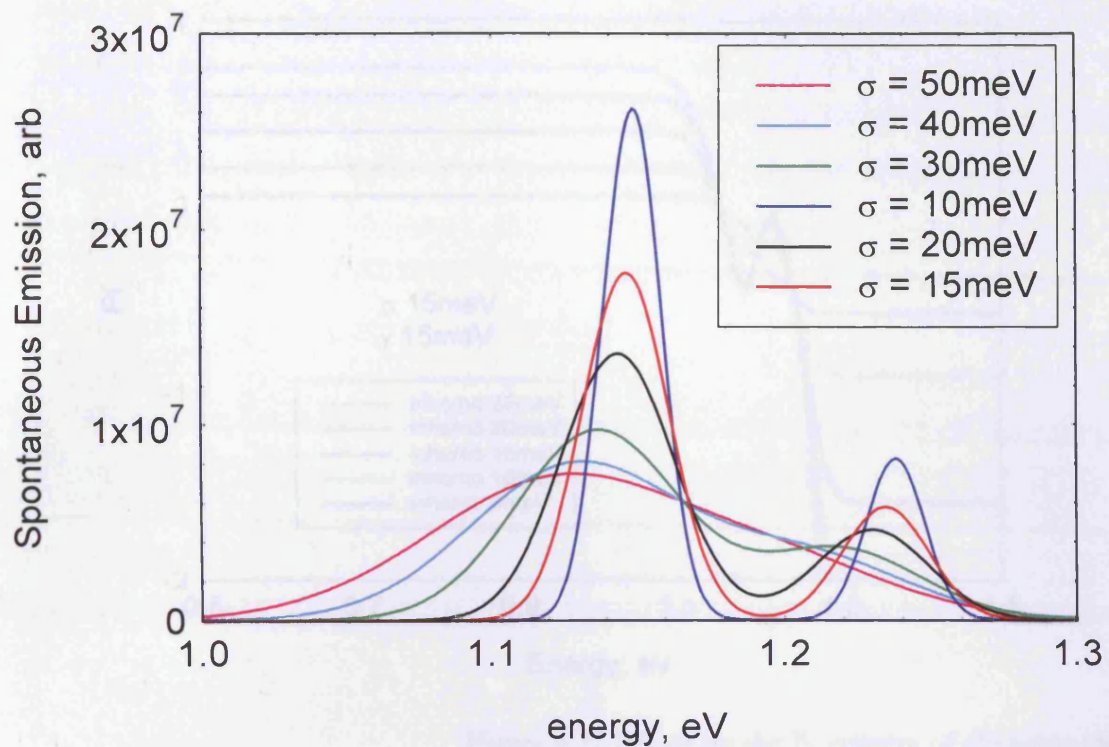


Figure 4.21 Effect on the spontaneous emission of changing the inhomogeneous broadening, low homogeneous broadening

For the high homogeneous broadening case, however, the situation is more complex as shown in Figure 4.22. For lower values of the inhomogeneous broadening, where the homogeneous broadening dominates, the resultant P_F spectra are smoother than for the higher values of inhomogeneous broadening where this dominates over the homogeneous broadening. If we look closer at the curves for inhomogeneous broadening values of 20 and 25meV, as shown in Figure 4.23, then it can be seen that increasing the inhomogeneous broadening does smooth the P_F curve and reduce the intensity of the peak as in the low homogeneous broadening case.

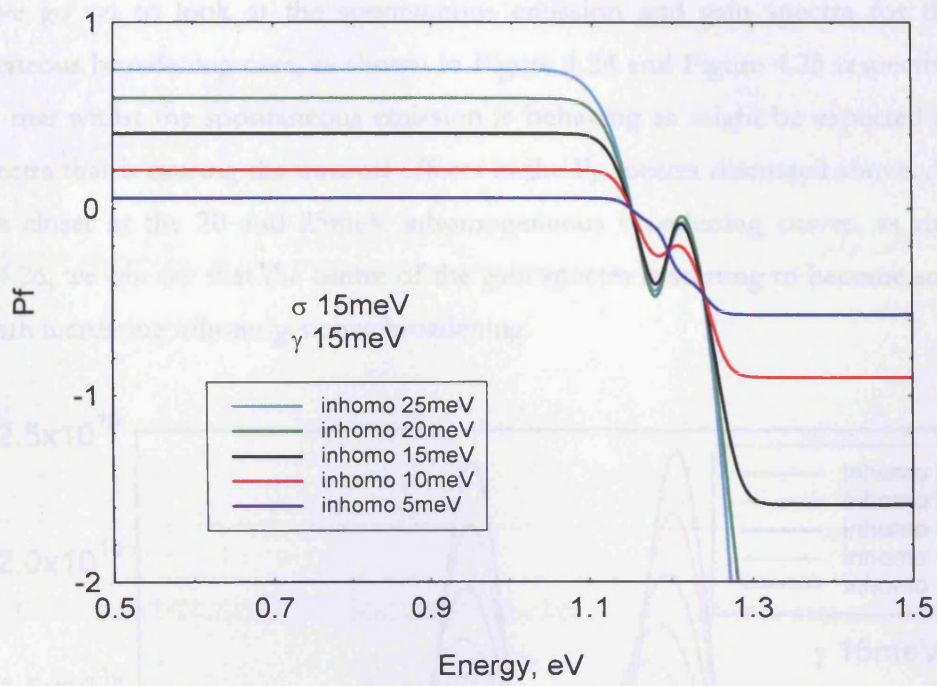


Figure 4.22 Effect on the P_F spectra of changing the inhomogeneous broadening, high homogeneous broadening

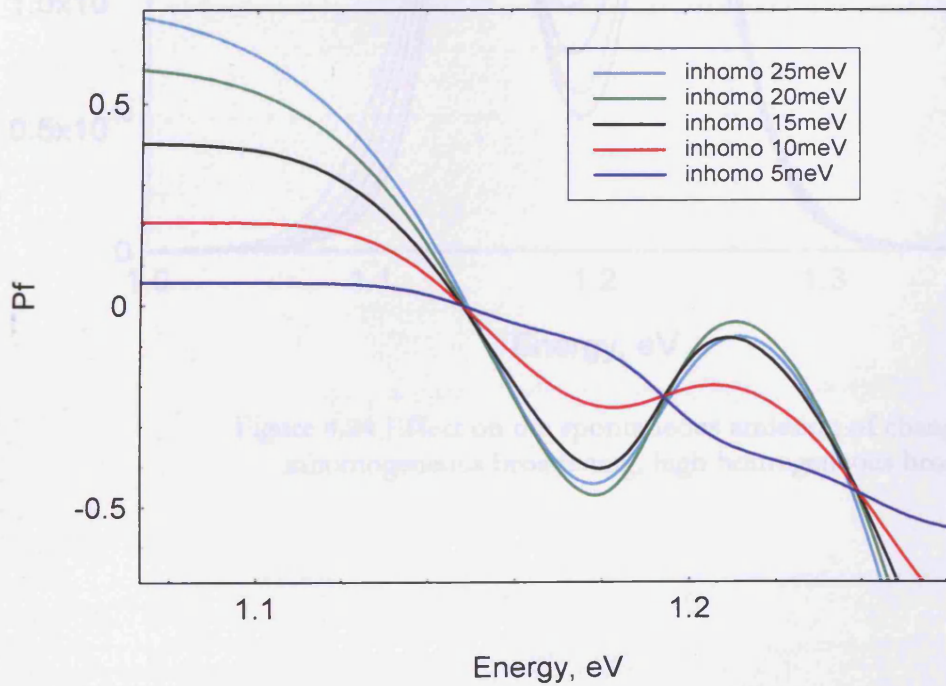


Figure 4.23 Enlargement of Figure 4.22, effect on the P_F spectra of changing the inhomogeneous broadening, high homogeneous broadening

If we go on to look at the spontaneous emission and gain spectra for the high homogeneous broadening case, as shown in Figure 4.24 and Figure 4.25 respectively, we can see that whilst the spontaneous emission is behaving as might be expected it is the gain spectra that is causing the unusual effects in the P_F spectra discussed above. Again, if we look closer at the 20 and 25meV inhomogeneous broadening curves, as shown in Figure 4.26, we can see that the centre of the gain spectra is starting to become smoother again with increasing inhomogeneous broadening.

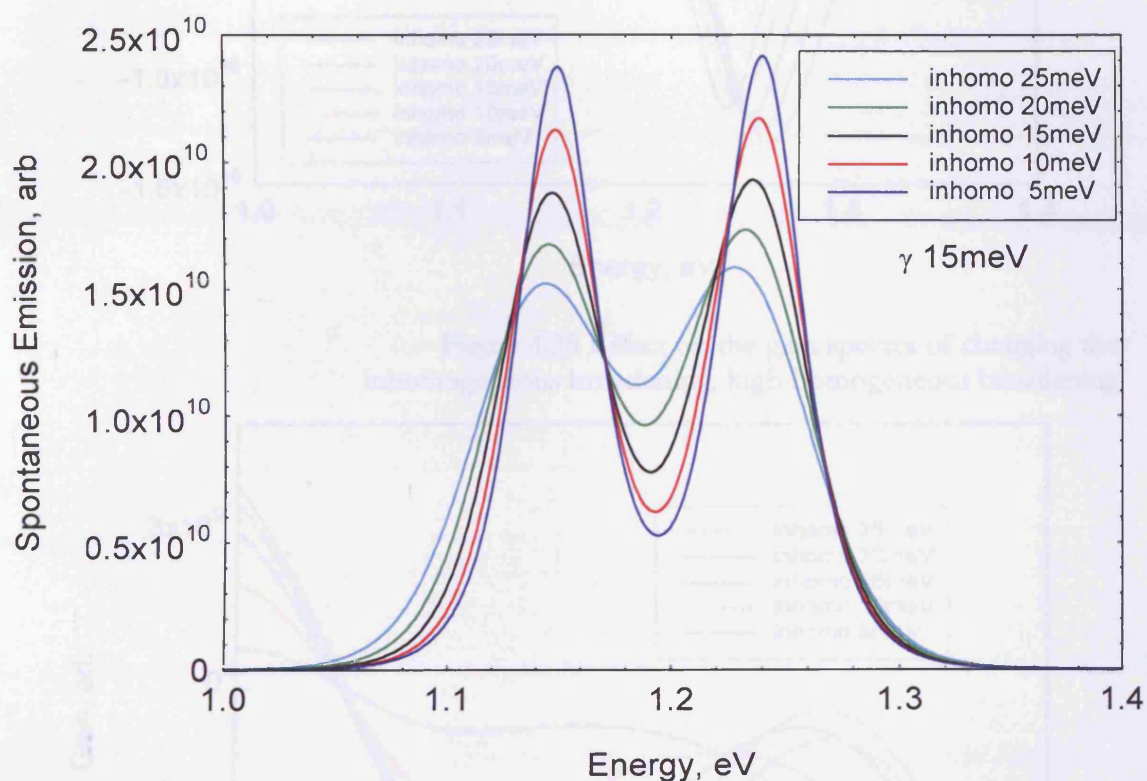


Figure 4.24 Effect on the spontaneous emission of changing the inhomogeneous broadening, high homogeneous broadening

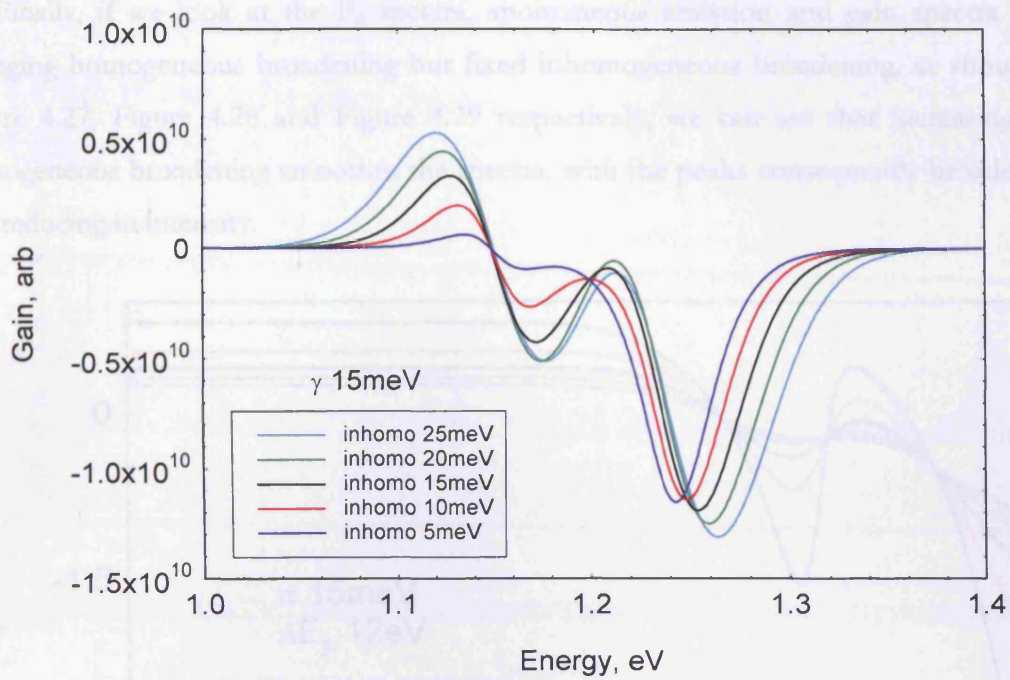


Figure 4.25 Effect on the gain spectra of changing the inhomogeneous broadening, high homogeneous broadening

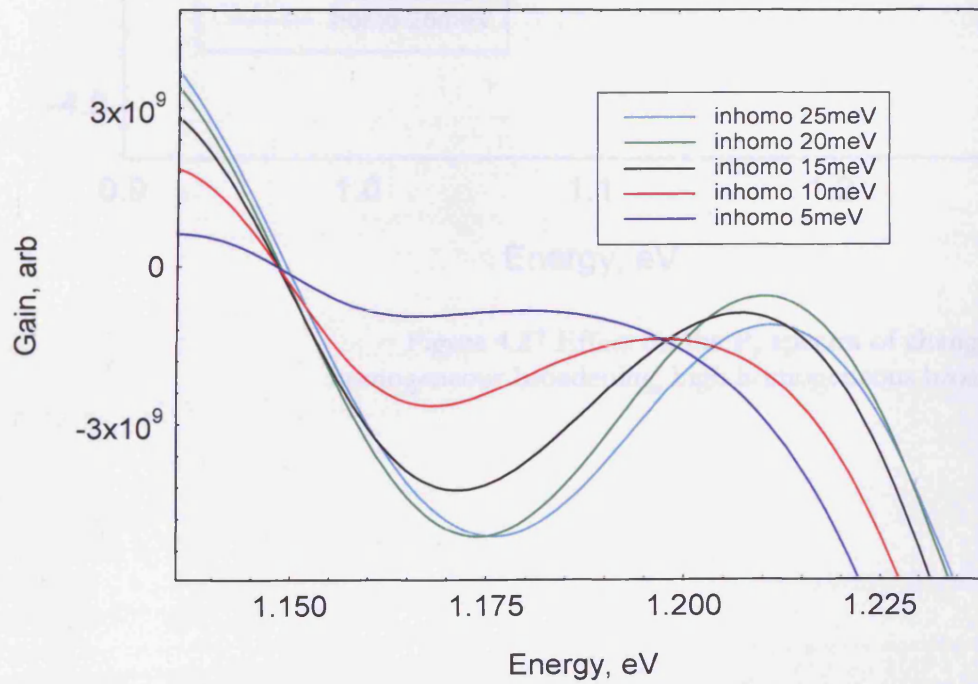


Figure 4.26 Enlargement of Figure 4.25, effect on the gain spectra of changing the inhomogeneous broadening, high homogeneous broadening

Finally, if we look at the P_F spectra, spontaneous emission and gain spectra with changing homogeneous broadening but fixed inhomogeneous broadening, as shown in Figure 4.27, Figure 4.28 and Figure 4.29 respectively, we can see that increasing the homogeneous broadening smooths the spectra, with the peaks consequently broadening and reducing in intensity.

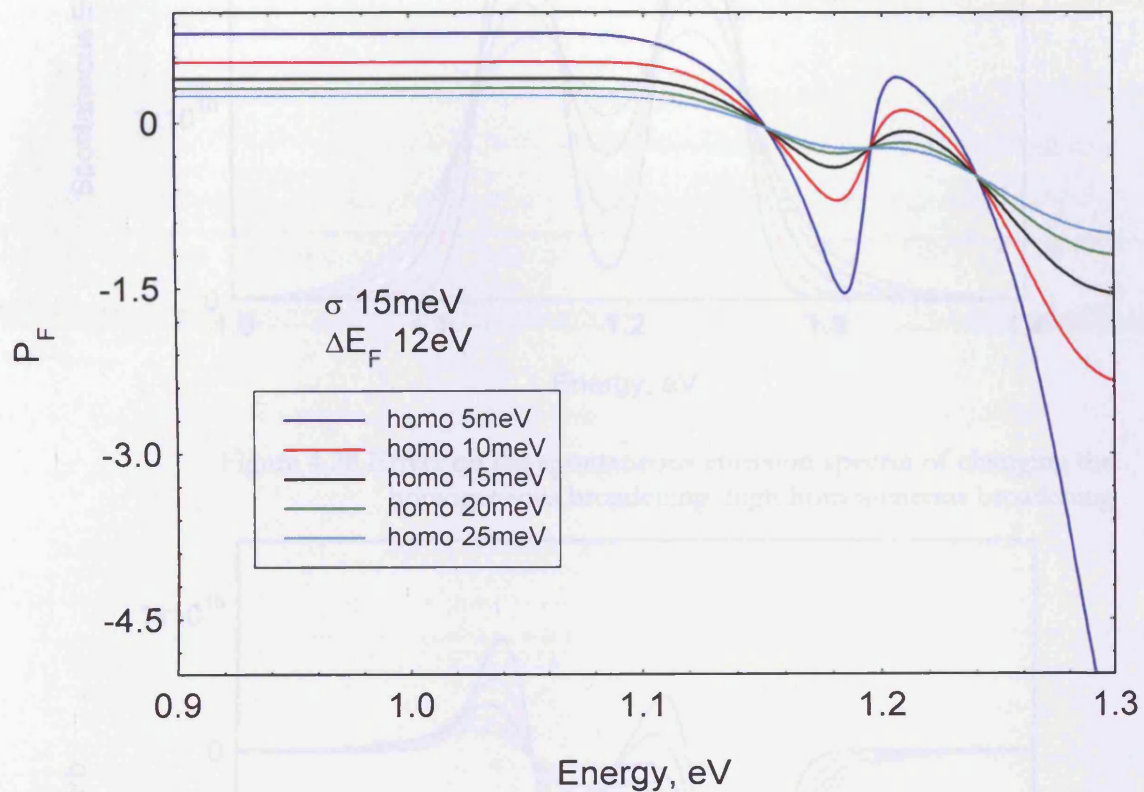


Figure 4.27 Effect on the P_F spectra of changing the homogeneous broadening, high homogeneous broadening

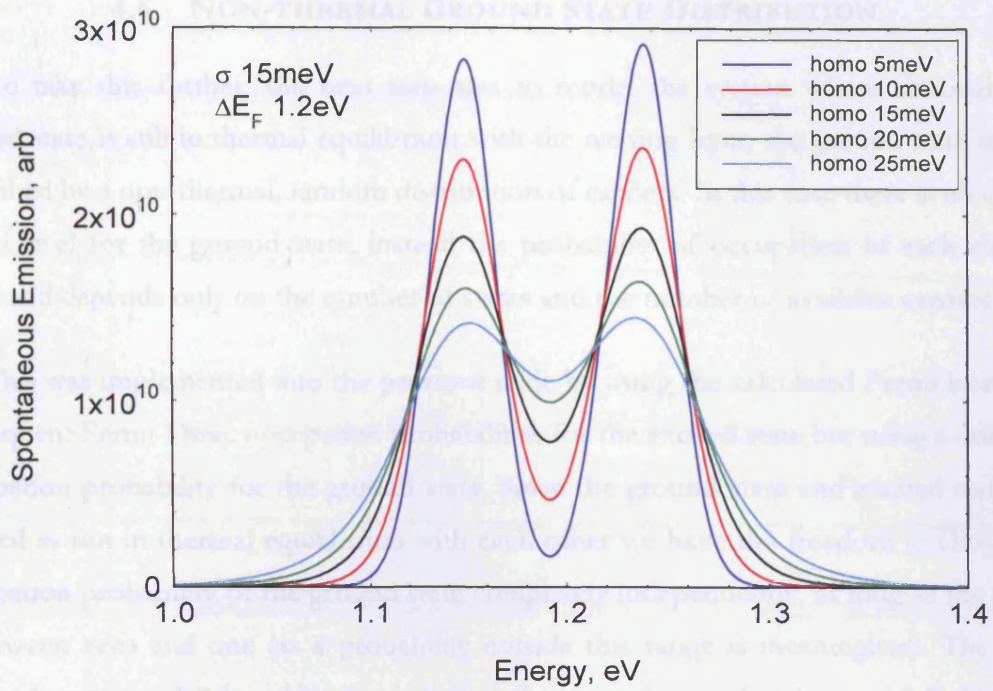


Figure 4.28 Effect on the spontaneous emission spectra of changing the homogeneous broadening, high homogeneous broadening

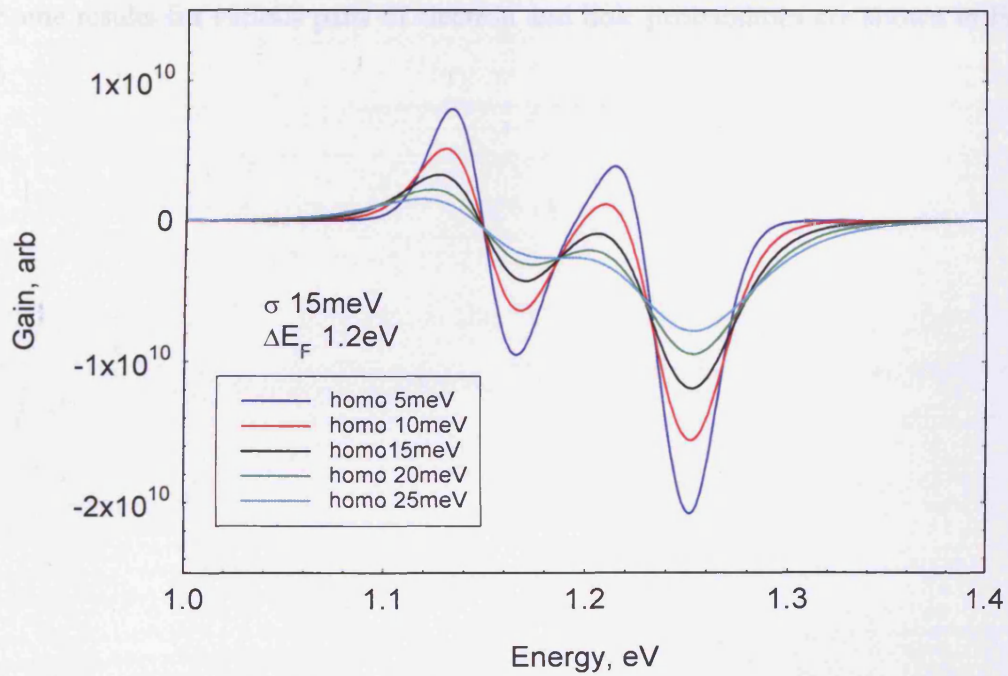


Figure 4.29 Effect on the gain spectra of changing the homogeneous broadening, high homogeneous broadening

4.6 NON-THERMAL GROUND STATE DISTRIBUTION

To take this further, the next step was to model the system where although the excited state is still in thermal equilibrium with the wetting layer, the ground state is best described by a non-thermal, random distribution of carriers. In this case there is no quasi-Fermi level for the ground state, instead the probability of occupation of each state is equal and depends only on the number of states and the number of available carriers.

This was implemented into the previous code by using the calculated Fermi level and subsequent Fermi-Dirac occupation probabilities for the excited state but using a uniform occupation probability for the ground state. Since the ground state and excited state are defined as not in thermal equilibrium with each other we have the freedom to choose the occupation probability of the ground state completely independently, as long as the value is between zero and one (as a probability outside this range is meaningless). The total carrier density can be found by integrating each occupation probability multiplied by the density of states.

Some results for various pairs of electron and hole probabilities are shown in Figure 4.30.

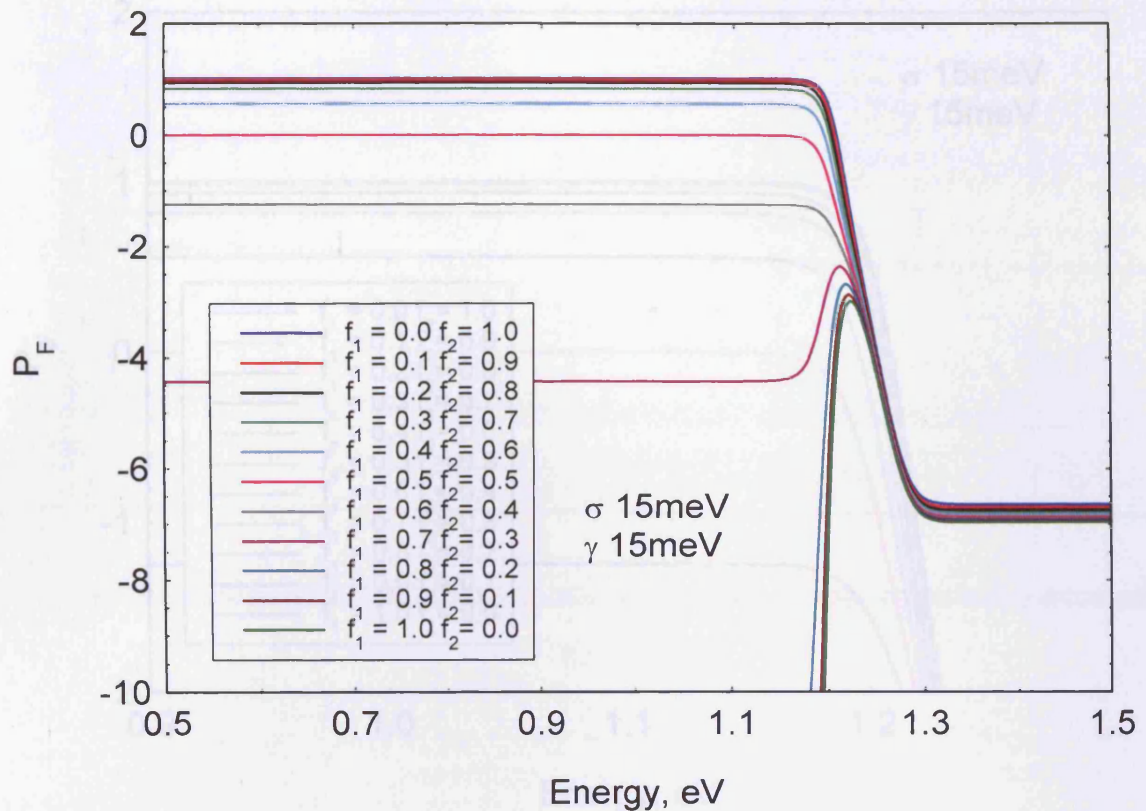


Figure 4.30 Effect on the P_F spectra of changing the ground state population, high homogeneous broadening

If we zoom in to show the y range from -2 to 2 we can see that for occupation probabilities between zero and one, the P_F never exceeds the value of one. This is illustrated in Figure 4.31. The maximum P_F of one is reached when f_1 is zero, so the hole states are fully empty, and f_2 is one, so the electron states are full. This is the situation corresponding to full population inversion. However, as may be obvious, unless either the electron or the hole states are fully populated the function does not tend to one and the calibration procedure cannot rely on the P_F being one.

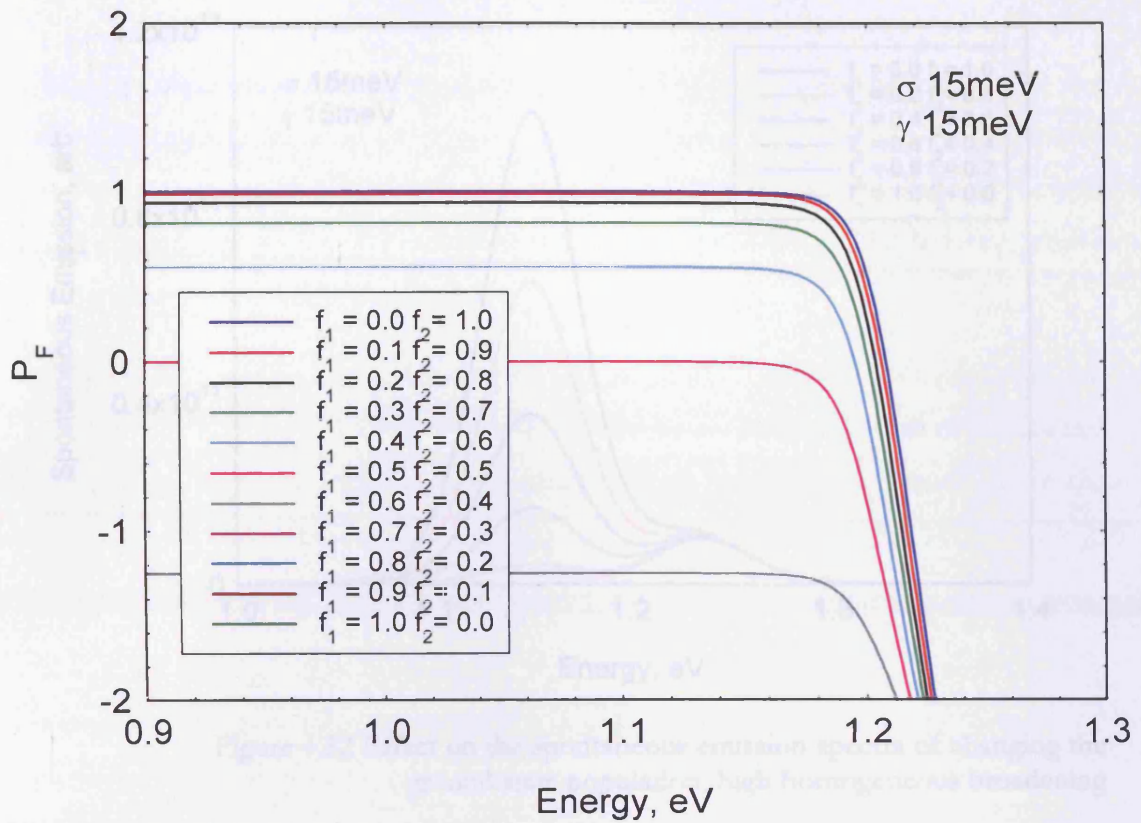


Figure 4.31 Expanded view of Figure 4.30

The corresponding spontaneous emission and gain spectra are shown in Figure 4.32 and Figure 4.33 respectively. These show that the excited state gain and spontaneous emission stay constant throughout, as the excited state quasi-Fermi level separation stays constant but as the population of the ground state increases, due to increasing f_2 and decreasing f_1 , the gain of the ground state varies between full absorption and full gain and the ground state spontaneous emission increases.

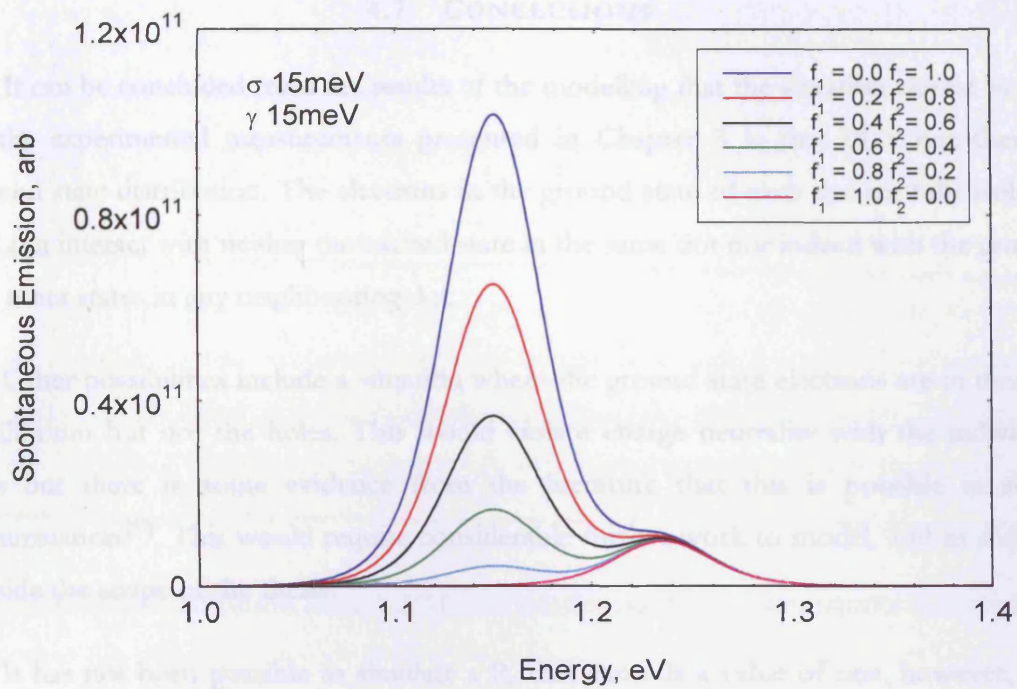


Figure 4.32 Effect on the spontaneous emission spectra of changing the ground state population, high homogeneous broadening

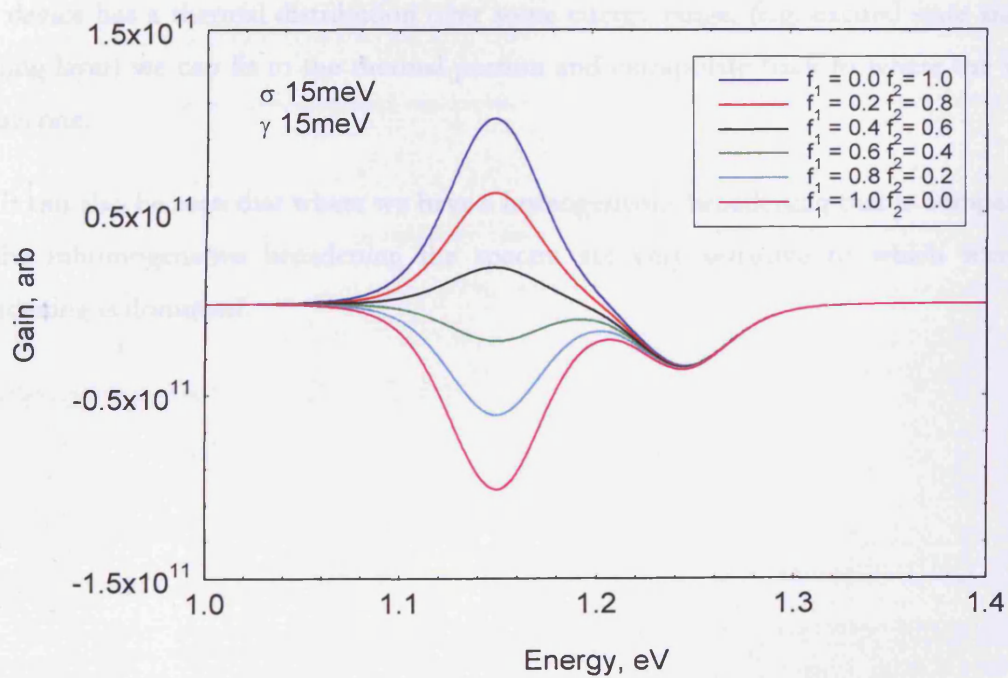


Figure 4.33 Effect on the gain spectra of changing the ground state population, high homogeneous broadening

4.7 CONCLUSIONS

It can be concluded from the results of the modelling that the situation closest to that of the experimental measurements presented in Chapter 3 is that of a non-thermal ground state distribution. The electrons in the ground state of each dot are fully isolated and can interact with neither the excited state in the same dot nor indeed with the ground nor other states in any neighbouring dot.

Other possibilities include a situation where the ground state electrons are in thermal equilibrium but not the holes. This would violate charge neutrality with the individual dots but there is some evidence from the literature that this is possible in some circumstances^[57]. This would require considerable further work to model, and as such, is outside the scope of the thesis.

It has not been possible to simulate a P_F that exceeds a value of one, however, it is clear from the results of the modelling that using the P_F for calibration of the unamplified spontaneous emission spectra does not depend on full thermal distribution. As long as our device has a thermal distribution over some energy range, (e.g. excited state and/or wetting layer) we can fit to the thermal portion and extrapolate back to where the value equals one.

It can also be seen that where we have a homogeneous broadening that is comparable to the inhomogeneous broadening the spectra are very sensitive to which form of broadening is dominant.

5.1 OVERALL RADIATIVE EFFICIENCY

5.1.1 INTRODUCTION

Due to the small area coverage of dots in the junction plane of a quantum dot laser, it has been suggested that electrons may pass through the structure without ever seeing the dots, thus contributing to a lower overall radiative efficiency than would otherwise be achieved. For our structures with dots of diameter 20-25nm and density $5 \times 10^{10} \text{cm}^{-2}$, this area coverage is 20%.

Therefore, to improve the performance of dot laser structures it has further been suggested that the dot layers should be placed within a separate quantum well structure, commonly referred to as a DWELL structure^[1]. This may improve the injection efficiency compared to a standard quantum dot laser as the well layer could provide a more efficient path for carrier capture. Although by the nature of the Stranski-Krastanow growth mechanism the dots are already accompanied by a wetting layer, this layer is extremely narrow and thus has a wide energy separation that may limit its potential usefulness for carrier injection.

In this section, I have determined the relative probability of occupation (P_F spectra) of states for the DWELL, standard quantum dot and our quantum well comparison structures detailed in Chapter 2. This has then been used to calibrate true spontaneous emission measurements and hence calculate the overall radiative efficiency of our devices as detailed in Section 2.5.

In using the P_F spectra to calibrate the spontaneous emission, I have made use of the assumption, from the modelling results in the previous chapter, that we can use the fit over the excited state energies to determine the calibration factor. An example fit is shown in Figure 5.1. The overall radiative efficiency (including both TE and TM contributions) has been calculated as a function of drive current density for each device using the method in Section 2.5. The current density has been calculated from the drive current by using the section length of $300 \mu\text{m}$ and assuming an effective stripe width of $60 \mu\text{m}$ due to current spreading (verified by looking at the near field emission).

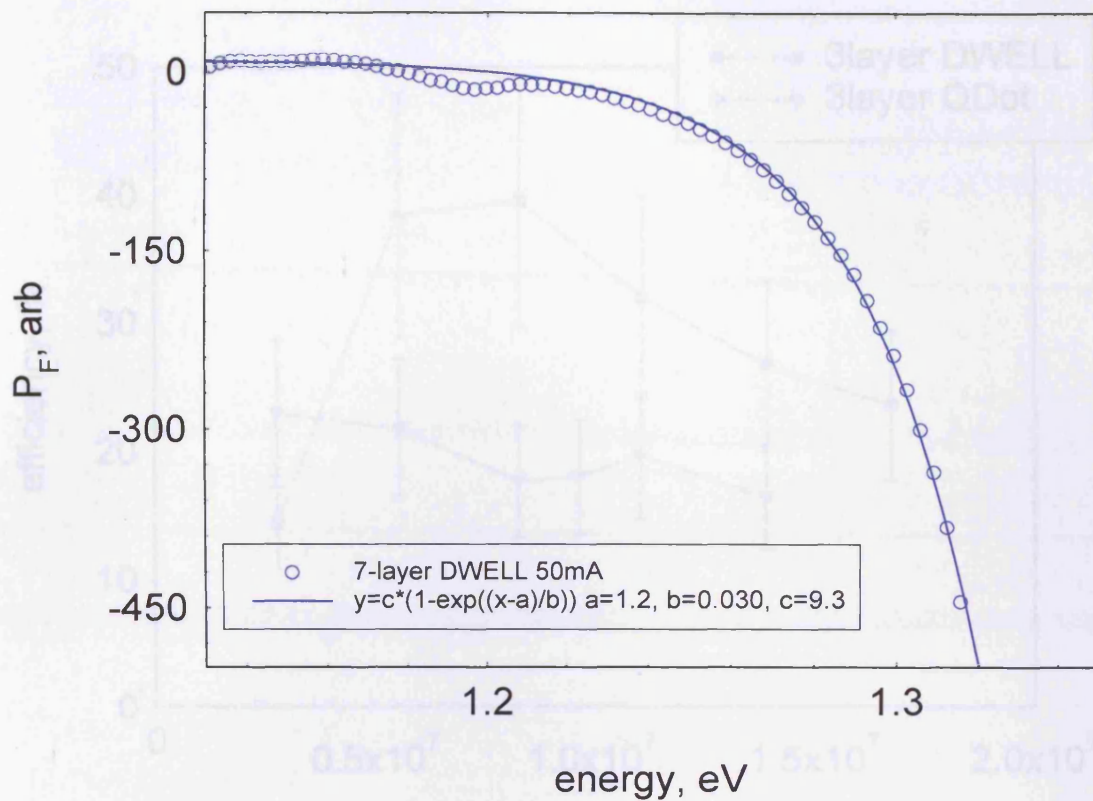


Figure 5.1 Example P_F fit to excited state, extrapolated back to low energies

5.1.2 DOTS IN WELL VERSUS STANDARD QUANTUM DOTS

We start by comparing a three-layer dwell structure and a three-layer standard quantum dot structure in Figure 5.2. The large uncertainty, represented by the error bars, arises largely from the uncertainty in the calibration procedure. However, it still appears from the larger efficiency of the DWELL structure that there is indeed an advantage to using a structure with an added quantum well. The data for the DWELL device also seems to indicate that the efficiency of this structure is more current density dependent than the non-DWELL structure. It is not clear why this would be so.

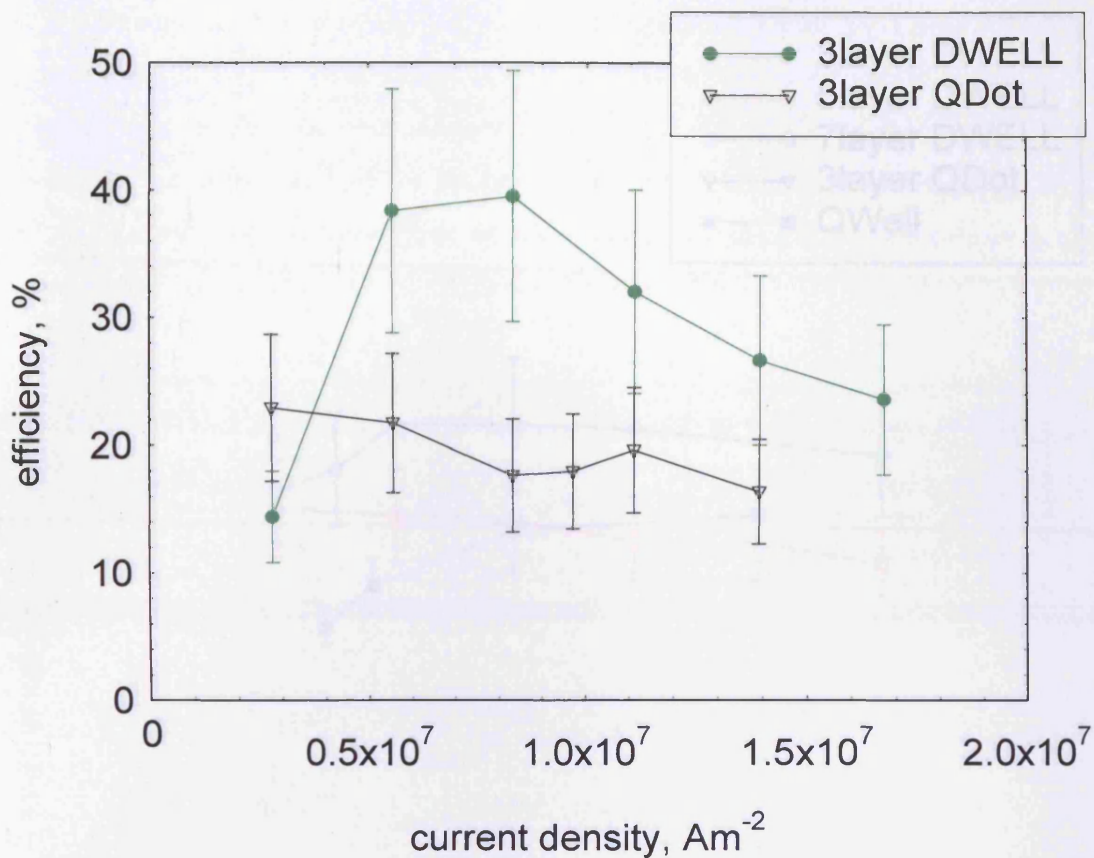


Figure 5.2 Overall radiative efficiency as a function of current density for a three-layer standard quantum dot device and a three-layer DWELL structure

In addition, the results for the five and seven-layer DWELL structures are more similar to the three-layer non-DWELL structure as shown in Figure 5.3, rather than the three-layer DWELL device. All four of the quantum dot structures seem to show a decrease of efficiency with increasing current density, apart from the three-layer DWELL device at low current density, whereas the quantum well device has an efficiency that increases with increasing current density. A radiative efficiency that increases with current density probably arises because the radiative process increases faster with carrier density than the non-radiative process. This is well known for quantum well lasers ^[25].

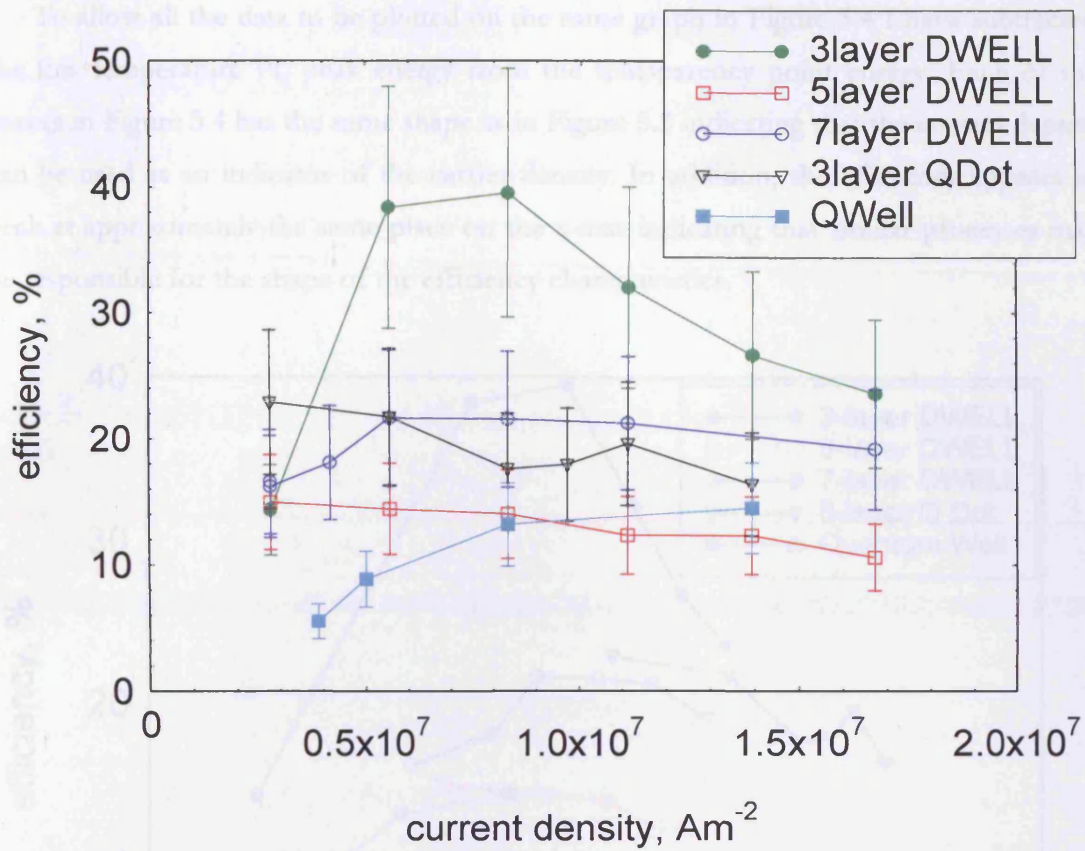


Figure 5.3 Comparison of the radiative efficiency of all the device structures as a function of current density

In a quantum well laser, the radiative process is approximately proportional to $n \times p$ or n^2 whereas Shockley-Read-Hall defect related recombination is proportional to $n^{[25]}$. This would lead to an increase in efficiency with carrier density. A non-radiative process that increases faster than n^2 such as Auger recombination (proportional to n^3) or a thermally activated leakage current would lead to a decrease in radiative efficiency with increasing current or carrier density.

To confirm that the efficiency has the same dependence on carrier density as current density (which might include other extrinsic processes), in particular for the data that exhibits an increase and then a decrease in efficiency, I have plotted the efficiency versus the transparency point energy, which is derived from the gain spectrum. An increasing transparency point implies an increasing carrier density. If the system can be described by Fermi-Dirac statistics, then the transparency point is also the quasi-Fermi level separation.

To allow all the data to be plotted on the same graph in Figure 5.4 I have subtracted the low temperature PL peak energy from the transparency point energy. Each of the curves in Figure 5.4 has the same shape as in Figure 5.3 indicating that the current density can be used as an indicator of the carrier density. In addition, the efficiency appears to peak at approximately the same place on the x-axis indicating that similar processes may be responsible for the shape of the efficiency characteristics.

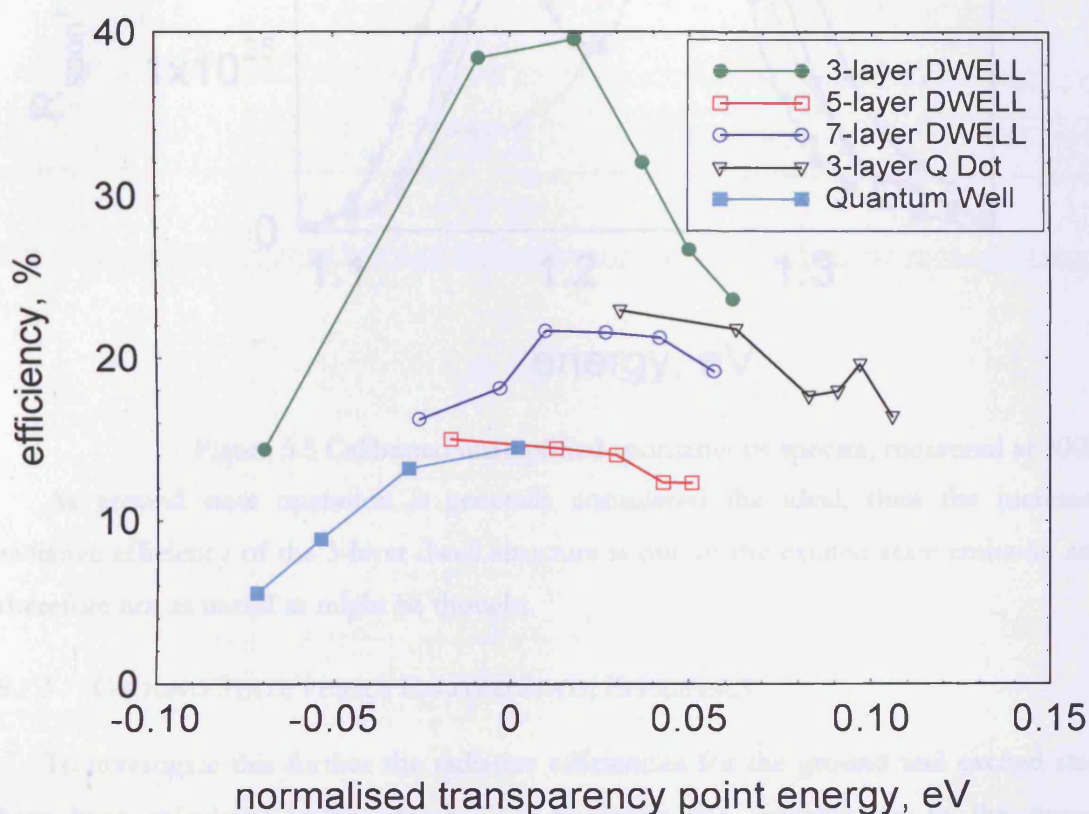


Figure 5.4 Comparison of the radiative efficiency all device structures where the x-axis is the transparency point energy normalised by the subtraction of the low temperature PL peak energy.

If we then look at the calibrated spontaneous emission (Figure 5.5), and choose suitable currents such that the radiative current (area under the calibrated spontaneous emission spectrum) is approximately equal then we can see that the contribution from the excited state is much greater for the 3-layer dwell structure than for the other structures.

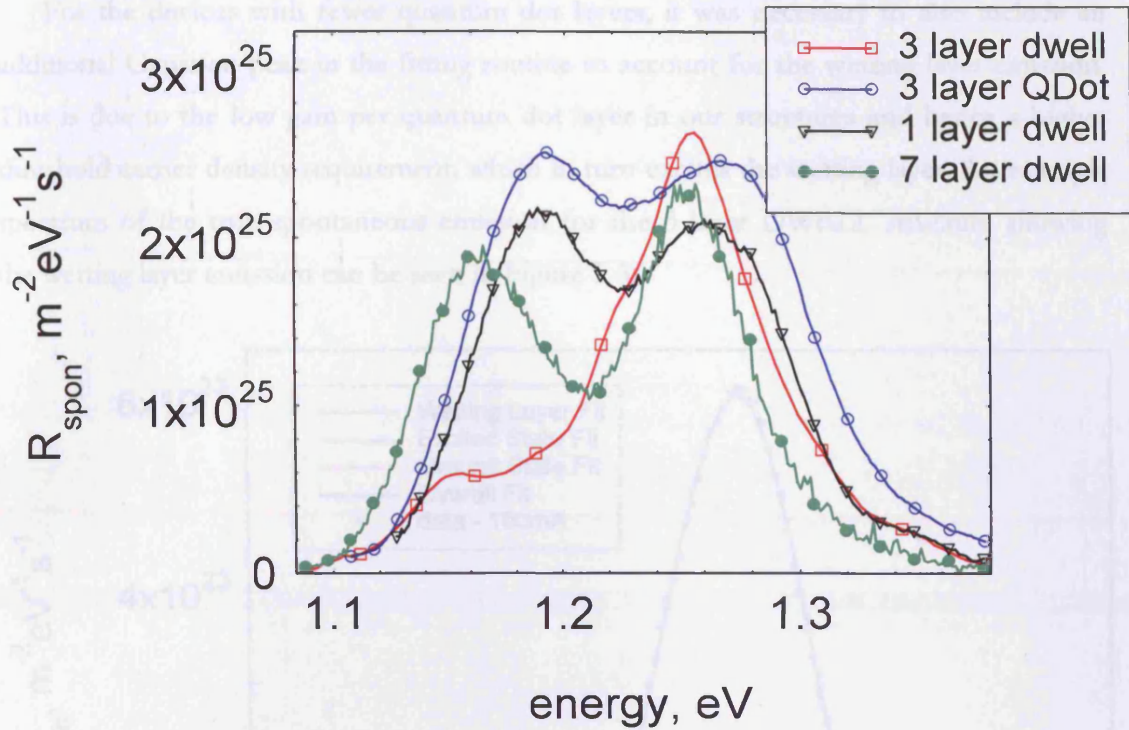


Figure 5.5 Calibrated unamplified spontaneous spectra, measured at 300K

As ground state operation is generally considered the ideal, then the increased radiative efficiency of the 3-layer dwell structure is due to the excited state emission and therefore not as useful as might be thought.

5.1.3 GROUND STATE VERSUS EXCITED STATE EFFICIENCY

To investigate this further the radiative efficiencies for the ground and excited state have been calculated independently. To determine the contribution to the overall radiative efficiency from the ground state, the extent of the ground state emission was determined by fitting the spontaneous emission spectra with two Gaussian curves, one for the ground state emission and one for the excited state emission. It was decided that this was a more accurate way of determining the split than simply taking the halfway point between the peaks, as at energies between the peaks of the ground and excited states there is some contribution from both of the states.

For the devices with fewer quantum dot layers, it was necessary to also include an additional Gaussian peak in the fitting routine to account for the wetting layer emission. This is due to the low gain per quantum dot layer in our structures and hence a higher threshold carrier density requirement, which in turn excites the wetting layer. An example spectrum of the true spontaneous emission for the 3-layer DWELL structure showing the wetting layer emission can be seen in Figure 5.6.

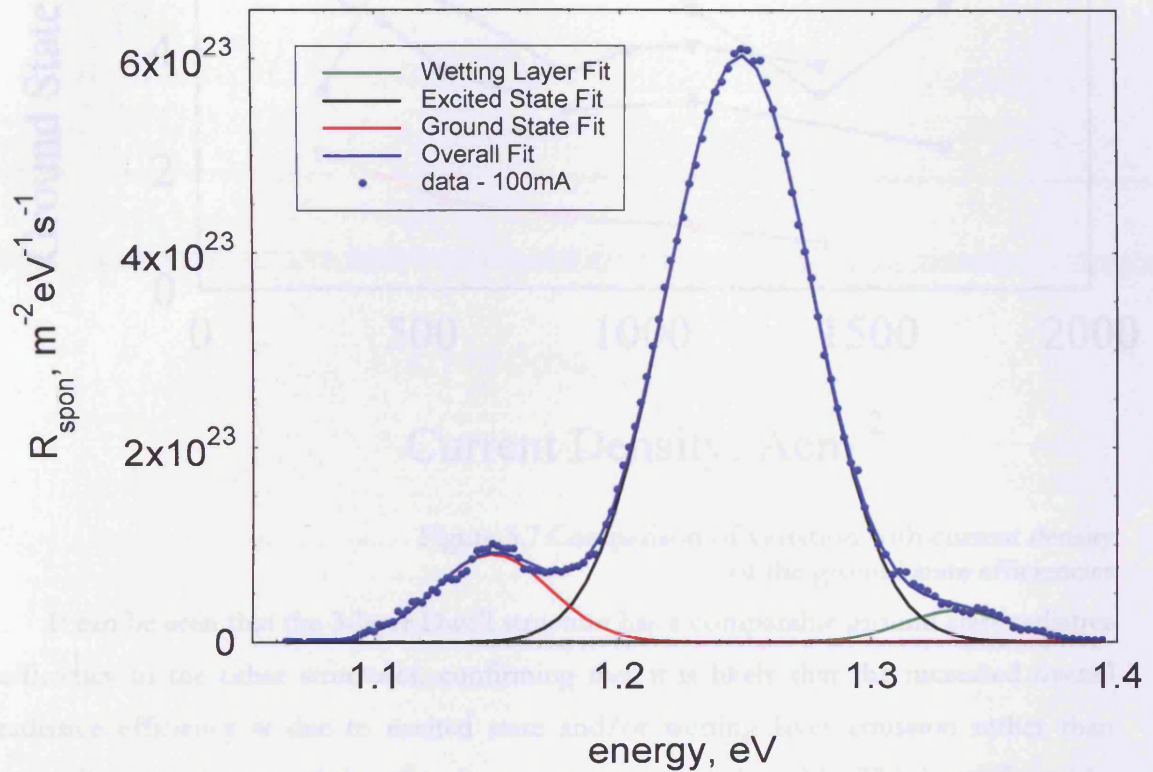


Figure 5.6 The true spontaneous emission spectra fitted with Gaussian contributions from each state, measured at 300K for the five-layer DWELL sample

Once the Gaussian curves have been fitted to the data, it is then possible to calculate the separate efficiencies of each state from the areas under the Gaussian curves. A comparison of the ground state efficiencies is shown in Figure 5.7.

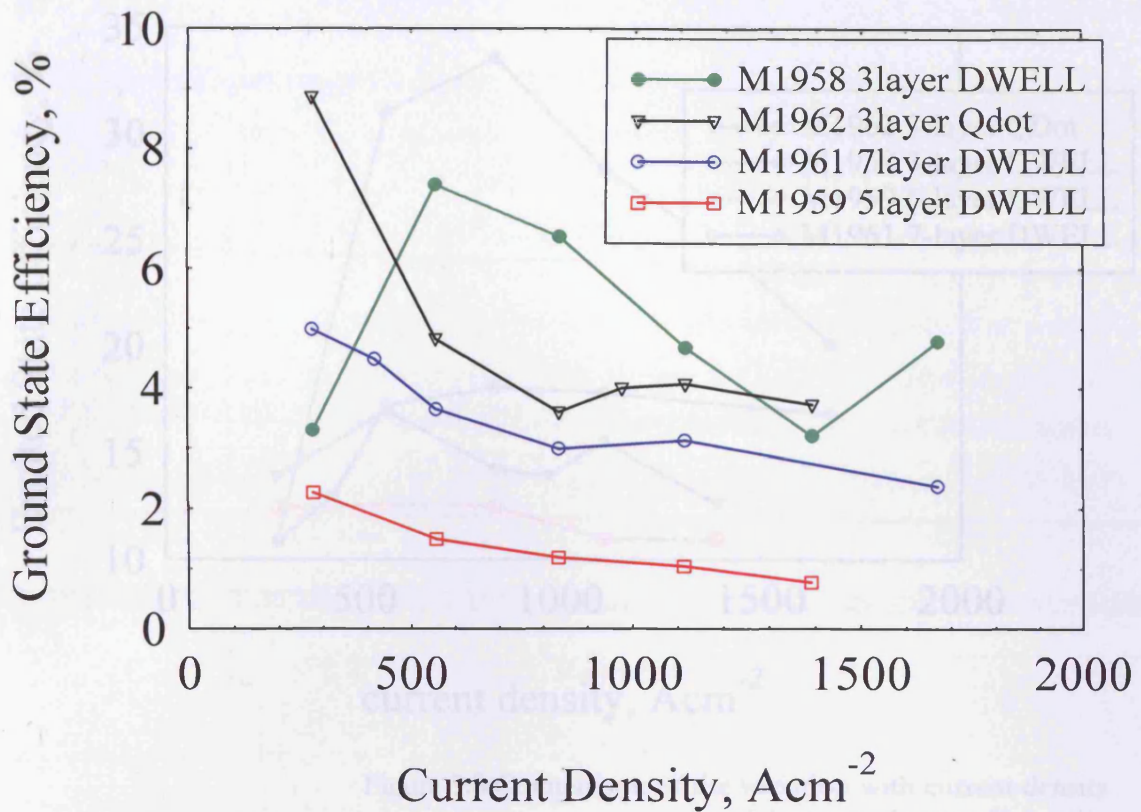


Figure 5.7 Comparison of variation with current density of the ground state efficiencies

It can be seen that the 3-layer Dwell structure has a comparable ground state radiative efficiency to the other structures, confirming that it is likely that the increased overall radiative efficiency is due to excited state and/or wetting layer emission rather than ground state emission and therefore for most purposes undesirable. This is confirmed by looking at the excited state efficiencies as shown in Figure 5.8.

In addition, the relative magnitudes of the spontaneous emission from the ground and excited states may have another effect on device performance through the relative magnitudes of the gain, which are related to the spontaneous emission as described in Section 1.9. Laser action will occur on the peak of the gain spectrum and if the excited state to ground state gain ratio for the three-layer DWELL is larger than the other samples then this device will switch from ground to excited state lasing at a lower injection level. Indeed the peak of the gain spectrum and the lasing wavelength are shifted to higher energy, which is a characteristic of excited state emission for this structure.

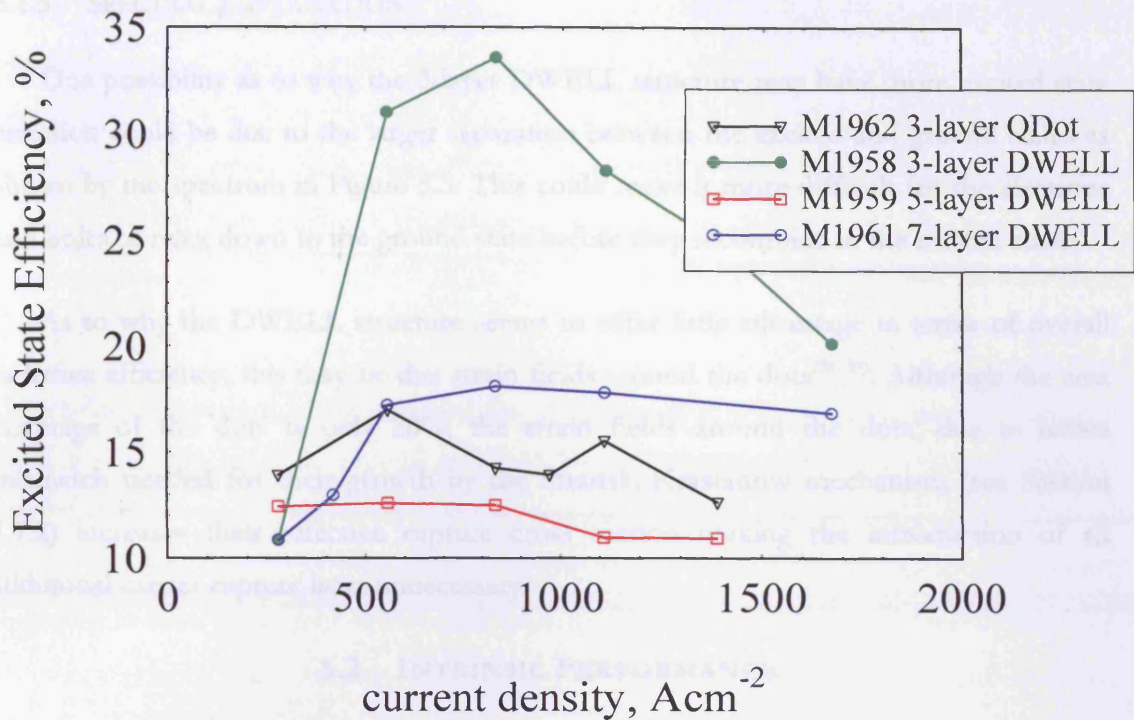


Figure 5.8 Comparison of the variation with current density of the excited state efficiencies

5.1.4 VARIATION WITH CURRENT OF THE EFFICIENCY

If we then look at the variation with current of the excited state radiative efficiency in Figure 5.8, in particular for the 3-layer Dwell structure, we can see that there is an initial increase followed by a gradual decrease.

This initial increase in the excited state efficiency may be explained by the ground state saturating as the current density is increased, hence forcing a greater proportion of the carriers into the excited state. There is then a gradual reduction in efficiency as the losses increase at higher current densities.

This variation with current of the excited state radiative efficiency directly translates into the variation with current of the overall radiative efficiency due the greater proportion of excited state emission.

5.1.5 SPECTRAL EXPLANATION

One possibility as to why the 3-layer DWELL structure may have more excited state emission could be due to the larger separation between the excited and ground states as shown by the spectrum in Figure 5.5. This could make it more difficult for the electrons and holes to relax down to the ground state before they recombine in the excited state.

As to why the DWELL structure seems to offer little advantage in terms of overall radiative efficiency, this may be due strain fields around the dots^[58, 59]. Although the area coverage of the dots is only 20%, the strain fields around the dots, due to lattice mismatch needed for their growth by the Stranski-Krastanow mechanism (see Section 1.7.2) increases their effective capture cross section making the introduction of an additional carrier capture layer unnecessary.

5.2 INTRINSIC PERFORMANCE

5.2.1 INTRODUCTION

To investigate the level of device performance that may be possible from optimised quantum dot lasers, in this section I will investigate the intrinsic performance.

In Section 5.2.2 I first look at the gain versus the total current density in order to check that the threshold currents predicted from the multisection gain devices are comparable to those measured in from our Fabry-Perot laser devices. These curves are also used to investigate the form of the fitting equation that is most appropriate for our devices.

In Section 5.2.3 the gain has then been plotted against the radiative current density calculated, as in Section 5.1 above, from the area under the calibrated spontaneous emission spectra. The spontaneous radiation current at threshold would be the lasing threshold value in the absence of non-radiative recombination^[60]. As ground state operation is the most important, I have then gone on to look at the ground state gain both versus the overall radiative current density and versus the ground state radiative current density.

From these results, it is possible to determine the intrinsic performance of the quantum dots and hence predict the ultimate limits on device performance, for example, what might be the lowest possible threshold currents that could be achieved with a fully optimised quantum dot laser with the same degree of inhomogeneous broadening. This could be further improved on if the inhomogeneous broadening could be reduced. These predictions can then be compared to the best results already published and discussed in Section 2.3.3.

The choice of number of layers of dots is important, as there is a trade off between the lower transparency current density and the differential gain. A lower transparency current density may be achieved through use of a lower number of dot layers^[61] (due to the lower number of dots that need to be populated) but for finite device lengths and uncoated facets, the higher differential (and total) gain that may be achieved by using multiple layers of dots can give lower threshold current densities. The data presented in the following sections is all for the seven-layer DWELL sample.

5.2.2 GAIN - CURRENT CURVES

By plotting the peak of the modal gain (measured net modal gain plus the measured loss), obtained using the multisection technique, against the current density, it is possible to determine the transparency current density (zero gain) from the intercept of the gain curve with the current density axis. If we then calculate the distributed mirror losses for various typical device lengths, we can calculate the threshold current densities for these device lengths and compare these to our laser devices processed from the same material. The threshold gain is equal to the sum of the internal loss, α_i , and the distributed mirror loss, α_M . The distributed mirror loss can be calculated using Equation 5.1 where L_c is the cavity length and R is the power reflectivity of the mirrors.

$$\alpha_M = \frac{1}{L_c} \ln\left(\frac{1}{R}\right)$$

Equation 5.1

The experimental points of the gain versus current density curve are commonly fitted by a curve of the form given in Equation 5.2, where J_{tr} is the transparency current density, and shown in Figure 5.9. This form is due to McIlroy^[16] and is appropriate for a quantum well where the gain of a single pair of sub-bands saturates at high currents.

$$G = G_o \ln\left(\frac{J}{J_{tr}}\right)$$

Equation 5.2

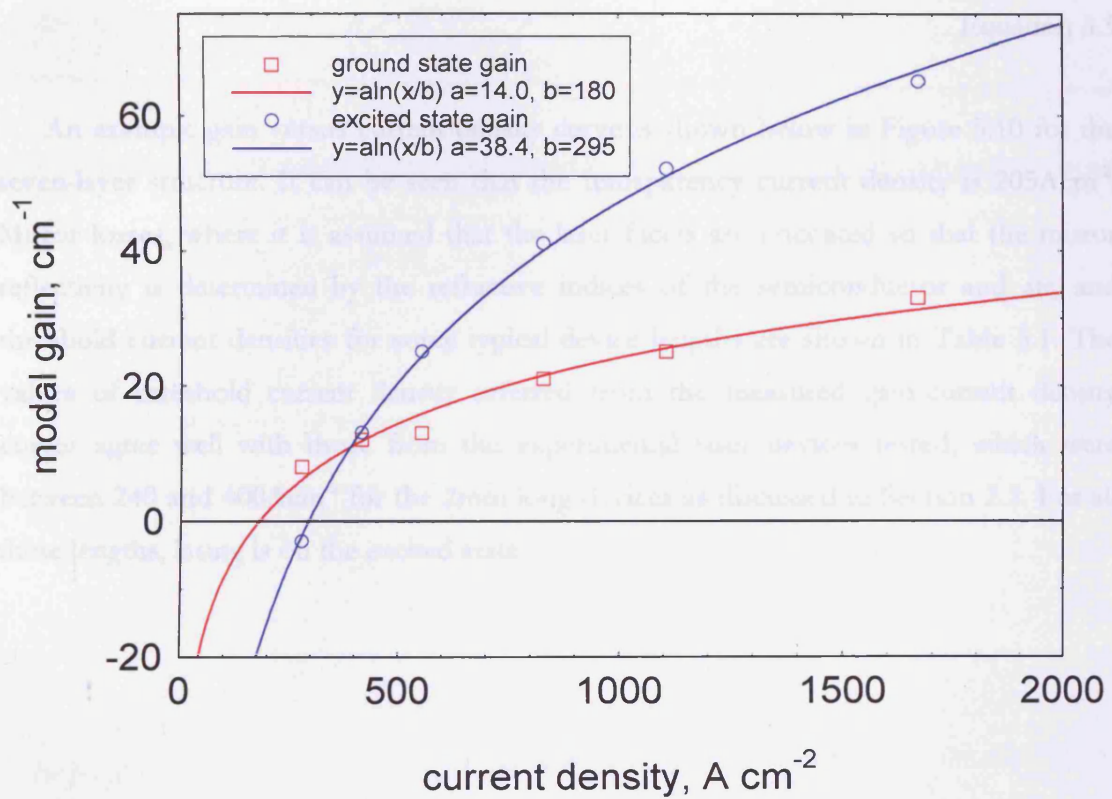


Figure 5.9 Experimental gain-current density curve fitted with $g=g_o \ln(J/J_{tr})$ for the seven-layer structure

However, it has been suggested that this form may not be suitable for quantum dot devices, and an alternative form is given by Zhukov et al^[62] and shown in Equation 5.3, where J_{tr} is the transparency current density and G_{sat} is the saturated value of the modal gain and γ is a fitting parameter. It is this form of equation that I have made use of throughout the remainder of this section.

$$G = G_{sat} \left[1 - \exp\left(-\gamma \frac{J - J_{tr}}{J_{tr}}\right) \right]$$

Equation 5.3

An example gain versus current density curve is shown below in Figure 5.10 for the seven-layer structure. It can be seen that the transparency current density is 205Acm^{-2} . Mirror losses, where it is assumed that the laser facets are uncoated so that the mirror reflectivity is determined by the refractive indices of the semiconductor and air, and threshold current densities for some typical device lengths are shown in Table 5.1. The values of threshold current density inferred from the measured gain-current density curves agree well with those from the experimental laser devices tested, which were between 240 and 400Acm^{-2} for the 2mm long devices as discussed in Section 2.3. For all these lengths, lasing is on the excited state.

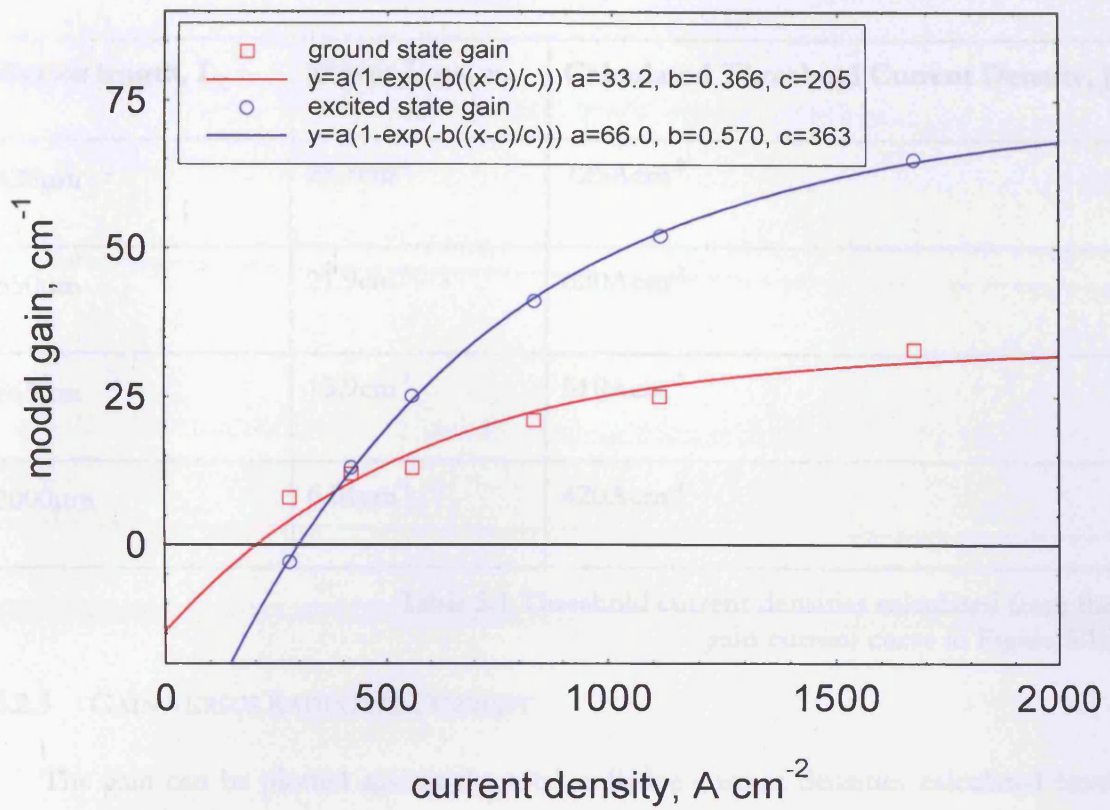


Figure 5.10 Example gain current curves showing ground state and excited state peak gain for the seven-layer structure

Device length, L_C	Mirror Loss, α_M	Calculated Threshold Current Density, J_{th}
420 μm	28.7 cm^{-1}	725 Acm^{-2}
550 μm	21.9 cm^{-1}	620 Acm^{-2}
865 μm	13.9 cm^{-1}	510 Acm^{-2}
2000 μm	6.01 cm^{-1}	420 Acm^{-2}

Table 5.1 Threshold current densities calculated from the gain current curve in Figure 5.10

5.2.3 GAIN VERSUS RADIATIVE CURRENT

The gain can be plotted against the total radiative current densities calculated from the integral of the calibrated spontaneous emission curves. This is shown in Figure 5.11 for the seven-layer sample. This shows us the transparency current density that, in theory, could be achieved if we could eliminate all non-radiative current paths within the device. This gives a value of 23 Acm^{-2} , comparable with the best-reported threshold current densities discussed in Section 2.3.3. The calculated spontaneous current densities required to achieve threshold gain for some typical device lengths are shown in Table 5.2.

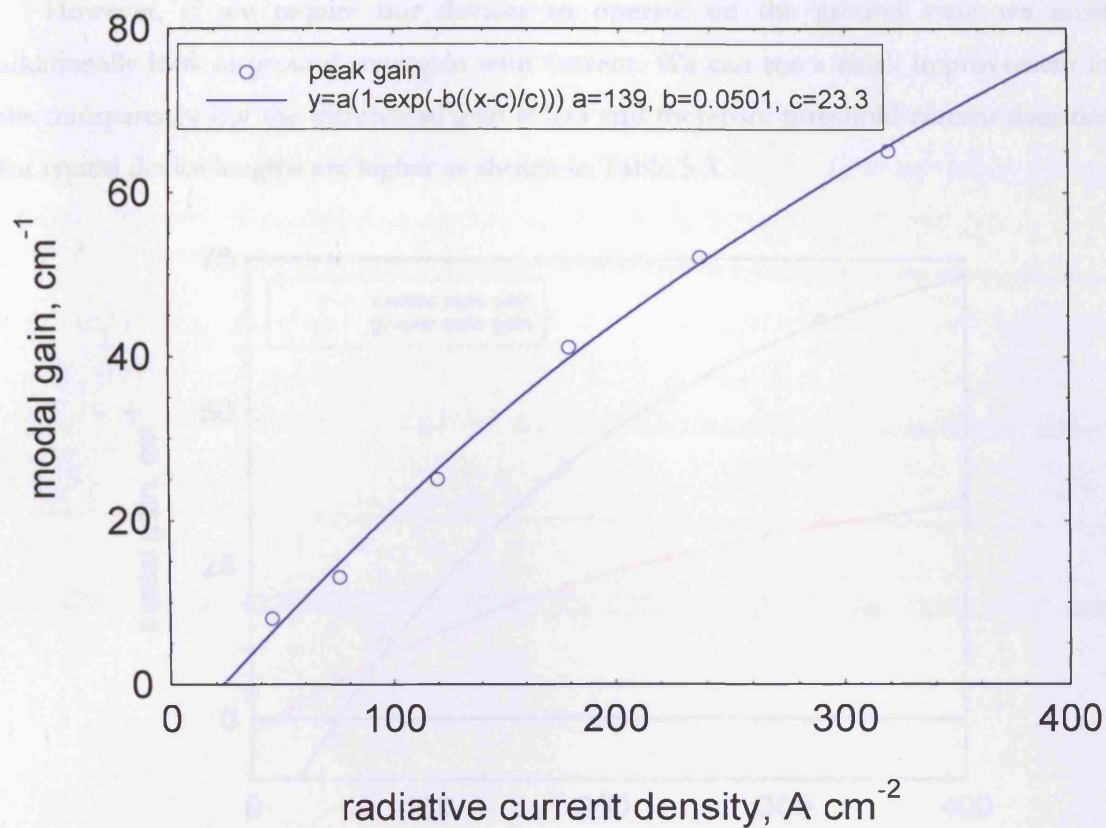


Figure 5.11 Seven-layer sample - peak gain versus radiative current density

Device length, L_C	Mirror Loss, α_M	Threshold Current Density, J_{th}
420 μm	28.7 cm^{-1}	160 Acm^{-2}
550 μm	21.9 cm^{-1}	131 Acm^{-2}
865 μm	13.9 cm^{-1}	99 Acm^{-2}
2000 μm	6.01 cm^{-1}	69 Acm^{-2}

Table 5.2 Threshold current densities calculated from the peak gain versus radiative current density

However, if we require our devices to operate on the ground state we must additionally look at ground state gain with current. We can see a small improvement in the transparency but the differential gain is less and therefore threshold current densities for typical device lengths are higher as shown in Table 5.3.

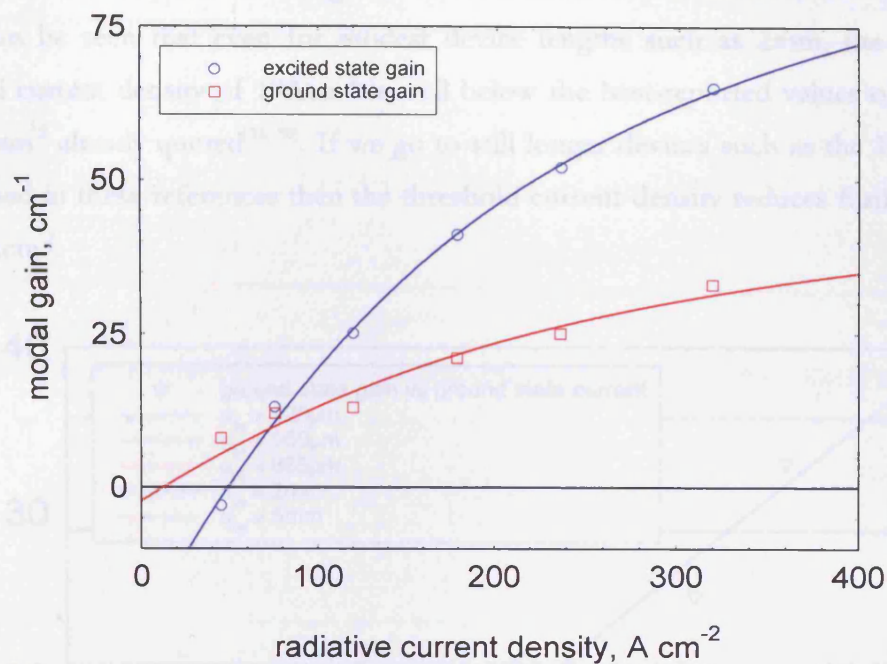


Figure 5.12 Seven-layer sample – ground state and excited state gain versus radiative current density

Device length, L_C	Mirror Loss, α_M	Threshold Current Density, J_{th}
420 μm	28.7 cm^{-1}	420 Acm^{-2}
550 μm	21.9 cm^{-1}	275 Acm^{-2}
865 μm	13.9 cm^{-1}	170 Acm^{-2}
2000 μm	6.01 cm^{-1}	100 Acm^{-2}

Table 5.3 Threshold current densities calculated from the ground state gain versus radiative current density

It is clear that considerable current is being lost through excited state emission. If we then look at the ground state gain plotted against the ground state radiative current density, we can predict the ultimate performance that could be possible if excited state emission could be eliminated. This is shown in Figure 5.13. A transparency current density of 6Acm^{-2} is predicted along with the threshold current densities shown in Table 5.4. It can be seen that even for modest device lengths such as 2mm, the predicted threshold current density of 19Acm^{-2} is well below the best-reported values of 24Acm^{-2} and 25Acm^{-2} already quoted^[35, 36]. If we go to still longer devices such as the 19.2mm or 14mm used in these references then the threshold current density reduces further to less than 14Acm^{-2} .

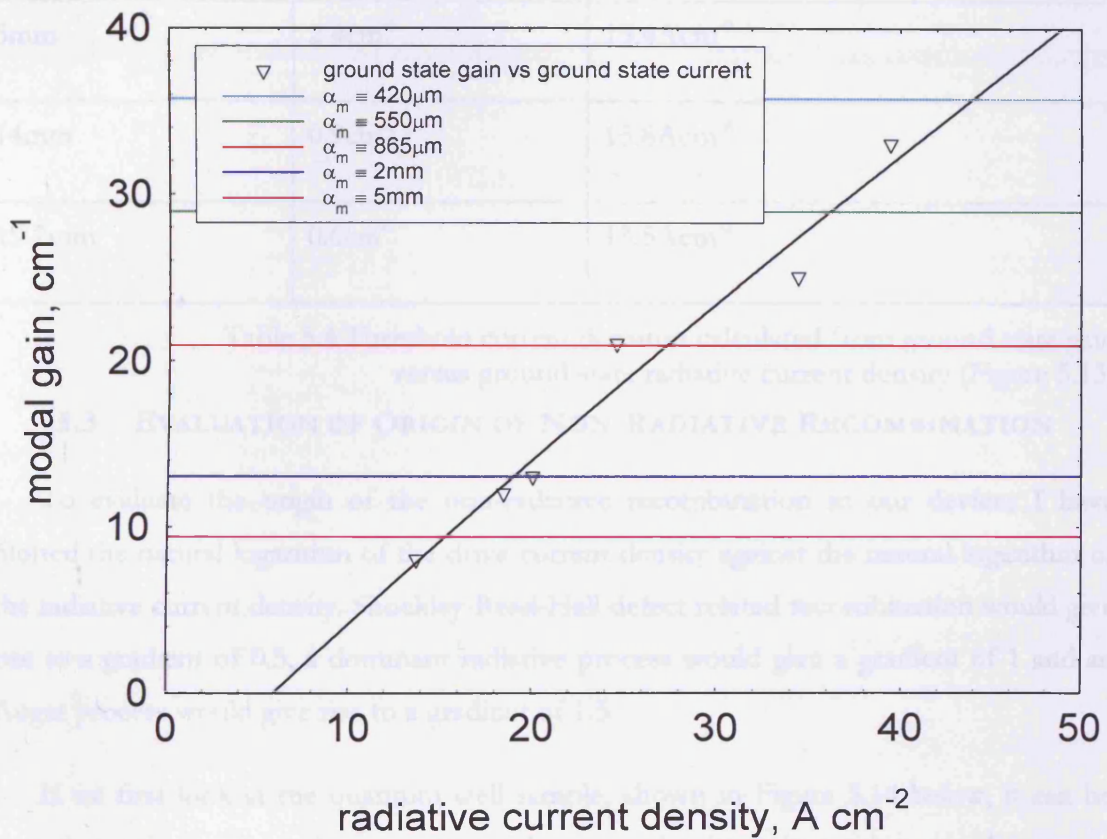


Figure 5.13 Seven-layer sample - ground state gain versus ground state radiative current density

Device length, L_C	Mirror Loss, α_M	Threshold Current Density, J_{th}
420 μ m	28.7 cm^{-1}	43.9 Acm^{-2}
550 μ m	21.9 cm^{-1}	36.3 Acm^{-2}
865 μ m	13.9 cm^{-1}	27.4 Acm^{-2}
2mm	6.01 cm^{-1}	19.0 Acm^{-2}
5mm	2.4 cm^{-1}	15.4 Acm^{-2}
14mm	0.9 cm^{-1}	13.8 Acm^{-2}
19.2mm	0.6 cm^{-1}	13.5 Acm^{-2}

Table 5.4 Threshold current densities calculated from ground state gain versus ground state radiative current density (Figure 5.13)

5.3 EVALUATION OF ORIGIN OF NON-RADIATIVE RECOMBINATION

To evaluate the origin of the non-radiative recombination in our devices I have plotted the natural logarithm of the drive current density against the natural logarithm of the radiative current density. Shockley-Read-Hall defect related recombination would give rise to a gradient of 0.5, a dominant radiative process would give a gradient of 1 and an Auger process would give rise to a gradient of 1.5.

If we first look at the quantum well sample, shown in Figure 5.14 below, it can be seen that at low current densities the total current density is increasing at a slower rate than the radiative current density. These current densities would be equivalent to around threshold in a laser device. Following the discussion in section 5.1.2, this would indicate that a Shockley-Read-Hall defect related recombination was dominating. As the current increases the gradient approaches one.

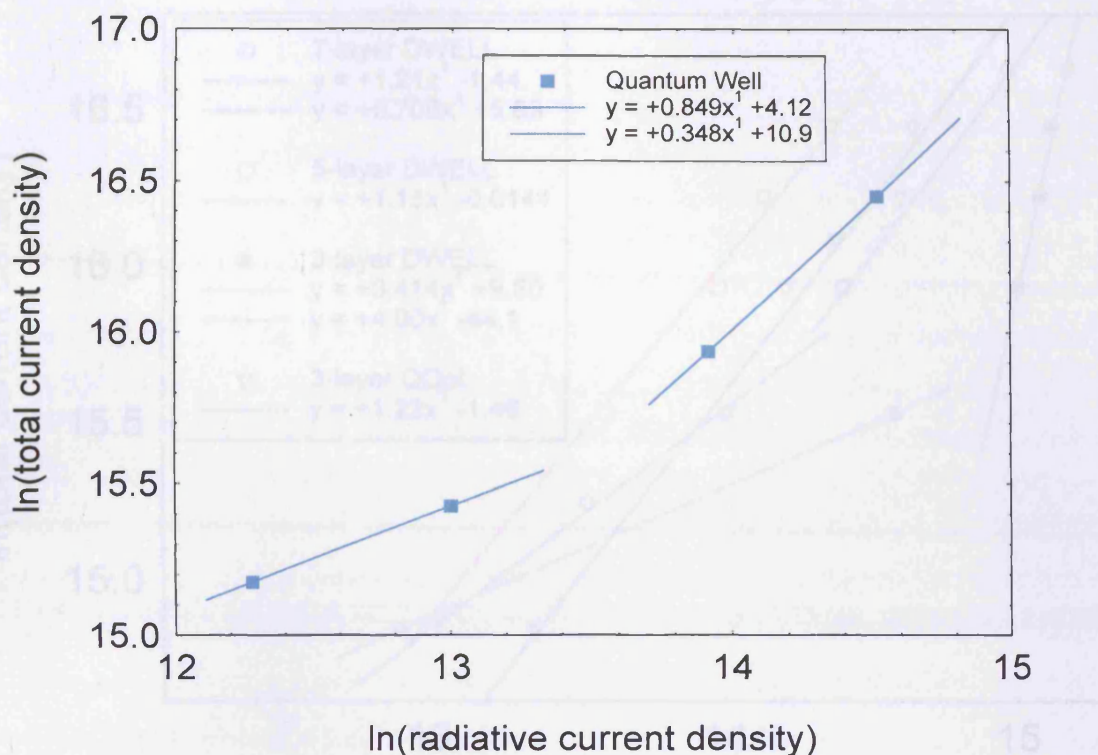


Figure 5.14 Ln (drive current) versus ln (radiative current density) for the quantum well sample, measured at 300K

If we then look at the quantum dot devices, shown in Figure 5.15 below, we can see that for both the five-layer DWELL sample and the three-layer quantum dot sample that gradient is slightly over one suggesting that radiative recombination dominates but that some Auger or thermally activated leakage process may be present. The seven-layer DWELL sample is similar at high current densities but may additionally have some defect related recombination present at lower current densities.

The three-layer DWELL sample however shows a markedly different behaviour. At high current densities there is a very steep gradient suggesting that an Auger or thermally activated leakage process dominates. A thermally activated leakage process would be consistent with the excited state and wetting layer emission observed in the unamplified spontaneous emission spectra shown in Figure 3.10 and the reduction in radiative efficiency at high current densities shown in Figure 5.3.

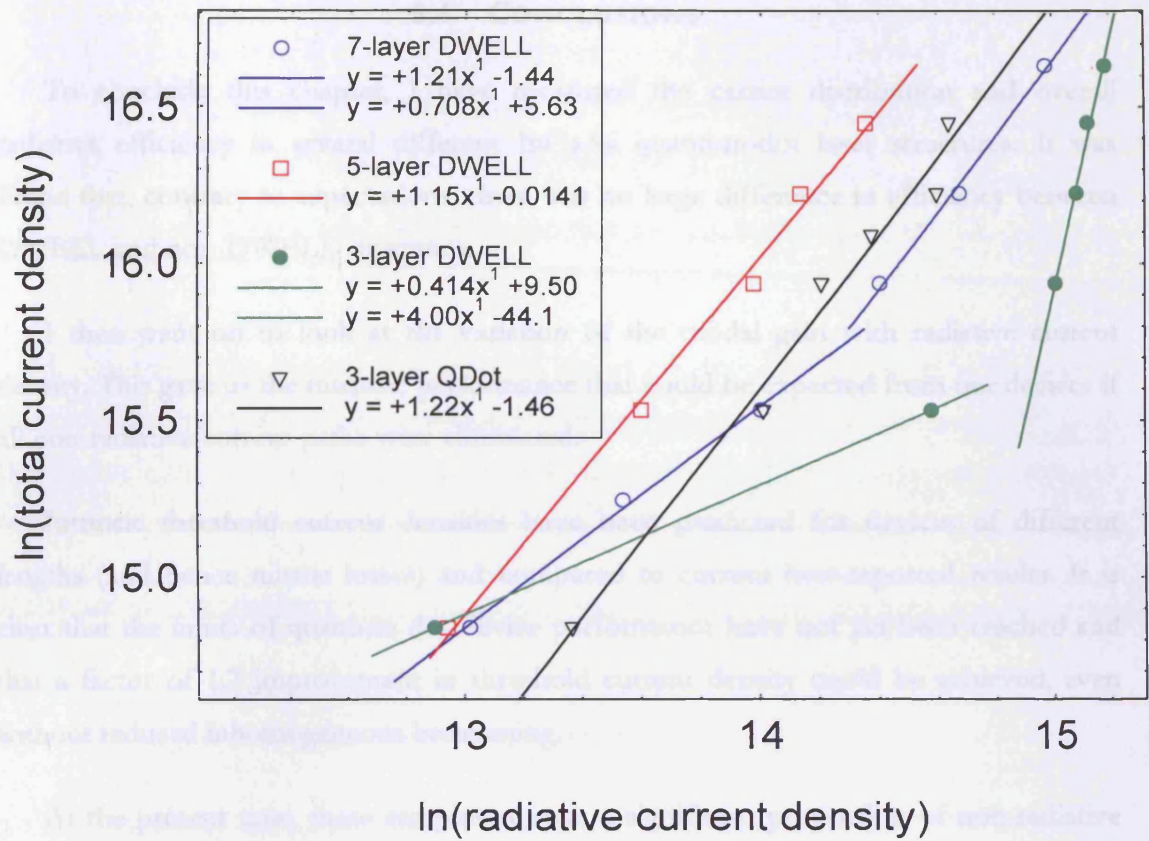


Figure 5.15 Ln (drive current) versus ln (radiative current density) for the quantum dot samples, measured at 300K

5.4 CONCLUSIONS

To conclude this chapter, I have measured the carrier distribution and overall radiative efficiency in several different InGaAs quantum-dot laser structures. It was found that, contrary to expectations, there was no large difference in efficiency between DWELL and non-DWELL structures.

I then went on to look at the variation of the modal gain with radiative current density. This gave us the intrinsic performance that could be expected from our devices if all non-radiative current paths were eliminated.

Intrinsic threshold current densities have been predicted for devices of different lengths (and hence mirror losses) and compared to current best-reported results. It is clear that the limits of quantum dot device performance have not yet been reached and that a factor of 1.7 improvement in threshold current density could be achieved, even without reduced inhomogeneous broadening.

At the present time, these samples contain a significant proportion of non-radiative recombination. Initial measurements indicate that Shockley-Read-Hall recombination is present with the addition of at least one other non-radiative process at higher current densities. A thermally activated leakage process is likely as the dominant mechanism at higher current densities.

6.1 SUMMARY

In this thesis, I have investigated the physics and performance of InGaAs quantum dot lasers through several means.

In Chapter 2 I compared the threshold characteristics of laser devices with multiple layers of dots with the best comparable devices reported in the literature^[35-37]. With threshold current densities for our devices between $240\text{-}400\text{Acm}^{-2}$ compared to 24Acm^{-2} in the literature, I suspected that non-radiative recombination must play a major role in increasing the threshold currents densities. The following chapters then looked at how we could separate out the non-radiative processes by looking at the radiative current only and use this to evaluate the intrinsic radiative performance we might obtain if we could remove these extrinsic non-radiative mechanisms.

In Chapter 3 I have experimentally measured the gain and unamplified spontaneous emission spectra as a function of current for a selection of quantum dot structures and a quantum well structure using a multisection device^[40]. The quotient of the gain and spontaneous emission spectra were then used to calculate the P_F spectra, needed to calibrate the spontaneous emission spectra and hence obtain the radiative current, and investigate the carrier distribution within the devices.

Devices with one or three layers of dots (and the quantum well device) showed a P_F spectra that is consistent with that derived from Fermi-Dirac statistics and hence are determined to be in thermal equilibrium. Devices with more layers dots (e.g. five and seven layers of dots) showed an unusual set of P_F spectra. This was determined to be due to a non-thermal distribution of carriers in the ground state by looking at the variation with current of the unamplified spontaneous emission spectra. This showed a blue shift of the peak wavelength for the excited state with increasing current, consistent with band filling effects, but no shift, or a slight red shift of the peak wavelength of the ground state with current due to some non-thermal carrier distribution at these energies.

For the devices that were not in thermal equilibrium, it was unclear how best to use the P_{F} spectra to calibrate the unamplified spontaneous emission spectra. Therefore, in the next chapter, Chapter 4, a simple model was developed to investigate the effects of several non-thermal carrier distributions on the calculated P_{F} spectra. From this modelling it was deduced that whilst determining the absolute form of the non-thermal ground state distribution was beyond the scope of the model developed, it was possible to use a fit of a thermal P_{F} to the excited state P_{F} and extrapolate back to where it tends to one to calibrate the measured unamplified spontaneous emission spectra. Where the homogeneous broadening is of a value comparable to the inhomogeneous broadening, the resultant P_{F} , gain and spontaneous emission spectra are sensitive to the exact balance between the homogeneous and inhomogeneous broadenings.

Finally, this calibration was used in Chapter 5 to calculate the radiative current densities and hence to calculate and compare the radiative efficiencies of different quantum dot structures, including both Dots in Well (DWELL) and standard quantum dot structures. It was found that there was no large difference in efficiency due to improved carrier injection in the DWELL structures compared to the standard quantum dot structures.

The calculated radiative current densities were also used to plot the gain-radiative current curves and hence predict the minimum transparency and threshold current densities that may be possible in the future with a fully optimised quantum dot laser. It is clear that the limits of quantum dot device performance have not yet been reached and that a factor of 1.7 improvement in threshold current density could be achieved, even without reduced inhomogeneous broadening.

Our samples currently contain a significant proportion of non-radiative recombination. Initial measurements indicate that Shockley-Read-Hall recombination is present with the addition of at least one other non-radiative process at higher current densities. A thermally activated leakage process is likely as the dominant mechanism at higher current densities.

6.2 FURTHER WORK

It would be interesting to investigate the behaviour of the samples over an extended temperature range. For the one and three-layer samples that we believe are in thermal equilibrium at room temperature, the gain and spontaneous emission measurements could be repeated at lower temperatures where we may expect the thermal equilibrium would breakdown. For the samples with more layers of dots, it would be interesting to see if they come back into thermal equilibrium at higher temperatures.

To further investigate the non-radiative processes active in our devices, the radiative efficiency could be measured at lower temperatures. This should reduce any thermally activated leakage current paths.

Other possibilities for further extension of this thesis would be to increase the scope of the simple theoretical model presented in Chapter 4 by treating the dots individually. This would allow us to take account of the localisation of the electrons and holes in an individual dot.

Additionally, the methods employed in this work could also be applied to dots operating at other wavelengths or different material systems. For example dots offer the advantage of extending the emission wavelength of GaAs based devices to the fibre optic telecommunication window of 1.3-1.55 μm ^[63]. It has also been suggested that quantum dot like states may exist GaInN/ GaN structures due to fluctuations in the local indium content.^[64]

REFERENCES

1. Lester, L.F., A. Stintz, H. Li, T.C. Newell, E.A. Pease, B.A. Fuchs, and K.J. Malloy, *Optical characteristics of 1.24- μ m InAs quantum-dot laser diodes*. IEEE Photonics Technology Letters, 1999. **11**(8): p. 931-933.
2. Basov, N.G., O.N. Kroklin, and Y.M. Popov, *Production of negative-temperature states in p-n junctions of degenerate semiconductors*. Pis'ma Zh. Eksp. Theor. Fiz., 1961. **40**: p. 1320.
3. Hall, R.N., G.E. Fenner, J.D. Kingsley, T.J. Soltys, and R.O. Carlson, *Coherent light emission from GaAs p-n junctions*. Physical Review Letters, 1962. **9**: p. 366.
4. Holonyak, N. and S.F. Bevacqua, *Coherent (visible) light emission from Ga (As_{1-x}P_x) junctions*. Applied Physics Letters, 1962. **1**: p. 82.
5. Nathan, M.I., W.P. Dumke, G. Burns, F.H. Dill, and G.J. Lasher, *Stimulated emission of radiation from GaAs p-n junctions*. Applied Physics Letters, 1962. **1**: p. 62.
6. Quist, T.M., R.H. Rediker, R.J. Keyes, W.E. Krag, B. Lax, A.L. McWhorter, and H.J. Zeiger, *Semiconductor maser of GaAs*. Applied Physics Letters, 1962. **1**: p. 91.
7. Alferov, Z.I., V.M. Andreev, V.I. Korol'kov, E.L. Portnoi, and D.N. Tret'yakov, *Injection properties of n-Al_xGa_{1-x}p-GaAs heterojunctions*. Fiz. Tekh. Poluprov., 1969. **2**: p. 1016.
8. Hayashi, M.B. Panish, and P.W. Foy, *A low threshold room temperature injection laser*. IEEE Journal of Quantum Electronics, 1969. **QE5**: p. 211.
9. Kressel, H. and H. Nelson, *Close confinement gallium arsenide PN junction lasers with reduced optical loss at room temperature*. RCA Rev., 1969. **30**: p. 106.
10. Hayashi, M.B. Panish, P.W. Foy, and S. Sumski, *Junction lasers which operate continuously at room temperature*. Applied Physics Letters, 1970. **17**: p. 109.
11. Alferov, Z.I., V.M. Andreev, D.Z. Garbuzov, Yu.V. Zhilyaev, E.P. Morozov, E.L. Portnoi, and V.G. Triofim, *Investigation of the influence of the AlAs-GaAs heterostructure parameters on the laser threshold current and the realization of continuous emission at room temperature*. Fiz. Tekh. Poluprov., 1971. **4**: p. 1826.
12. Einstein, A., Z. Phys., 1917. **18**: p. 121-128.
13. Shockley, W. and W.T. Reed, *Statistics of the recombination of holes and electrons*. Physics Review, 1952. **87**(5): p. 835-842.
14. Hall, R.N., *Electron-Hole recombination in germanium*. Physics Review, 1952. **87**: p. 387.
15. Thompson, G.H.B., *Physics of Semiconductor Laser Devices*. 1980: Wiley.
16. McIlroy, P.W.A., A. Kurobe, and Y. Uematsu, *Analysis and Application of Theoretical Gain Curves to the Design of Multi-Quantum-Well Lasers*. IEEE Journal of Quantum Electronics, 1985. **21**(12): p. 1958-1963.
17. Arakawa, Y. and H. Sakaki, *Multidimensional Quantum Well Laser and Temperature-Dependence of Its Threshold Current*. Applied Physics Letters, 1982. **40**(11): p. 939-941.

18. Asada, M., Y. Miyamoto, and Y. Suematsu, *Gain and the Threshold of 3-Dimensional Quantum-Box Lasers*. IEEE Journal of Quantum Electronics, 1986. **22**(9): p. 1915-1921.
19. Sellin, R.L., C. Ribbat, M. Grundmann, N.N. Ledentsov, and D. Bimberg, *Close-to-ideal device characteristics of high-power InGaAs/GaAs quantum dot lasers*. Applied Physics Letters, 2001. **78**(9): p. 1207-1209.
20. Bimberg, D., M. Grundmann, and N.N. Ledentsov, *Quantum Dot Heterostructures*. 1999, New York: Wiley.
21. Priester, C. and M. Lannoo, *Origin of Self-Assembled Quantum Dots in Highly Mismatched Heteroepitaxy*. Physical Review Letters, 1995. **75**(1): p. 93-96.
22. Leonard, D., M. Krishnamurthy, C.M. Reaves, S.P. Denbaars, and P.M. Petroff, *Direct Formation of Quantum-Sized Dots from Uniform Coherent Islands of InGaAs on GaAs Surfaces*. Applied Physics Letters, 1993. **63**(23): p. 3203-3205.
23. Sugawara, M., K. Mukai, and H. Shoji, *Effect of phonon bottleneck on quantum-dot laser performance*. Applied Physics Letters, 1997. **71**(19): p. 2791-2793.
24. Blood, P., *On the dimensionality of optical absorption, gain, and recombination in quantum-confined structures*. IEEE Journal of Quantum Electronics, 2000. **36**(3): p. 354-362.
25. Coldren, L.A. and S.W. Corzine, *Diode Lasers and Photonic Integrated Circuits*. 1995, New York: Wiley.
26. Herrmann, E., P.M. Smowton, Y. Ning, K.M. Groom, D.J. Mowbray, and M. Hopkinson, *Performance of lasers containing three, five and seven layers of quantum dots*. IEE Proceedings-Optoelectronics, 2001. **148**(5-6): p. 238-242.
27. Smowton, P.M., E. Herrmann, Y. Ning, H.D. Summers, P. Blood, and M. Hopkinson, *Optical mode loss and gain of multiple-layer quantum-dot lasers*. Applied Physics Letters, 2001. **78**(18): p. 2629-2631.
28. Heitz, R., A. Kalburge, Q. Xie, M. Grundmann, P. Chen, A. Hoffmann, A. Madhukar, and D. Bimberg, *Excited states and energy relaxation in stacked InAs/GaAs quantum dots*. Physical Review B, 1998. **57**(15): p. 9050-9060.
29. Solomon, G.S., J.A. Trezza, A.F. Marshall, and J.S. Harris, *Vertically aligned and electronically coupled growth induced InAs islands in GaAs*. Physical Review Letters, 1996. **76**(6): p. 952-955.
30. Kestle, A., *The modification and control of electrical barriers at semiconductor interfaces*. PhD, University Of Wales, Cardiff
31. *NSM Archive - Physical Properties of Semiconductors* [WWW], Ioffe Institute Peterburg. Available at: <<http://www.ioffe.rssi.ru/SVA/NSM/Semicond/>> [Accessed:19th January 2005]
32. Smowton, P.M., G.M. Lewis, A. Sobiesierski, P. Blood, J. Lutti, and S. Osbourne, *Non-uniform carrier distribution in multi-quantum-well lasers*. Applied Physics Letters, 2003. **83**(3): p. 419-421.
33. Smowton, P.M. and P. Blood, *The differential efficiency of quantum-well lasers*. IEEE Journal of Selected Topics in Quantum Electronics, 1997. **3**(2): p. 491-498.
34. Smowton, P.M. and P. Blood, *Fermi level pinning and differential efficiency in GaInP quantum well laser diodes*. Applied Physics Letters, 1997. **70**(9): p. 1073-1075.

35. Park, G., O.B. Shchekin, S. Csutak, D.L. Huffaker, and D.G. Deppe, *Room-temperature continuous-wave operation of a single-layered 1.3 μ m quantum dot laser*. Applied Physics Letters, 1999. **75**(21): p. 3267-3269.
36. Huang, X.D., A. Stintz, C.P. Hains, G.T. Liu, J. Cheng, and K.J. Malloy, *Efficient high-temperature CW lasing operation of oxide-confined long-wavelength InAs quantum dot lasers*. Electronics Letters, 2000. **36**(1): p. 41-42.
37. Ustinov, V.M. and A.E. Zhukov, *GaAs-based long-wavelength lasers*. Semiconductor Science and Technology, 2000. **15**(8): p. R41-R54.
38. Liu, G.T., A. Stintz, H. Li, K.J. Malloy, and L.F. Lester, *Extremely low room-temperature threshold current density diode lasers using InAs dots in In_{0.15}Ga_{0.85}As quantum well*. Electronics Letters, 1999. **35**(14): p. 1163-1165.
39. Sellers, I.R., H.Y. Liu, K.M. Groom, D.T. Childs, D. Robbins, T.J. Badcock, M. Hopkinson, D.J. Mowbray, and A.S. Skolnick, *1.3 μ m InAs/GaAs multilayer quantum-dot laser with extremely low room-temperature threshold current density*. Electronics Letters, 2004. **40**(22): p. 1412-1413.
40. Thomson, J.D., H.D. Summers, P.J. Hulyer, P.M. Smowton, and P. Blood, *Determination of single-pass optical gain and internal loss using a multisection device*. Applied Physics Letters, 1999. **75**(17): p. 2527-2529.
41. Shaklee, K.L. and R.F. Leheny, *Direct Determination of Optical Gain in Semiconductor Crystals*. Applied Physics Letters, 1971. **18**(11): p. 475-477.
42. Oster, A., G. Erbert, and H. Wenzel, *Gain spectra measurements by a variable stripe length method with current injection*. Electronics Letters, 1997. **33**(10): p. 864-866.
43. Hakki, B.W. and T.L. Paoli, *Gain Spectra in GaAs double-heterostructure injection lasers*. Journal of Applied Physics, 1975. **46**(3): p. 1299-1306.
44. Cassidy, D.T., *Technique for Measurement of the Gain Spectra of Semiconductor Diode-Lasers*. Journal of Applied Physics, 1984. **56**(11): p. 3096-3099.
45. Blood, P., G.M. Lewis, P.M. Smowton, H. Summers, J. Thomson, and J. Lutti, *Characterization of semiconductor laser gain media by the segmented contact method*. IEEE Journal of Selected Topics in Quantum Electronics, 2003. **9**(5): p. 1275-1282.
46. Summers, H.D., J.D. Thomson, P.M. Smowton, P. Blood, and M. Hopkinson, *Thermodynamic balance in quantum dot lasers*. Semiconductor Science and Technology, 2001. **16**(3): p. 140-143.
47. Schneider, H.C., W.W. Chow, and S.W. Koch, *Many-body effects in the gain spectra of highly excited quantum-dot lasers*. Physical Review B, 2001. **64**(11): p. 5315-+.
48. Schneider, H.C., W.W. Chow, and S.W. Koch, *Anomalous carrier-induced dispersion in quantum-dot active media*. Physical Review B, 2002. **66**(4): p. art. no.-041310.
49. Matthews, D.R., H.D. Summers, P.M. Smowton, and M. Hopkinson, *Experimental investigation of the effect of wetting-layer states on the gain-current characteristic of quantum-dot lasers*. Applied Physics Letters, 2002. **81**(26): p. 4904-4906.
50. Chow, W.W. and S.W. Koch, *Semiconductor-laser fundamentals*. 2000: Springer.
51. Sugiyama, Y., Y. Nakata, S. Muto, N. Horiguchi, T. Futatsugi, Y. Awano, and N. Yokoyama, *Observation of spectral hole burning in photocurrent spectrum of InAs self-assembled quantum dots buried in pn-junction*. Physica E, 1998. **2**(1-4): p. 632-636.

52. Notomi, M., T. Furuta, H. Kamada, J. Temmyo, and T. Tamamura, *Microscopic excitation spectroscopy for zero-dimensional quantized states of individual $\text{In}_x\text{Ga}_{1-x}\text{As}/\text{Al}_y\text{Ga}_{1-y}\text{As}$ quantum dots*. Physical Review B, 1996. **53**(23): p. 15743-15748.
53. Borri, P., W. Langbein, S. Schneider, U. Woggon, R.L. Sellin, D. Ouyang, and D. Bimberg, *Exciton relaxation and dephasing in quantum-dot amplifiers from room to cryogenic temperature*. IEEE Journal of Selected Topics in Quantum Electronics, 2002. **8**(5): p. 984-991.
54. Sugawara, M., K. Mukai, Y. Nakata, K. Otsubo, and H. Ishikawa, *Performance and physics of quantum-dot lasers with self-assembled columnar-shaped and 1.3- μm emitting InGaAs quantum dots*. IEEE Journal of Selected Topics in Quantum Electronics, 2000. **6**(3): p. 462-474.
55. Matsuda, K., K. Ikeda, T. Saiki, H. Tsuchiya, H. Saito, and K. Nishi, *Homogeneous linewidth broadening in a $\text{In}_{0.5}\text{Ga}_{0.5}\text{As}/\text{GaAs}$ single quantum dot at room temperature investigated using a highly sensitive near-field scanning optical microscope*. Physical Review B, 2001. **63**(12): p. art. no.-121304.
56. Osborne, S., P. Blood, P. Smowton, J. Lutti, Y.C. Xin, A. Stintz, D. Huffaker, and L.F. Lester, *State filling in InAs quantum-dot laser structures*. IEEE Journal of Quantum Electronics, 2004. **40**(12): p. 1639-1645.
57. Urayama, J., T.B. Norris, J. Singh, and P. Bhattacharya, *Observation of phonon bottleneck in quantum dot electronic relaxation*. Physical Review Letters, 2001. **86**(21): p. 4930-4933.
58. Lee, W., J.M. Myoung, Y.H. Yoo, and H. Shin, *Effect of elastic anisotropy on the strain fields and band edges in stacked InAs/GaAs quantum dot nanostructures*. Solid State Communications, 2004. **132**(2): p. 135-140.
59. Coli, P. and G. Iannaccone, *Modelling of self-organized InAs quantum dots embedded in an $\text{AlGaAs}/\text{GaAs}$ heterostructure*. Nanotechnology, 2002. **13**(3): p. 263-266.
60. Park, G., D.L. Huffaker, Z. Zou, O.B. Shchekin, and D.G. Deppe, *Temperature dependence of lasing characteristics for long-wavelength (1.3- μm) GaAs -based quantum-dot lasers*. IEEE Photonics Technology Letters, 1999. **11**(3): p. 301-303.
61. Zhukov, A.E., A.R. Kovsh, S.S. Mikhlin, A.P. Vasil'ev, E.S. Semenova, N.A. Maleev, V.M. Ustinov, M.M. Kulagina, E.V. Nikitina, and I.P. Soshnikov, *High external differential efficiency and high optical gain of long-wavelength quantum dot diode laser*. Physica E: Low-dimensional Systems and Nanostructures, 2003. **17**: p. 589-592.
62. Zhukov, A.E., A.R. Kovsh, V.M. Ustinov, A.Y. Egorov, N.N. Ledentsov, A.F. Tsatsul'nikov, M.V. Maximov, Y.M. Shernyakov, V.I. Kopchatov, A.V. Lunev, P.S. Kop'ev, D. Bimberg, and Z.I. Alferov, *Gain characteristics of quantum dot injection lasers*. Semiconductor Science and Technology, 1999. **14**(1): p. 118-123.
63. Ilahi, B., L. Sfaxi, H. Maaref, G. Bremond, and G. Guillot, *Long wavelength vertically stacked $\text{InAs}/\text{GaAs}(001)$ quantum dots with a bimodal size distribution: Optical properties and electronic coupling*. Superlattices and Microstructures, 2004. **36**(1-3): p. 55-61.
64. Im, J.S., S. Heppel, H. Kollmer, A. Sohmer, J. Off, F. Scholz, and A. Hangleiter, *Evidence for quantum-dot-like states in GaInN/GaN quantum wells*. Journal of Crystal Growth, 1998. **190**: p. 597-600.

PUBLICATIONS AND CONFERENCES

Tanguy, Y., J. Muszalski, J. Houlihan, G. Huyet, E.J. Pearce, P.M. Snowton, and M. Hopkinson, *Mode formation in broad area quantum dot lasers at 1060 nm*. Optics Communications, 2004. **235**(4-6): p. 387-393.

Snowton, P.M., E.J. Pearce, J. Lutti, D.R. Matthews, H.D. Summers, G.M. Lewis, P. Blood, M. Hopkinson, and A. Krysa. *Carrier distribution, spontaneous emission and gain in self assembled quantum dot lasers*. in *Novel in-plane semiconductor lasers III*. 2004, ed. C.F. Gmachl and D.P. Bour, Proceedings of the Society of Photo-Optical Instrumentation Engineers (SPIE), Vol. 5365: p. 86-95

Pearce, E.J., P.M. Snowton, and M. Hopkinson, *A Comparison of the Overall Radiative Efficiency of DWELL, Standard Quantum Dot and Quantum Well Laser Structures*, in *Optoelectronic Applications of Quantum Dots and Nanoparticles - Rank Prize Funds*. 2004: UK.

Pearce, E.J., P.M. Snowton, and M. Hopkinson, *A Comparison of the Overall Radiative Efficiency of DWELL, Standard Quantum Dot and Quantum Well Laser Structures*, in *LEOS03*. 2003: Tuscon, AZ.

Snowton, P.M., E.J. Pearce, H.C. Schneider, W.W. Chow, and M. Hopkinson, *Filamentation and linewidth enhancement factor in InGaAs quantum dot lasers*. Applied Physics Letters, 2002. **81**(17): p. 3251-3253.

Schneider, H.C., W.W. Chow, P.M. Snowton, E.J. Pearce, and S.W. Koch, *Anomalous Carrier-Induced Dispersion in Semiconductor Quantum Dots*. Optics and Photonics News, 2002. **13**(12): p. 50.

Pearce, E.J., P.M. Snowton, H.C. Schneider, W.W. Chow, and M. Hopkinson, *Filamentation and Linewidth Enhancement Factor in InGaAs Quantum Dot Lasers*, in *Photon02*. 2002: Cardiff, UK.

Pearce, E.J., P.M. Snowton, H.C. Schneider, W.W. Chow, and M. Hopkinson, *Filamentation in Quantum Dot Lasers*, in *SIOE02*. 2002: Cardiff, UK.

Pearce, E.J., *From Laboratory to Living Room - The Microscopic Laser*, in *Cardiff University Dept Physics & Astronomy 6th Form Conference*. 2001.

Pearce, E.J., P.M. Snowton, E. Herrmann, and M. Hopkinson, *Filamentation and Linewidth Enhancement Factor in InGaAs Quantum Dot Lasers*, in *SIOE01*. 2001: Cardiff, UK.

Patane, A., A. Polimeni, L. Eaves, M. Henini, P.C. Main, P.M. Snowton, E.J. Johnston, P.J. Hulyer, E. Herrmann, G.M. Lewis, and G. Hill, *Experimental studies of the multimode spectral emission in quantum dot lasers*. Journal of Applied Physics, 2000. **87**(4): p. 1943-1946.

Snowton, P.M., E.J. Johnston, S.V. Dewar, P.J. Hulyer, H.D. Summers, A. Patane, A. Polimeni, and M. Henini, *Spectral analysis of InGaAs/GaAs quantum-dot lasers*. Applied Physics Letters, 1999. **75**(15): p. 2169-2171.

